Measurement of the Radial Electric Field in the ASDEX Tokamak

A. R. Field, G. Fussmann, J. V. Hofmann

IPP III/165

December 1990

MAX-PLANCK-INSTITUT FÜR PLASMAPHYSIK

8046 GARCHING BEI MÜNCHEN

MAX-PLANCK-INSTITUT FÜR PLASMAPHYSIK

GARCHING BEI MÜNCHEN

Measurement of the Radial Electric Field in the ASDEX Tokamak

A. R. Field, G. Fussmann, J. V. Hofmann

IPP III/165

December 1990

Die nachstehende Arbeit wurde im Rahmen des Vertrages zwischen dem Max-Planck-Institut für Plasmaphysik und der Europäischen Atomgemeinschaft über die Zusammenarbeit auf dem Gebiete der Plasmaphysik durchgeführt.

MEASUREMENT OF THE RADIAL ELECTRIC FIELD IN THE ASDEX TOKAMAK

A. R. FIELD, G. FUSSMANN, J. V. HOFMANN and the ASDEX team

Max-Planck-Institut für Plasmaphysik
EURATOM-IPP Association D-8046 Garching, FRG

Abstract:

The radial electric field (E_r) at the plasma periphery is determined by measuring the drift velocities of low-Z impurity ions (BIV, CIII and HeII). The measurements are performed with a scannable mirror system which allows the determination of the poloidal, perpendicular (to $\vec{B}$) and toroidal components of the drift velocities from the differential Doppler shift of visible line emission observed along opposing viewing directions.

The principle of the measurement is investigated in detail. In particular, it is shown that for radially localised emission shells there exits a line of sight oriented perpendicular to $\vec{B}$ along which E_r may be inferred directly from the observed Doppler shift of the line emission. Along such a line of sight the net contribution to the shift from the diamagnetic drift and the radial gradient of the excitation probability is negligible.

During the Ohmic- and L-phases the perpendicular drift velocity of the BIV ions measured approximately 2 cm inside the separatrix is small ($\leq 2 kms^{-1}$) and in the ion diamagnetic drift direction. However, at the L→H-mode transition it changes sign and begins to increase on the time-scale of the edge pressure gradients reaching the highest values at the end of the H*-phase. From these high perpendicular drift velocities it is inferred that, in the H-mode, there exists a strong negative radial electric field ($|E_r| \leq 25\ kVm^{-1}$) just inside the separatrix. The dependence of the drift velocity of the BIV ions and E_r on the NBI-heating power and the magnitude and direction of the plasma current and the magnetic field is investigated.

Contents

1. Introduction:

The cause of the sudden substantial improvement in the confinement of a Tokamak which occurs at the transition into the H-mode [1.1] is not yet fully understood. This deficiency of knowledge hinders the reliable prediction of the performance of future devices. As future Tokamaks will operate routinely in the H-mode it is of great importance to understand the cause and the physics of this confinement regime. Various authors have developed theories in which it is proposed that the anomalous transport is reduced by presence of a strong radial electric field [1.2] and / or sheared poloidal rotation [1.3, 4, 5] just inside the separatrix thus causing the H-mode.

The presence of a strong negative radial electric field (inwardly directed) of magnitude $|E_r| \cong 15$ kVm^{-1} and sheared poloidal rotation within the thermal barrier of the H-mode has been inferred from spectroscopic measurements of the drift velocities of low-Z impurities at the plasma periphery of DIII-D [1.6] and, more recently, JFT-2M [1.7]. In the CCT device it is found that radial currents, driven through the edge plasma using a biased internal electrode, induce H-mode like conditions [1.8]. Also, in Textor, the induction of a radial electric field of either sign in the edge plasma with a biased electrode [1.9] is found to induce the H-mode.

Here are presented measurements of the radial electric field within the thermal barrier of ASDEX H-mode plasmas. We investigate the basic physics of spectroscopic measurements of radial electric fields by considering the effects of diamagnetic drifts, radial gradients of the excitation probability and line-of-sight integration on the observed Doppler shift. As our spectrometer views along a single line of sight we show that, when observing ionic species which emit from radially localised shells, there is a chord at a particular impact radius, aligned perpendicular to $\vec{B}$, where the radial electric field can be directly inferred from the measured perpendicular drift velocities without having to account for contributions to the shift from the diamagnetic drift and gradients of the excitation probability.

We have concentrated our measurements on the BIV(2823 Å) and CIII (4649 Å) triplet lines and the HeII (4686 Å) line; the measurements on the BIV (2823 Å) triplet being the most successful. Poloidal, perpendicular (to $\vec{B}$) and toroidal components of the drift velocities are measured just inside the separatrix and used to construct vector diagrams.

From the perpendicular component of the BIV ion drift velocity, $v_{i\perp}$, measured during the H-mode we infer the presence of a strong negative radial electric field ($|E_r| \leq 25$ kVm^{-1}) just inside the separatrix. At the L→H-mode transition $v_{i\perp}$ and E_r begin to increase slowly from their Ohmic-phase values ($|v_{i\perp}| \leq 2$ kms^{-1}, $|E_r| \leq 4$ kVm^{-1}) on the time-scale of the development of the edge temperature and pressure gradients. The dependence of $v_{i\perp}$ and E_r on the NBI-heating power and the direction and the magnitude of the plasma current and the magnetic field are presented. We briefly discuss our results in terms of neo-classical theories of poloidal momentum damping and poloidal rotation.

2. Principle of Electric Field Measurement:

2.1 Basic Equations:

In cylindrical geometry the basic relation between the macroscopic drift velocity of a particle species $\vec{v}_i$ and a radial electric field is obtained from the radial component of the equation of motion for the species. For an ion of species i, charge eZ_i and mass m_i the equation of motion is [2.1]:

$$n_i m_i \left(\frac{\partial \vec{v}_i}{\partial t} + \vec{v}_i \cdot \nabla \vec{v}_i \right) = e Z_i n_i \left(\vec{E} + \vec{v}_i \times \vec{B} \right) - \nabla \cdot \vec{\psi}_i + \sum_j \vec{P}_{ij} \quad (2.1)$$

where n_i is the species density, $\vec{\psi}_i$ is the stress tensor, including viscosity, and $\vec{P}_{ij}$ is the frictional force between the species i and other species j. In a steady state, neglecting spatial variations of the particle velocity in the convective derivative and off-axis (viscous) terms in the stress tensor and assuming a scalar pressure Equ. (2.1) reduces to:

$$e Z_i n_i \left(\vec{E} + \vec{v}_i \times \vec{B} \right) = \nabla p_i - \sum_j \vec{P}_{ij} \quad (2.2)$$

Considering only the radial component and neglecting the inter-particle frictional forces this equation becomes:

$$e Z_i n_i \left(E_r + \left[\vec{v}_i \times \vec{B} \right]_r \right) = \frac{\partial p_i}{\partial r} \quad (2.3)$$

Equation (2.3) pertains for all charged particles provided that the radial velocities are sufficiently small so that the corresponding friction forces can be neglected. The perpendicular component of the fluid velocity $v_{i\perp}$ relevant in Equ. (2.3) is tangential to the magnetic surfaces and points nearly in the poloidal direction. We may rewrite Equ. (2.3) as:

$$v_{i\perp} = - \frac{1}{e Z_i n_i B} \frac{\partial p_i}{\partial r} + \frac{E_r}{B} = v_{diam} + v_{ExB} \quad (2.4)$$

Only in the case that the first term on the right hand side of this equation is small compared to the second can the electric field be directly determined from a measurement of the perpendicular fluid velocity, $v_{i\perp}$. Generally, the diamagnetic component of the fluid velocity v_{diam}, which is in a direction perpendicular to $\vec{B}$, has to be taken into account. For the deuterons the sign of v_{diam} is upwards at the outboard side of the minor cross-section of the Tokamak in ASDEX co-conditions (i.e. parallel current, field and neutral beam injection).

A few notes are appropriate in this context. Firstly, choosing low-Z impurity ions existing in narrow shells in the boundary region, in the case of $E_r = 0$, $v_{i\perp}$ will have a different sign at the inner and outer sides of the shell. In fact, different ions but of the same charge (e.g. CVI and OVI) may have opposite velocities at the same radial location. This apparent paradox is solved by realising that the diamagnetic velocity occurring in the above equations is solely produced by the gyration of the particles rather than by a motion of the gyro-centres. Furthermore, Equ. (2.4) implies that the diamagnetic drift velocity v_{diam} depends upon the ion species but that the velocity of the guiding centres v_{ExB} is independent of the ion species.

2.2 Diamagnetic and Pseudo Velocities:

An appropriate measurement of the Doppler shift of a spectral line does not necessarily provide a direct measurement of the perpendicular component of the local ion fluid velocity $v_{i\perp}$ given by Equ. (2.4). Attention has to be paid as to whether the Doppler shift of photons emitted from a volume element of plasma actually reflects the local ion fluid velocity which is related to the gradients of n_i and T_i over distances of the order of the gyro-radius. This is the case for photons which are emitted from excited ionic states k with a mean lifetime τ_k (= $1/\Sigma A_{jk}$) which is much shorter than the reciprocal gyro-frequency, ω_i^{-1}. In this case the ions are excited at the local excitation rate and decay almost instantaneously within an observed small volume element. The line shift, therefore, represents the perpendicular fluid velocity $v_{i\perp}$ of the ion species. For the opposite case, where $\omega_i\tau_k \approx 1$ or $\omega_i\tau_k >> 1$, the spectral shift is influenced by a gradient in the excitation probability of the ground state ions ζ'_k and the velocity inferred from the Doppler shift $v_{i\perp}^*$ may not represent the local ion fluid velocity. This is because the photons may be emitted from ions which are excited outside the observed volume element. With a gradient in the excitation probability $\partial\zeta_k/\partial x$ perpendicular to $\vec{B} = B\hat{e}_z$ and observing along the y-axis, excited ions passing through the volume element with one sign of v_y (emitting red shifted photons) will be excited with a different probability than ions passing with the opposite sign of v_y (emitting blue shifted photons) because of the gyration of the ions across the gradient of the excitation probability. (These coordinates are as used in the derivation presented in Appendix 3). A Doppler shift will be observed when there is a gradient in the excitation probability, even in the absence of gradients of n_i and T_i and a radial electric field.

This effect is considered in detail in Appendix 1 where it is shown that, in the presence of gradients of n_i, T_i and ζ_k perpendicular to $\vec{B}$ the velocity inferred from the Doppler shift of a spectral line $v_{i\perp}^*$ is given by:

$$v_{i\perp}^* = -\frac{1}{eZ_i n_i B}\frac{\partial p_i}{\partial r} - \frac{T_i\Gamma}{eZ_iB}\left[\frac{\frac{\partial}{\partial r}(\zeta_k)}{\zeta_k}\right] + \frac{E_r}{B} = v_{diam} + v_{pseudo} + v_{ExB} \qquad (2.5)$$

where Γ is given by:

$$\Gamma = \frac{(\omega_i\tau_k)^2}{1+(\omega_i\tau_k)^2} \qquad (2.6)$$

The additional velocity component v_{pseudo} which contributes to the line shift is not a component of the fluid velocity but arises solely from the gradient of the excitation rate.

Equation (2.5) can be rearranged to give the radial electric field E_r in terms of $v_{i\perp}^*$, $\partial p_i/\partial r$ and ζ_k, as:

$$E_r = v_{i\perp}^* B + \frac{1}{eZ_i n_i}\frac{\partial p_i}{\partial r} + \frac{T_i\Gamma}{eZ_i}\left[\frac{\frac{\partial}{\partial r}(\zeta_k)}{\zeta_k}\right] \qquad (2.7)$$

Two extreme cases can be considered. Firstly, when $(\omega_i\tau_k)^2 << 1$ then $\Gamma \rightarrow 0$ and $v_{pseudo} \rightarrow 0$ in which case Equ. (2.5) reduces to Equ. (2.4). The drift velocity inferred from the Doppler shift $v_{i\perp}^*$ is then equal to the perpendicular fluid velocity of the ion species, $v_{i\perp}$.

In this case E_r is given by:

$$E_r = v^*_{i\perp} B + \frac{T_i}{eZ_i}\left[\frac{n_i'}{n_i} + \frac{T_i'}{T_i}\right] \quad (2.8)$$

and so E_r may be determined from the velocity determined from the Doppler shift $v_{i\perp}$*, the ion temperature profile (which can be determined from the Doppler broadening) and the relative density profile (which may be determined from the measured radial relative emissivity profile ε if the radial profile of the excitation probability ζ_k is known).

In the opposite case, where $(\omega_i\tau_k)^2 >> 1$, $\Gamma \rightarrow 1$ and v_{diam} and v_{pseudo} may be combined together to yield:

$$v^*_{i\perp} = -\frac{T_i}{eZ_iB}\left[\frac{\frac{\partial}{\partial r}(\varepsilon T_i)}{(\varepsilon T_i)}\right] + \frac{E_r}{B} \quad (2.9)$$

where ε is the local line emissivity. The radial electric field is then given by:

$$E_r = v^*_{i\perp} B + \frac{T_i}{eZ_i}\left[\frac{\frac{\partial}{\partial r}(\varepsilon T_i)}{(\varepsilon T_i)}\right] \quad (2.10)$$

Here, E_r may be directly determined from the measured radial relative emissivity profile and the radial profile of the ion temperature obtained from the Doppler broadening of the line emission.

Whether this additional contribution to the Doppler shift of a spectral line has to be considered when attempting to measure the ion fluid velocity or the radial electric field depends upon both the value of the parameter Γ (given by Equ. 2.6) and the gradient of the excitation probability ζ'_k being sufficiently high. In Appendix 2 the magnitude of v_{diam} and v_{pseudo} (of Equ. 2.5) are estimated from the relevant gradient scale lengths as measured (or estimated) in the boundary region of ASDEX H-mode plasmas. In Appendix 3 the appropriate values of Γ are estimated for the transitions investigated in this study. At B = 2.0 T the values of Γ are: CIII (4649Å), Γ = 0.14; HeII (4686Å), Γ = 0.01; and BIV (2823Å), Γ = 0.58. Thus, in the case of the BIV (2823Å) triplet we may expect a contribution to the Doppler shift due to the gradient of the excitation probability ζ'_k. Any such contribution to this shift in the cases of CIII (4649Å) and HeII (4686Å) would be correspondingly smaller (although for H-like ions (e.g. HeII) the unresolved fine structure complicates the measurement, as is discussed in Chap. 3).

In Appendix 2 it is shown that the velocity inferred from the measured Doppler shift $v_{i\perp}$* may be written in terms of equivalent electric fields as:

$$v^*_{i\perp} = \frac{1}{B}\left(E^*_{diam} + E^*_{pseudo} + E_r\right) = \frac{1}{B}\left(E^*_\Lambda + E_r\right) \quad (2.11)$$

where E_{diam}* and E_{pseudo}* are equivalent radial electric fields which would produce E_r/B drift velocities equal to v_{diam} and v_{pseudo} and E_Λ* is their sum. Estimates of these quantities, made using as much experimental data as is available, indicate that values of E_Λ* for the relevant transitions are: CIII (4649Å), E_Λ* = +3.6 kVm^{-1}; HeII (4686Å), E_Λ* = +11.4 kVm^{-1}; and BIV

(2823Å), $E_\Lambda^* = +10.1\ kVm^{-1}$; in the H-mode of ASDEX at the *outer* sides of the emission shells. In comparison, the measured values of E_r are typically $-10\ kVm^{-1}$. At most, in the case of BIV (2823Å), E_{pseudo}^* contributes 6% to the estimated value of E_Λ^*. In conclusion, these estimates indicate that contributions to the measured Doppler shift from the v_{diam} term can, locally, be of the same order of magnitude (but of the opposite sign) as that from the likely E_r/B drift velocity and that the contribution from the gradient of the excitation probability ζ'_k is small. (Note that, in the case of charge exchange recombination with energetic neutrals from a heating beam, the gradient of n_o may be steep and of the opposite sign to those of T_e and n_e thus changing the sign of E_{pseudo}^*.)

These discussions refer to a radially localised measurement of the line profile. In general, the line profile is an integral of the emissivity from along the line of sight. It is shown below that, when measuring the line profile of line emission from an ion species which is localised in a narrow shell at the plasma boundary, contributions to the line shift from the diamagnetic drift and the gradient of the excitation probability may cancel along a particular chord thus enabling a direct determination of E_r from the Doppler shift measured at a particular radius.

2.3 Thermal Equilibration:

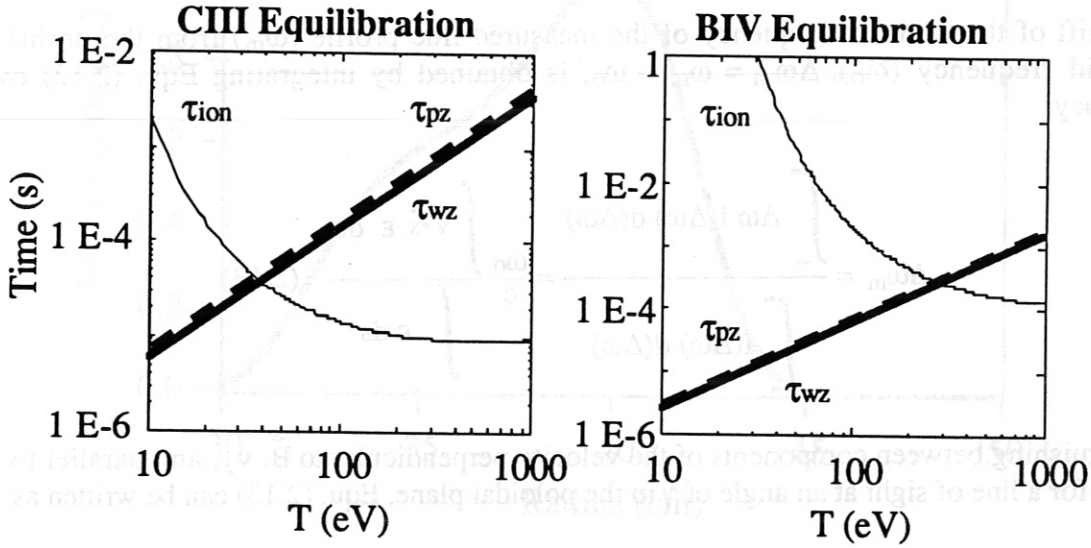

Fig. 2.1 (a,b): C III and B IV ionisation and equilibration. A comparison of momentum and energy equilibration times τ_{pz}, τ_{wz} and ionisation time τ_{ion} as a function of temperature for $n_e = 1{\cdot}10^{13}\ cm^{-3}$.

It should be considered whether the ions under investigation reach the local ion temperature and drift velocity of the background plasma before being further ionized. This is of particular importance when inferring drift velocities and ion temperatures from the measured Doppler shift and broadening. Fig. 2.1 (a,b) shows a comparison of the momentum equilibration time τ_{pz}, energy equilibration time τ_{wz} and ionisation time τ_{ion} as a function of temperature for CIII and BIV. Ionisation rates according to Lotz [2.2] are used and equal electron and ion temperatures are assumed. From the crossing points of the curves it can be concluded that it is possible to measure the parallel drift velocity $v_{i\|}$ and temperature of the background ions (deuterons) in a region where the electron temperature is below 40 eV in the case of C III and 300 eV in the case of B IV. At higher temperatures the values inferred from the Doppler broadening and the line shift have a tendency to underestimate the true values of T_i and $v_{i\|}$.

2.4 The Effect of Integration along the Line of Sight:

Here, the effect of the line-of-sight integration of the emissivity on the measured Doppler shift of the line centroid is considered. These effects are of particular importance when performing passive measurements where the line of sight does not intersect an exciting beam and thus allow a localised measurement to be performed. The measured line profile can be represented as an integral along the line of sight of shifted Gaussians representing the local line profile:

$$I(\Delta\omega) = \frac{c\,\Delta\Omega\,\Delta A}{4\pi\,\omega_o}\int \exp\left[-\left(\frac{\Delta\omega\;c}{\omega_0\;v_{th}} - \frac{\vec{v}\cdot\vec{s}}{v_{th}}\right)^2\right]\frac{\varepsilon}{v_{th}}\,ds \qquad (2.12)$$

where the local line intensitiy is proportional to the local emissivity ε, the shift of the local line centroid frequency (ω) from the unshifted centroid frequency (ω_o), $\Delta\omega = \omega - \omega_o$, is proportional to the component of the drift velocity along the line of sight, $\vec{s}$ is a unit vector in the direction of the chosen chord, c is the speed of light, v_{th} is the ion thermal velocity ($v_{th} = (2eT_i/m_i)^{1/2}$) and $\Delta\Omega\Delta A$ étendu of the spectrometer.

The shift of the centroid frequency of the measured line profile (ω_m) from the unshifted centroid frequency (ω_o), $\Delta\omega_m = \omega_m - \omega_o$, is obtained by integrating Equ. (2.12) over frequency:

$$\Delta\omega_m = \frac{\int_{-\infty}^{\infty}\Delta\omega\,I(\Delta\omega)\,d(\Delta\omega)}{\int_{-\infty}^{\infty}I(\Delta\omega)\,d(\Delta\omega)} = \frac{\omega_0}{c}\frac{\int \vec{v}\cdot\vec{s}\;\varepsilon\;ds}{\int \varepsilon\;ds} \qquad (2.13)$$

Distinguishing between components of the velocity perpendicular to $\vec{B}$, $v_\perp$, and parallel to $\vec{B}$, $v_\parallel$, and for a line of sight at an angle of γ to the poloidal plane, Equ. (2.13) can be written as:

$$\Delta\omega_m = \frac{\omega_0}{c}\frac{\int_{r_0}^{a}\frac{\left[v_\perp r_0 + v_\parallel\left(\frac{B_\theta}{B}r_0 + \gamma r\right)\right]\varepsilon\;dr}{\sqrt{r^2 - r_0^2}}}{\int_{r_0}^{a}\frac{\varepsilon\;r\,dr}{\sqrt{r^2 - r_0^2}}} \qquad (2.14)$$

The contributions to the observed Doppler shift due to $v_\parallel$ may be minimized, although they cannot be completely suppressed, by choosing $\gamma = -B_\theta(r_0)/B$ so that we observe in a direction as nearly $\perp$ to $\vec{B}$ as possible.

The pitch angle of the field lines B_θ/B may be expressed in terms of the safety factor q(r): $B_\theta / B \approx r / (R_0 q)$. It is assumed that:

$$\frac{B_\theta}{B} = \frac{1}{A\, q_a} \frac{\left[1 - \left(1 - \rho^2\right)^{q_a}\right]}{\rho} \qquad (2.15)$$

where $A = R_0 / a$ and $\rho = r / a$.

As an example (the results of which are considered in our evaluation of the radial electric field presented in Sect. 6.6), Equ. (2.9) can be used to calculate the 'drift velocity', $v_{i\perp m}^*$, which would be inferred from the shift of the line centroid $\Delta\omega_m$ (using the relation $v_{i\perp m}^* = -c\Delta\omega_m/\omega_o$) when observing along a chord of impact parameter r_0 at an angle of γ to the poloidal plane for various model cases.

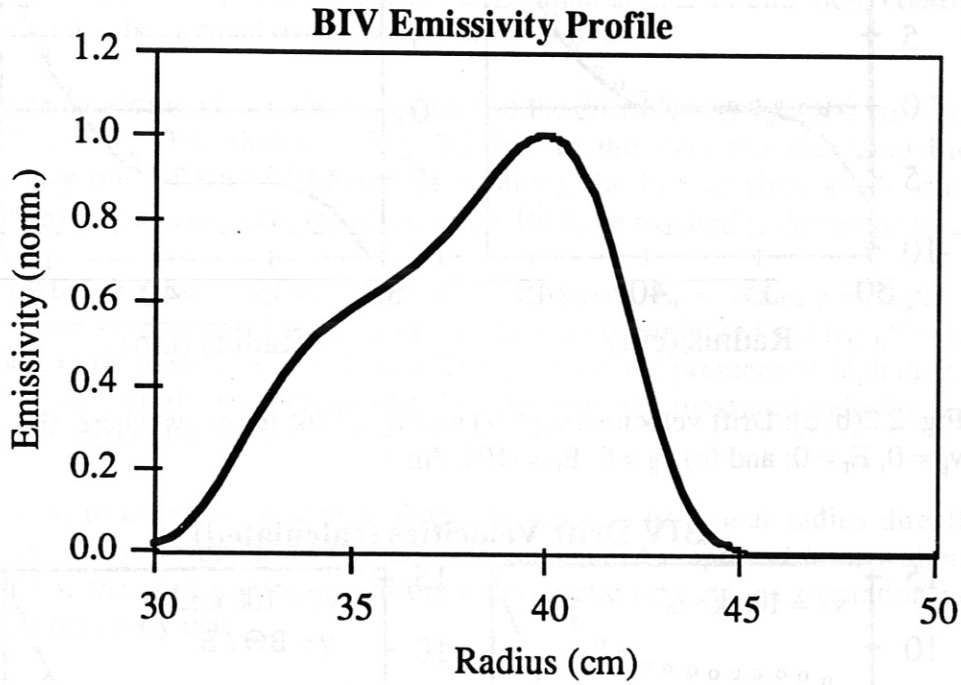

Fig. 2.2 (a): The normalised radial emissivity profile $\varepsilon(r)$ of the BIV (2823Å) line as determined during the H*-mode (ELM-free H-mode) from shot-to-shot measurements of the line emissivity (see Fig. 6.1.3 (c)).

A fit to the measured relative radial emissivity profile of the BIV (2823Å) line (see Fig. 2.2 (a)) is used in Equ. (2.9) to calculate the equivalent local perpendicular ion 'drift velocity' $v_{i\perp}^*$ (equivalent as in this case an additional component to the line shift arises from the gradient of the excitation probability). Equ. (2.9) (relevant to the case where $(\omega_i\tau_k)^2 >> 1, \Gamma = 1$) is used because, for the BIV ions under ASDEX conditions, Γ is estimated to be approaching unity and with $\Gamma = 1$ we do not need to determine the relative ground state ion density from the relative emissivity profile. We assume that the BIV ion temperature profile is flat (T_i (BIV) = 200.0 eV) as there is little evidence from the BIV (2823Å) line profiles that the BIV ion temperature varies strongly with radius.

The measured BIV (2823Å) emissivity profile is taken from an Abel inversion of shot-to-shot measurements of the line intensity measured along chords of various impact radii (shown in the contour plot of Fig. 6.1.3 (c)), at 1.32 s during the H*-mode (ELM free H-mode). Measurements were not made at greater chord impact radii than $r_o = 44$ cm. Because of this we consider two cases where, at larger radii, we have assumed that either a) the measured intensities would continue as an extrapolation to a fit to those measured at smaller radii, or b) the measured intensities would decay exponentially outside the separatrix radius with a scale length of 1.2 cm as measured in Ref. [A2.1]. Case (b) gives the most rapid decay with radius and is considered to be the most realistic representation.

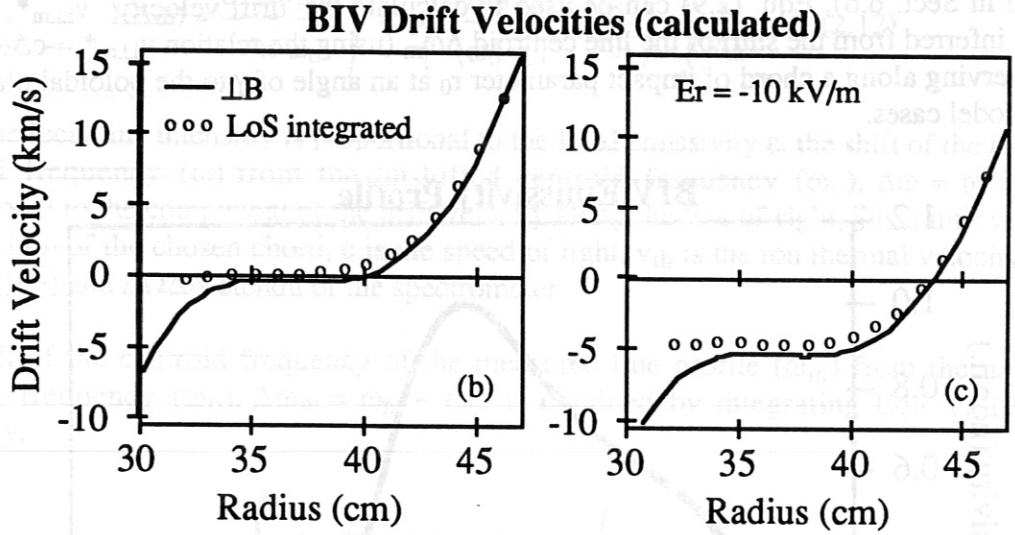

Fig. 2.2(b, c): Drift velocities $v_{i\perp}$* (-) and $v_{i\perp m}$* (o) for cases where: (b) $v_{\parallel} = 0$, $E_r = 0$; and (c) $v_{\parallel} = 0$, $E_r = -10\,kVm^{-1}$.

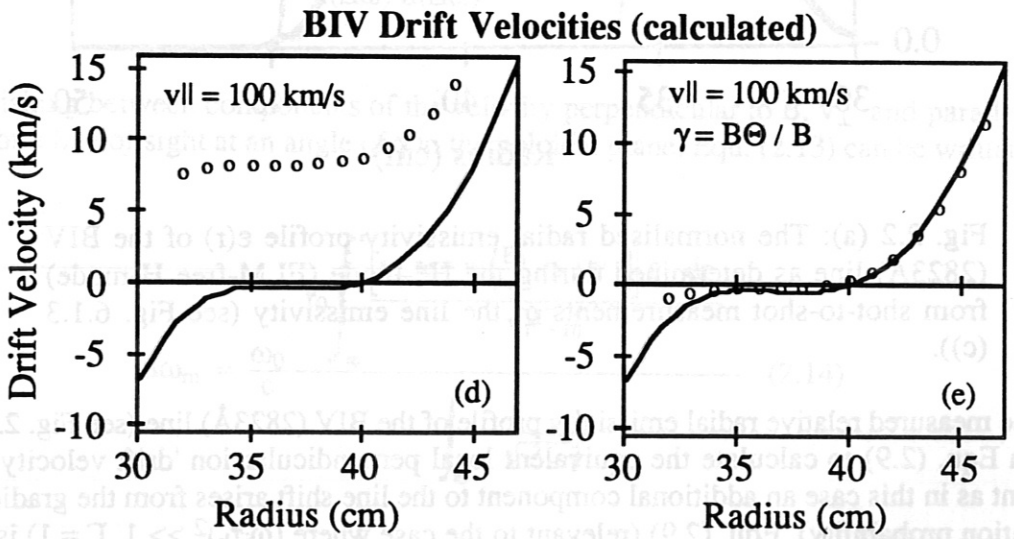

Fig. 2.2(d, e): Drift velocities $v_{i\perp}$* (-) and $v_{i\perp m}$* (o) for cases where: (d) $v_{\parallel} = 100$ km/s, $E_r = 0$, $\gamma = 0$; and (e) $v_{\parallel} = 100$ km/s, $E_r = 0$, $\gamma = -B_\Theta/B$.

Figs. 2.2 (b-e) show the equivalent local perpendicular ion 'drift velocity' $v_{i\perp}$* as calculated from Equ. (2.9) and the 'measured' velocity as would be inferred from the shift of the line centroid, $v_{i\perp m}$*, as calculated from Equ. (2.13) for different values of the radial electric field

E_r, the drift velocity parallel to $\vec{B}$, $v_{||}$, and the angle of the line of sight to the poloidal plane, γ. The emissivity profile of case (b) above is used for these calculations.

Results from the case where $E_r = 0$ and $v_{||} = 0$ are shown in Fig. 2.2(b). The effect of the line-of-sight integration is to reduce the measured velocity $v_{i\perp m}$* relative to the local value $v_{i\perp}$*(r_o) at small radii. For chord impact radii of 35 cm < r_o < 40 cm the diamagnetic drift and excitation gradient contributions to $v_{i\perp m}$* are small $|v_{i\perp m}^*| \leq 1.0 kms^{-1}$. These radii are just inside the radius of the maximum of the emission shell in the H*-phase at r_o = 40 cm.

Fig. 2.2 (c) shows a case where the effect of a radial electric field of $E_r = -10 kVm^{-1}$ is included. The result shown in Fig. 2.2 (b) indicates that in this case, at chord impact radii of 35 cm < r_o < 40 cm, we can infer the value of E_r directly from the measured velocity $v_{i\perp m}$* to an accuracy of ± (1.0xB(T)) kVm^{-1} without having to correct for contributions to the line shift from the diamagnetic drift and the excitation probability gradient. If we use the emissivity profiles of case (a) above, with the shallower gradient at $r_o \geq 44$ cm, these contributions to $v_{i\perp m}$* are found to be as small over a greater range of radii.

A case where an additional parallel component of the drift velocity $v_{||} = 100 kms^{-1}$ is included and $E_r = 0$ and $\gamma = 0$ is shown in Fig. 2.2 (d). In this case the measured line shift is predominantly due to the component of $v_{||}$ along the line of sight and a simultaneous measurement along a nearly orthogonal direction would be required to determine $v_{i\perp m}$*.

Finally, Fig. 2.2 (e) shows a case where $v_{||} = 100 kms^{-1}$, $E_r = 0$ and $\gamma = -B_\theta/B$. With this arrangement the component of $v_{||}$ along the line of sight is minimised and $|v_{i\perp m}^*| \leq 1.0 kms^{-1}$ at chord impact radii of 35 cm < r_o < 40 cm. Thus, even in the presence of high drift velocities parallel to $\vec{B}$, E_r can also be determined directly from the measured velocity $v_{i\perp m}$* to an accuracy of ± (1.0xB(T)) kVm^{-1}.

In conclusion, in order to be able to determine E_r at a particular radius directly from a measurement of the Doppler shift of the line centroid of a spectral line, without making corrections for the contributions from the diamagnetic drift or the excitation probability gradient, it is necessary that:

(i) The line emission is localised to narrow shells at an appropriate radius.

(ii) The observations are made along a line of sight with an impact radius just inside the radius of the maximum of the emissivity along which contributions to the measured Doppler shift from the diamagnetic drift and excitation probability gradient are negligible.

(iii) The line of sight should be oriented at such an angle to the poloidal plane that contributions to the line shift from any component of the drift velocity parallel to $\vec{B}$ are minimised.

3. Atomic Physics Considerations:

Measurements have been performed on the Be-like CIII (λ=4649Å) and He-like BIV (λ=2823Å) triplet lines and the H-like HeII (λ=4686Å) multiplet line. Typical raw spectra are shown in Figs. 3.1 and 3.2. The spectroscopic data for these lines which are relevant to this investigation are summarised in Table 3.1.

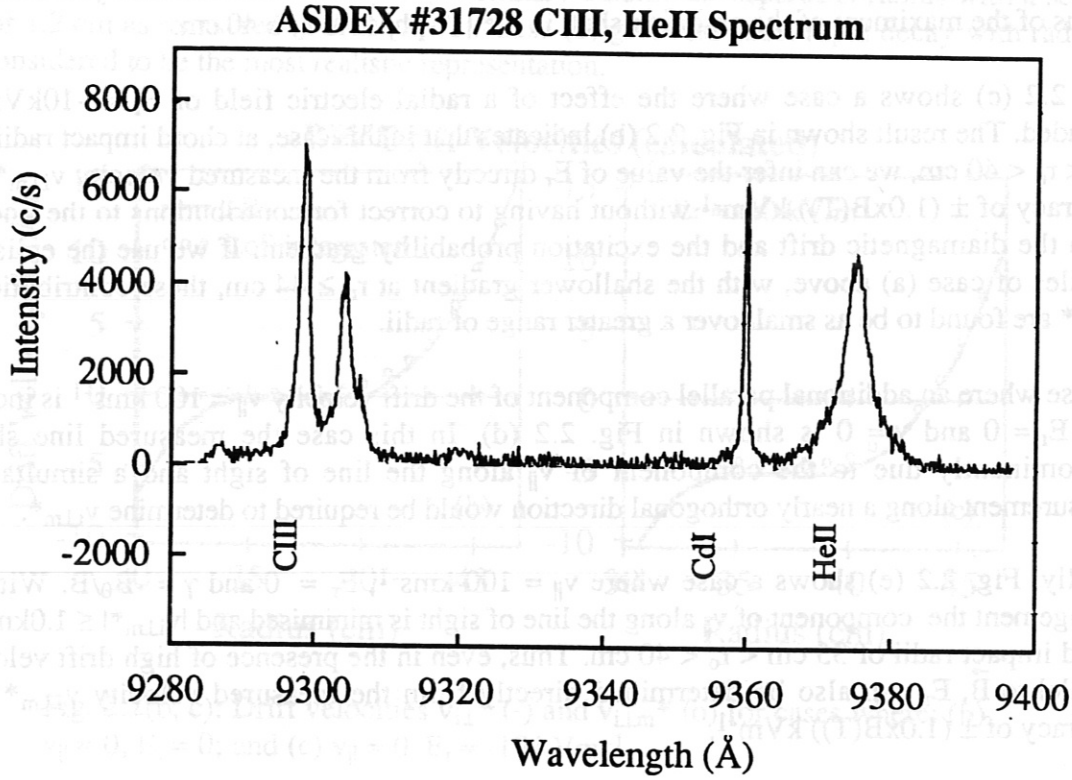

Fig. 3.1: A spectrum showing the CIII (λ=4649Å) and HeII (λ=4686Å) lines measured, simultaneously with a CdI (λ=4678Å) line from a calibration lamp, using a 1200 lmm^{-1} grating in 2nd order.

The intensities of the CV (λ=2274Å) and OV (λ=2784Å) lines, which are also suitable for poloidal rotation measurements, were too weak to perform analogous measurements as the concentrations of C and O were very low because of the prior boronization of the ASDEX vacuum vessel.

In the case of the CIII and BIV triplets ($^3S_1$ - $^3P_{0,1,2}$) the transitions from the upper levels with different j' are well separated in wavelength. Tabulated values of the wavelength separation ($\Delta\lambda$) of the longer wavelength components relative to the shortest wavelength component are given in Table. 3.1. With statistically weighted upper j'-level populations (as expected from electron impact excitation) the relative intensity of the component from the j'-level, $I_{rj'}$, are proportional to the statistical weight of the upper level, 2j'+1.

Ion	Configuration	Spectral Term	λ [Å]	Δλ [Å]	$I_{rj'}$	$<\delta\lambda_\sigma>/B$ [ÅT^{-1}]	T_i [eV]	$\delta\lambda_{1/2}$ [Å]	$\frac{<\delta\lambda_\sigma>/B}{\delta\lambda_{1/2}}$
CIII	$1s^22s3s$-$1s^22s3p$	$^3S_1$-$^3P_2$	4647.42	0	5/9	.126	50	.37	.34
CIII	$1s^22s3s$-$1s^22s3p$	$^3S_1$-$^3P_1$	4650.25	2.83	3/9	.177	50	.37	.47
CIII	$1s^22s3s$-$1s^22s3p$	$^3S_1$-$^3P_0$	4651.47	4.05	1/9	.202	50	.37	.55
BIV	1s2p-1s2p	$^3S_1$-$^3P_2$	2821.68	0	5/9	.065	200	.47	.14
BIV	1s2p-1s2p	$^3S_1$-$^3P_1$	2825.82	4.15	3/9	.074	200	.47	.16
BIV	1s2p-1s2p	$^3S_1$-$^3P_0$	2824.55	2.87	1/9	.046	200	.47	.10
HeII	3d-4f	$^2D_{5/2}$-$^2F_{7/2}$	4685.72	0	.39	.11	150	.64	.17
HeII	all intermediate	transitions	(lj - l'j')						
HeII	3s-3p	$^2S_{1/2}$-$^2P_{1/2}$	4685.46	0.27	.0032	.137	150	.64	.21

Table 3.1: Summary of relevant spectroscopic data: Δλ, wavelength separation of the longer wavelength component relative to the shortest wavelength component within the multiplet; $I_{rj'}$, relative intensity of the component from the j'-level to the total multiplet intensity; $\delta\lambda_{1/2}$, Doppler width (half width at half maximum intensity) at an ion temperature of T_i; $<\delta\lambda_\sigma>/B$, mean wavelength shift of the Zeeman σ–components on one side of the line centroid relative to their unperturbed wavelength per unit magnetic field intensity; and $<\delta\lambda_\sigma>/(B\delta\lambda_{1/2})$.

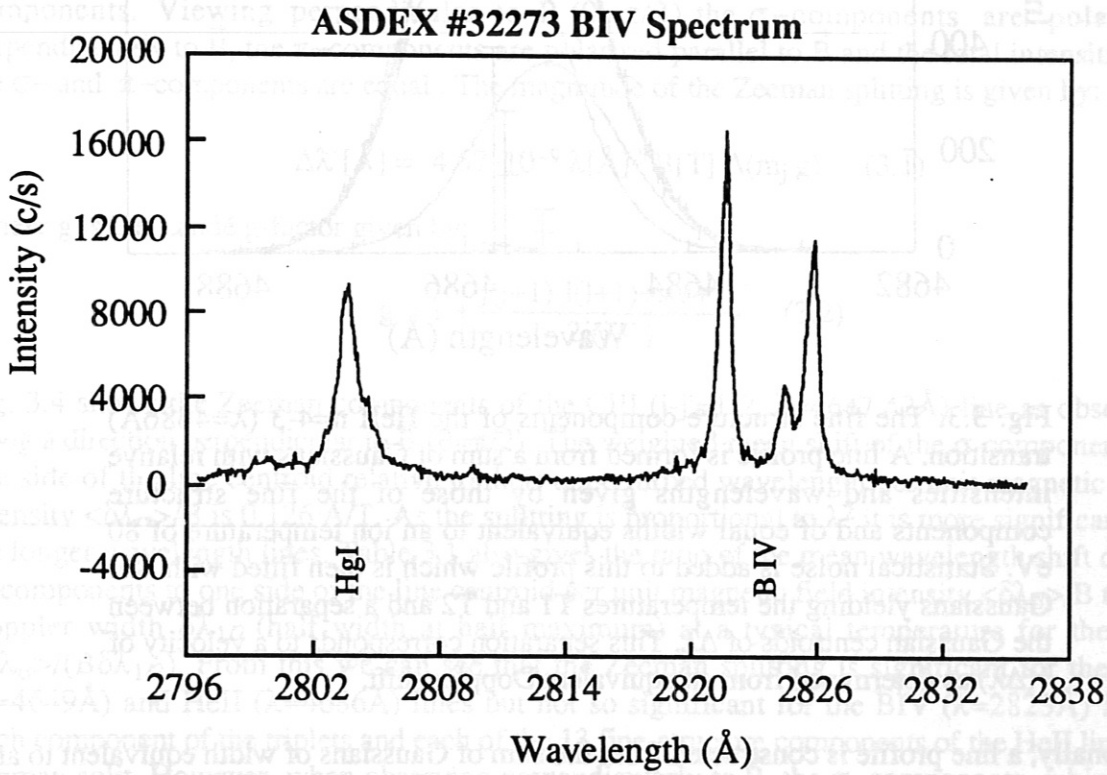

Fig. 3.2: A spectrum showing the BIV (λ=2823Å) triplet lines measured, simultaneously with a HgI (λ=2803Å) doublet line from a calibration lamp, using a 3600 lmm^{-1} grating in 1st order.

However, for the H-like HeII n = 3-4 (λ=4686Å) multiplet line the energy levels of different orbital quantum numbers l are degenerate but for the fine-structure splitting due to the weak j dependence of the spin-orbit interaction. This line actually consists of 13 different lj - l'j' transitions at 8 discrete wavelengths with a maximum separation of 0.54Å. The relative intensities of these lines are calculated (assuming statistically weighted relative populations of the upper levels as is appropriate for electron impact excitation) using sum-rules to calculate the relative transition probabilities between levels nlj -n'l'j'. Fig. 3.3 shows the fine-structure components of this line.

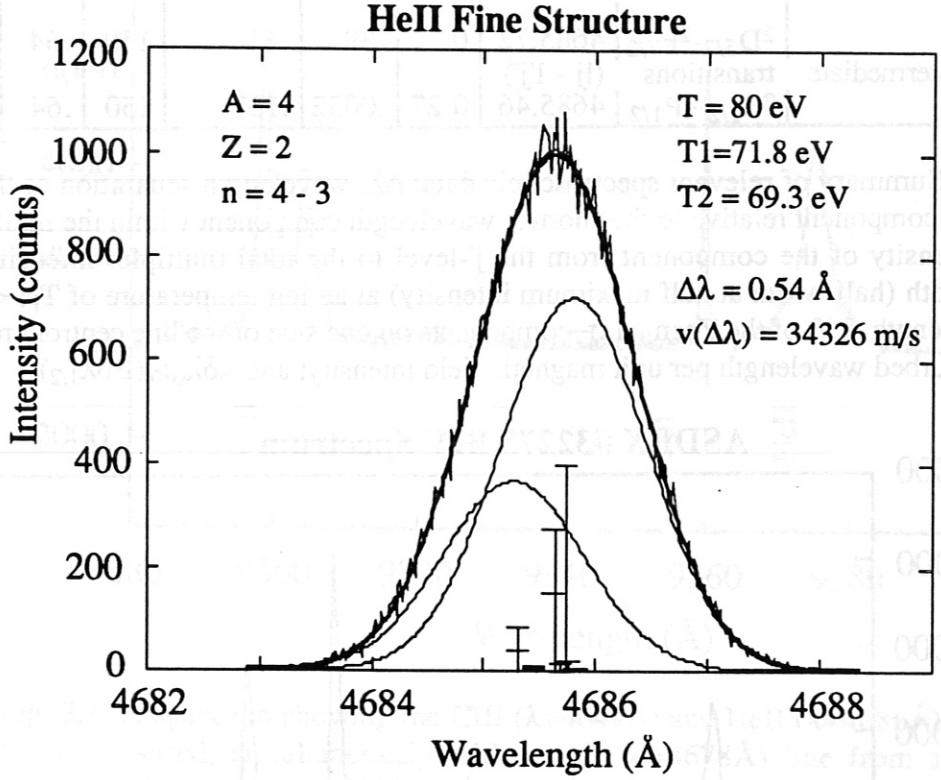

Fig. 3.3: The fine structure components of the HeII n=4-3 (λ=4686Å) transition. A line profile is formed from a sum of Gaussians with relative intensities and wavelengths given by those of the fine structure components and of equal widths equivalent to an ion temperature of 80 eV. Statistical noise is added to this profile which is then fitted with two Gaussians yielding the temperatures T1 and T2 and a separation between the Gaussian centroids of Δλ. This separation corresponds to a velocity of v(Δλ) as determined from an equivalent Doppler shift.

Additionally, a line profile is constructed from the sum of Gaussians of width equivalent to an ion temperature of 80 eV and of central wavelength and intensity given by that of each fine-structure component. An appropriate level of statistical noise (of S/N level typical of our measured spectra) is added to this profile which is then fitted with two Gaussians of free widths, intensities and central wavelengths. This subdivision of the HeII emission into two components (often refered to as the 'warm' and 'cold' components) is frequently used in charge-exchange-recombination spectroscopy. Note that the centroids of the two fitted Gaussians are separated by 0.54Å, which is equivalent to a velocity of 34 kms^{-1} as determined from an equivalent Doppler shift. Any changes in the relative populations of the

upper l-levels due to changes in the influence of competing population mechanisms (e.g. charge-exchange or electron-impact excitation) could alter this apparent 'drift' velocity. Therefore, drift velocity measurements made using this line should be interpreted with caution, particularly if simultaneous measurements from along opposing viewing directions are not available.

It is necessary to account for the Zeeman splitting of the lines (by the magnetic field of the Tokamak) in the line fitting procedure in order to provide a reliable representation of the various components of the observed multiplets. This is particularly important if the fits are to be used to determine the ion temperature from Doppler broadening and if the relative intensities, widths and separations of the triplet lines are to be used as a check on the reliability of the analysis procedure, e.g. to detect blended lines from other transitions. This is important as the presence of blended lines could contribute to the observed Doppler shifts.

In an external magnetic field each unperturbed energy level of a particular j is split into 2j+1 components corresponding to different values of the magnetic quantum number m_j. Transitions with $\Delta m_j = 0$ produce the central Zeeman π–components and transitions with $\Delta m_j = \pm 1$ produce the Zeeman σ–components which are symmetrically shifted about the unperturbed line position. The intensity of the π–components is proportional to $\sin^2\theta$ (were θ is the angle of the observation direction to the field) and that of the σ–components is proportional to $1+\cos^2\theta$. Viewing parallel to $\vec{B}$ ($\theta=0$) the σ–components are circularly polarized and there are no π–components. Viewing perpendicular to $\vec{B}$ ($\theta=\pi/2$) the σ–components are polarised perpendicularly to $\vec{B}$, the π–components are polarised parallel to $\vec{B}$ and the total intensities of the σ– and π–components are equal . The magnitude of the Zeeman splitting is given by:

$$\Delta\lambda\,[\text{Å}] = 4.67 \cdot 10^{-9}\,\lambda[\text{Å}]^2\,B[\text{T}]\,\Delta(m_j\,g) \qquad (3.1)$$

Where g is the Landé g-factor given by:

$$g = 1 + \frac{j(j+1)-l(l+1)+s(s+1)}{2j(j+1)} \qquad (3.2)$$

Fig. 3.4 shows the Zeeman components of the CIII (j-j'=1-2, λ=4647.42Å) line as observed along a direction perpendicular to $\vec{B}$ ($\theta=\pi/2$). The weighted mean shift of the σ-components to one side of the line centroid relative to their unperturbed wavelength per unit magnetic field intensity $\langle\delta\lambda_\sigma\rangle/B$ is 0.126 Å/T. As the splitting is proportional to λ^2 it is more significant for the longer wavelength lines. Table 3.1 also gives the ratio of the mean wavelength shift of the σ–components to one side of the line centroid per unit magnetic field intensity $\langle\delta\lambda_\sigma\rangle/B$ to the Doppler width $\delta\lambda_{1/2}$ (half width at half maximum) at a typical temperature for the ion, $\langle\delta\lambda_\sigma\rangle/(B\delta\lambda_{1/2})$. From this we can see that the Zeeman splitting is significant for the CIII (λ=4649Å) and HeII (λ=4686Å) lines but not so significant for the BIV (λ=2823Å) lines. Each component of the triplets and each of the 13 fine-structure components of the HeII line are Zeeman split. However, when observing perpendicularly to $\vec{B}$, the σ–components, which are polarised parallel to $\vec{B}$, can be removed with a polariser. When analysing data measured observing parallel to $\vec{B}$ (in which case only the σ–components are present) each of the triplet components is fitted with two symmetrically shifted Gaussians representing the σ–components or, for data measured when observing perpendicularly to $\vec{B}$ without the polariser, each of the triplet components are fitted with three Gaussians; one unshifted (representing the central π–components) and two symmetrically shifted about the line centroid (representing the σ–components). The magnitude of $\vec{B}$ may either be supplied to the fitting programme as a fixed parameter or determined from the fit. In the case of the CIII (λ=4649Å) triplet, the value of |B|

obtained from the fit is in good agreement with that obtained from the experimental parameters, however, in subsequent analysis the value of |B| appropriate to the experimental conditions is supplied to the fit in order to reduce the uncertainties of the other fit parameters.

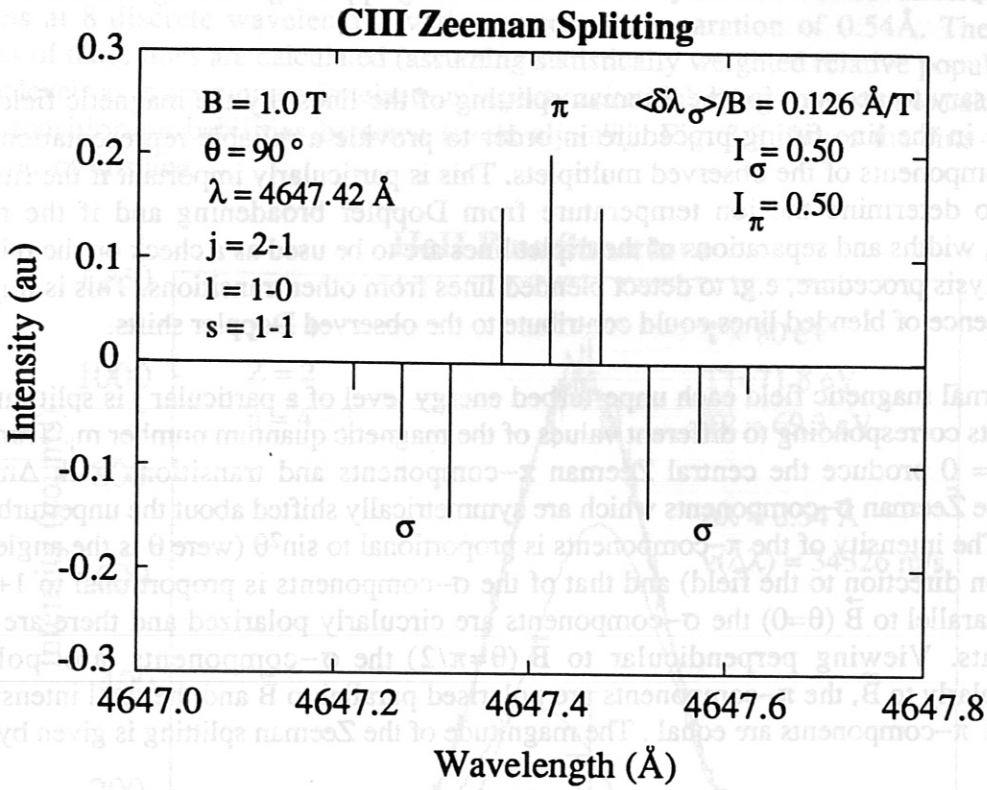

Fig. 3.4: Zeeman splitting of the most prominent CIII (λ=4647.42Å, $^3P_2$ - $^3S_1$) line in the triplet. The angle of observation to the magnetic field, θ, is π/2. The weighted mean shift of the σ-components on one side of the line centroid, relative to the unperturbed wavelength, per unit magnetic field intensity is 0.126 Å/T.

In order to know whether the radial electric field E_r can be determined directly from the measured Doppler shift of the line centroid (as discussed in Chap. 2) the radial profiles of the contributions to the line shift from the diamagnetic drift and the excitation probability gradient have to be estimated from the results of our measurements. In general E_r is to be evaluated from Equ. (2.7) which is valid for all possible values of Γ given by Equ. (2.6). To do this measurements or estimates of $\omega_i\tau_k$, T_i, n_i'/n_i and ζ_k'/ζ_k are required. In the extreme case where $\omega_i\tau_k << 1$, $\Gamma \rightarrow 0$, E_r can be evaluated from Equ. (2.8) for which only T_i and n_i'/n_i are required. In the other extreme case where $\omega_i\tau_k >> 1$, $\Gamma \rightarrow 1$, E_r can be evaluated from Equ. (2.10) for which only T_i and $\varepsilon_i'/\varepsilon_i$ are required. In the latter case, all of the information required to evaluate E_r is available from a radially resolved measurement of the line profile and relative line intensity. T_i can be obtained from the Doppler broadening of the line and $\varepsilon_i'/\varepsilon_i$ from an Abel inversion of the chord integrated intensity $I(r_o)$, where r_o is the chord impact parameter. In the former case, where $\Gamma \rightarrow 0$, additional information on the excitation rate is required to calculate the relative ground state density profile n_i'/n_i from the measured line intensities.

Here, as an example, we use the chord integrated intensity profile of the BIV (2823Å) line, measured during the Ohmic phase of an ASDEX discharge, to calculate the equivalent local

drift velocities $v_{i\perp}^*$ for the extreme cases of a) solely diamagnetic drift ($\Gamma = 0$, where $v_{i\perp}^*$ is given by the first term on the r.h.s. of Equ. (2.5)) and b) where the diamagnetic drift and the excitation probability gradient contributes to the measured line shift ($\Gamma = 1$, where $v_{i\perp}^*$ is given by the first term on the r.h.s. of Equ. (2.9)).

From the Doppler broadening of the BIV (2823Å) triplet lines observed at different radii there is evidence that the BIV ion temperature is fairly constant over the radial extent of the emission shell. In the following example, therefore, we assume a constant BIV ion temperature T_i (BIV) of 200 eV.

Fig. 3.5 shows the radial pressure profile and the local equivalent drift velocity $v_{i\perp}^*$ of the BIV ions evaluated from the relative emissivity profile ε_i obtained from an Abel inversion of the chord integrated line intensity profile measured in the Ohmic-phase of an ASDEX plasma. Values corresponding to the $\Gamma = 1$ case are shown as solid lines. In order to be able to evaluate the $\Gamma = 0$ case it is necessary to determine the relative ground state ion density profile n_g from the relative emissivity profile. This is possible provided that the excitation mechanism can be modelled for which, in this case, a knowledge of the electron temperature T_e and density n_e profiles is required. We assume that the excitation of the 2p excited state (k) is by electron impact excitation from the ^3S meta-stable level (g) and that the excitation rate coefficient χ_{gk} from the ground state g to the excited state k can be approximated by van Regemorter's formula [3.1]:

$$\chi_{gk}\,[\mathrm{cm^3 s^{-1}}] = \frac{1.6\cdot 10^{-5}\, f_{gk}\,\langle g\rangle}{\Delta E_{gk}\,\sqrt{T_e}}\; e^{-\left(\frac{\Delta E_{gk}}{T_e}\right)} \qquad (3.3)$$

Assuming Coronal population equilibrium we have:

$$\varepsilon = \frac{1}{4\pi}\, n_k\, A_{gk} = \frac{1}{4\pi}\, B\, n_e\, n_g\, \chi_{gk} \qquad (3.4)$$

$$B = \frac{A_{gk}}{\sum\limits_{l \le k} A_{lk}} \qquad (3.5)$$

where ΔE_{gk} is the energy difference between the excited state and the ground state, n_k is the excited state density, A_{lk} is the decay probability from excited state k to a state l, B is the branching ratio and n_g is the ground state density which can thus be obtained from the expression:

$$n_g = \frac{4\pi\,\varepsilon}{n_e\,\chi_{gk}\,B} \qquad (3.6)$$

Using values of T_e and n_e obtained from fits to the data from the YAG Thomson scattering system and the appropriate value for ΔE_{gk} the relative ground state density n_g has been calculated from Equ. (3.6). The calculated values of n_g and $v_{i\perp}^*$ calculated using Equ. (2.5) are shown in Fig. 3.5 (dashed lines). Note that, due to the gradients of T_e and n_e these curves are shifted a few mm outwards relative to the ε_i and $v_{i\perp}^*$ curves relevant to the $\Gamma = 1$ case. If we assume that the true ^1S ground state, rather than the ^3S meta-stable state, is the appropriate ground state for this transition we find that the /n_g and $v_{i\perp}^*$ curves calculated for the $\Gamma = 0$ case are only shifted outwards a little more with respect to the ε_i and $v_{i\perp}^*$ curves shown here. A

more accurate calculation would have to take into account the temperature and density dependence of the relative ^1S and ^3S populations.

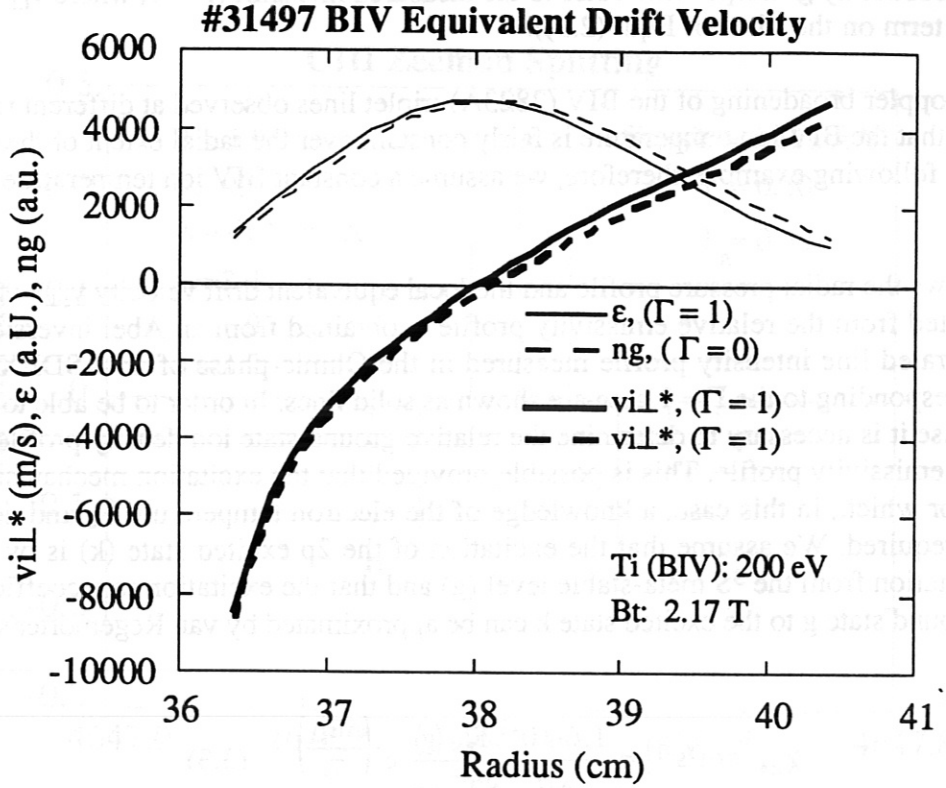

Fig. 3.5: The equivalent local drift velocity $v_{i\perp}$* calculated from the measured emissivity profile of the BIV ions during the Ohmic-phase for the cases of: $\Gamma = 0$ (pure diamagnetic drift); and $\Gamma = 1$ (with contributions from the diamagnetic drift and the gradient of the excitation probability).

In conclusion, the equivalent local drift velocity $v_{i\perp}$*, calculated in the extreme cases of $\Gamma = 0$ (pure diamagnetic drift) and $\Gamma = 0$ (with contributions from the diamagnetic drift and the gradient of the excitation probability), are equal to within the uncertainties of the measurements, at least for the Ohmic-phase of the plasma. In the case of the BIV (2823Å) triplet, Γ is estimated to be approaching unity ($\Gamma = 0.54$ at B = 2.0 T). We are, therefore, at liberty to calculate $v_{i\perp}$* using Equ. (2.9) directly from the measured emissivity profile and the Doppler broadening. The corrections required for conditions where $\Gamma << 1$ (which necessitate modelling of the excitation process) have been shown to be negligibly small in comparison with the uncertainties of our measurement of the relevant radial profiles.

4. Experiment and Accuracy:

By working in the visible spectral range it is relatively simple to achieve the resolution required to measure drift velocities of the order of 1000 ms^{-1} (Doppler shifts of $\Delta\lambda = 0.01$Å at 3000Å). Our spectrometer system [4.1] was configured to view along lines of sight through the outer part of the plasma where partially ionised impurities emit visible line radiation from radially localized emission shells. Visible light emitted from the edge region of the plasma was collimated into a 1m Czerny-Turner spectrometer using a lens, a rotatable mirror at the port entrance and two edge mirrors above and below the plasma mid-plane, as shown in Fig. 4.1. The system could thus view in either of two anti-parallel directions which were at approximately 5° to the vertical plane, perpendicular to $\vec{B}$ for typical values of q_a ($q_a \approx 3$). By moving the rotatable mirror the line of sight could be scanned from 6 cm inside to 3 cm outside the separatrix (r_{sep} = 40 cm) at the horizontal mid-plane. By using a prism to rotate the slit image by 90^0 a radial resolution of 0.5 cm was achieved. The spectrometer was equipped with (1200, 2400 and 3600) lmm^{-1} gratings and a 1024 channel, intensified photo-diode array detector (OMA) which provided spectra at 20 ms intervals. The dispersion of the instrument at 4650 Å is (7.62, 3.11 and 1.17) $Åmm^{-1}$ or (0.192, 0.078 and 0.029) $Åpix^{-1}$ in first order (where the three values refer to the gratings listed above).

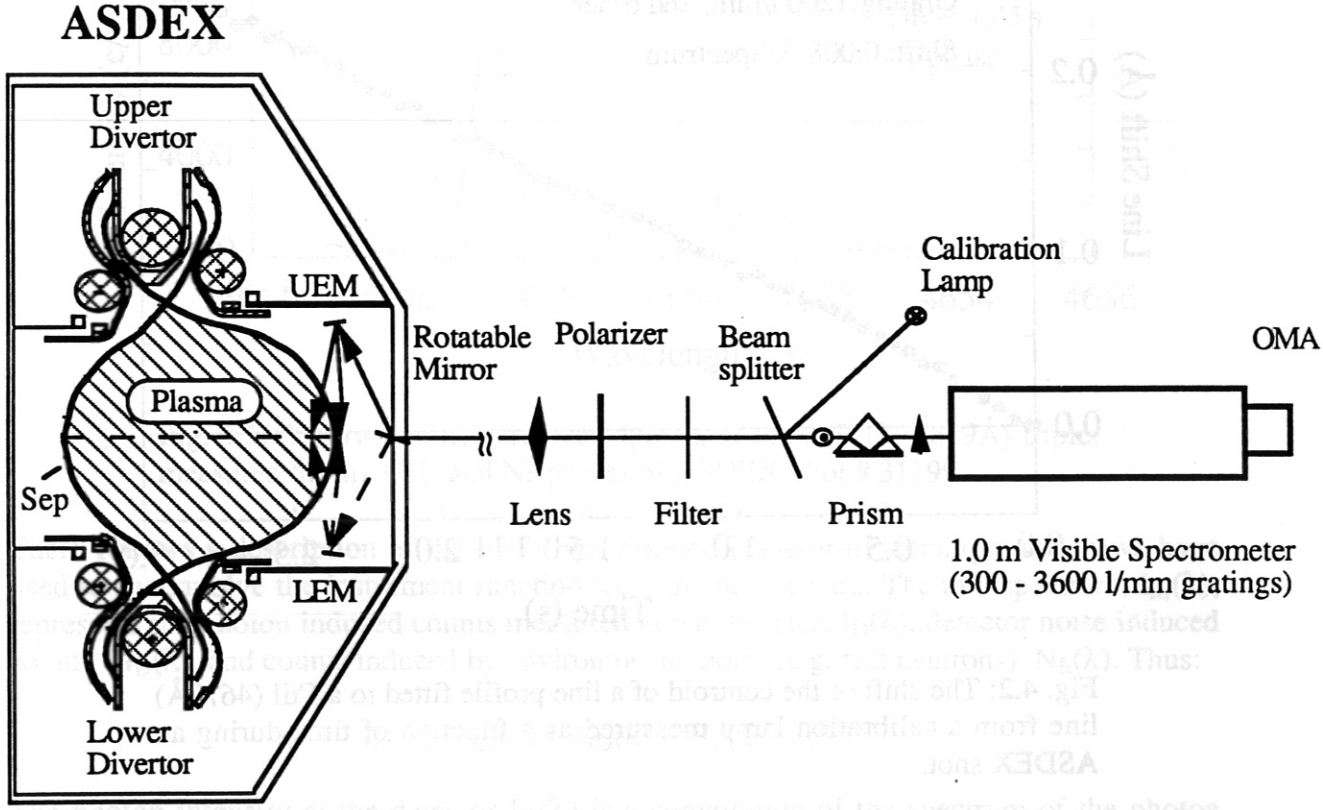

Fig. 4.1: Experimental setup used for spectroscopic measurements of the impurity ion drift velocities in ASDEX.

Contributions to the spectra from lower wavelength lines in higher orders were suppressed using a filter. Additional broadening due to Zeeman splitting was suppressed by removing the σ-components (which are polarised $\perp\vec{B}$ when viewing $\perp\vec{B}$) with a polariser. However, this was not absolutely necessary as both the π- and σ-components could be accounted for in the line fitting procedure. To provide an absolute wavelength reference, Hg- and Cd-lines from calibration lamps were measured simultaneously via a beam splitter. This was particularly

necessary as the system could not view simultaneously along two opposing directions, thus, a simultaneous measurement of the differential Doppler shift was not possible.

The accuracy of the line shift measurements and of the data analysis has been checked using several techniques. Firstly, a measured spectrum of the C III (4649Å) triplet was deconvolved using a FFT technique, described in Chap. 5, and then fitted with an appropriate line profile. The weighted mean of the shift of the centroid of the fitted line profile from a reference wavelength could be determined to an accuracy of ± 0.005 Å corresponding to a velocity uncertainty of ± 300 ms^{-1}. Secondly, a continuous line shift measurement was performed by measuring a CdI (4678Å) line from a calibration lamp and then turning the grating slowly during an ASDEX shot. The resulting shift of the centroid of the fitted line profile shows that a line shift can be measured to an accuracy of ±0.01 Å, which corresponds to a velocity uncertainty of ±800 ms^{-1}, see Fig. 4.2. An analogous blue shift was observed when the grating was turned in the opposite direction.

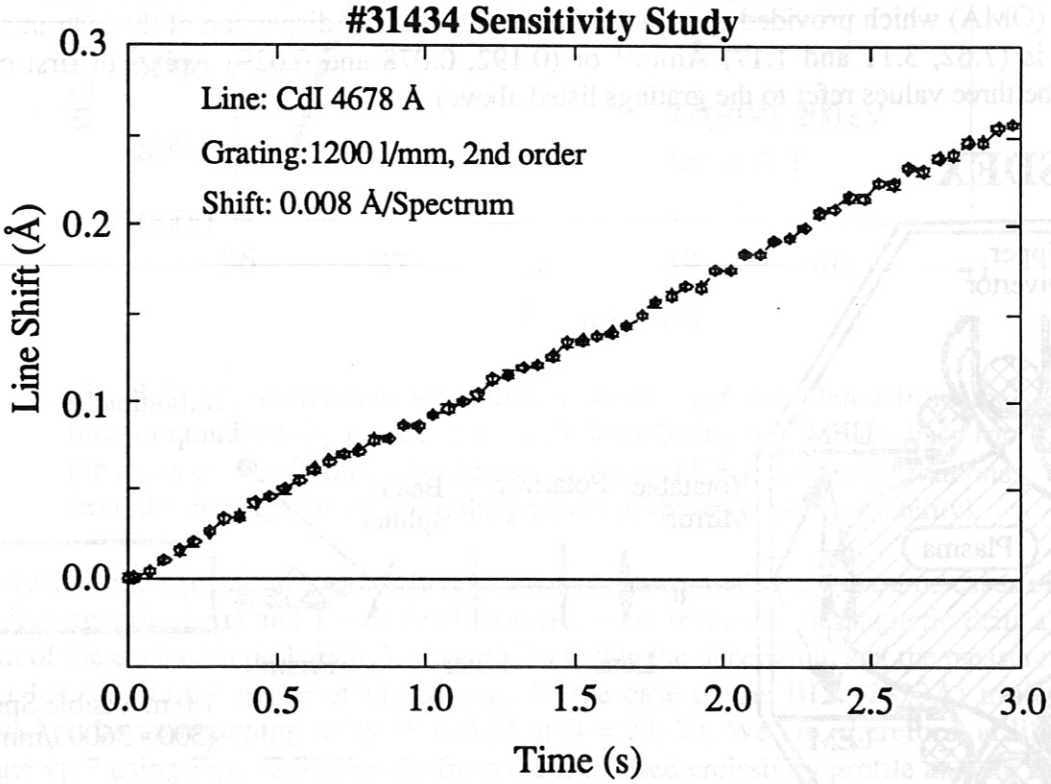

Fig. 4.2: The shift of the centroid of a line profile fitted to a CdI (4678Å) line from a calibration lamp measured as a function of time during an ASDEX shot.

The radial emission profiles of the ionic species were measured either by shifting the plasma radially during the shot whilst measuring at a fixed radial position, or by scanning the rotatable mirror several times during the shot. In addition, in the case of the B IV lines, radial profile measurements were performed by moving the rotatable mirror between shots. In particular, these shot-to-shot measurements enabled the radial emissivity profiles to be measured during the short L- and H*-phases of the shots during which measurements could not be performed by scanning the mirror.

5. Analysis Procedure:

Typical 'raw' spectra of the CIII (λ=4649Å) triplet measured with a 2400 lmm^{-1} grating in 1st order during OH- and NI-phases (NI: Co, 2.0 MW / 1.35 MW, $D^o \rightarrow D^+$, 1.0-1.7 s), are shown in Fig. 5.1(a). These spectra were measured during 20 ms periods of the ASDEX discharge #31199 viewing $\perp \vec{B}$ from the upper edge mirror (UEM) using a polariser to remove the Zeeman σ–components.

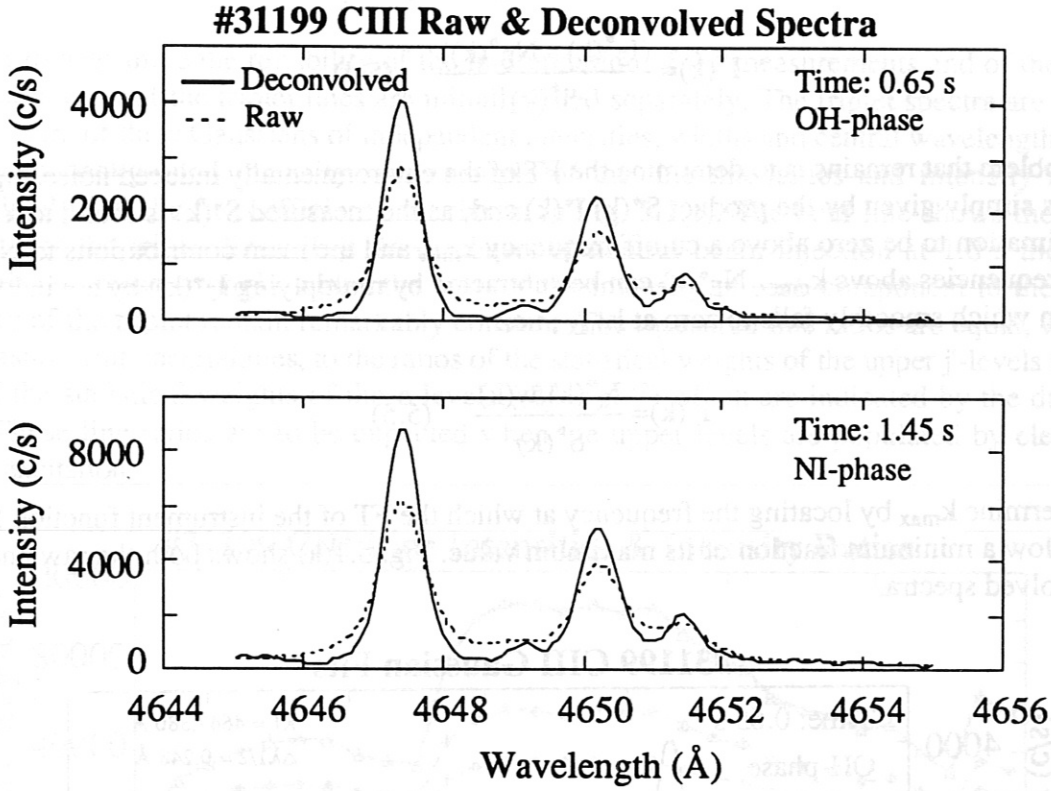

Fig. 5.1(a): Raw and deconvolved spectra of the CIII (λ=4649Å) triplet measured during OH- and NI-phases of ASDEX Shot # 31199.

There follows a description of the FFT (Fast Fourier Transform) technique which we have used to deconvolve the instrument function from the raw spectra. The raw spectrum, $I_M(\lambda)$, represents the photon induced counts measured at the detector, $I_D(\lambda)$, detector noise induced counts, $N_D(\lambda)$, and counts induced by environmental noise (e.g. fast neutrons), $N_E(\lambda)$. Thus:

$$I_M(\lambda) = I_D(\lambda) + N_D(\lambda) + N_E(\lambda) \quad (5.1)$$

The photon intensity at the detector $I_D(\lambda)$ is a convolution of the spectrum of the photon intensity entering the spectrometer $I(\lambda)$, which we wish to measure, and the response function $S(\lambda)$ of the instrument (consisting of the spectrometer and the detector) to an incident δ-function spectrum (the instrument function):

$$I_D(\lambda) = I(\lambda) \otimes S(\lambda) \quad (5.2)$$

$S(\lambda)$ has been measured for all of the gratings and spectrometer slit widths used by recording the spectra of narrow lines from calibration lamps under conditions where the number of noise induced counts ($N_D(\lambda)$ and $N_E(\lambda)$) was low.

A background spectrum $N_B(\lambda)$, recorded just before the plasma discharge, is subtracted from the raw spectrum as this is found to be a good approximation to the detector noise recorded during the shot (i.e. $N_D(\lambda) \approx N_B(\lambda)$). Thus:

$$I_S(\lambda) = I_M(\lambda) - N_B(\lambda) \approx I_D(\lambda) + N_E(\lambda) \quad (5.3)$$

By taking the Fourier transform (FT) of $I_S(\lambda)$, $I_S^*(k)$, the spectrum of light entering the instrument can be computed from its FT which is given by:

$$I^*(k) = \frac{(I_S^*(k) - N_E^*(k))}{S^*(k)} \quad (5.4)$$

The problem that remains is to determine the FT of the environmentally induced noise, $N_E^*(k)$. $I_S^*(k)$ is simply given by the product $S^*(k)\, I^*(k)$ and, as the measured $S^*(k)$ is found to a good approximation to be zero above a cutoff frequency k_{max} and the main contributions to $N_E^*(k)$ are at frequencies above k_{max}, $N_E^*(k)$ can be subtracted by multiplying $I_S^*(k)$ by a windowing function which smoothly falls to zero at k_{max} , i.e.:

$$I^*(k) = \frac{I_S^*(k)\, w(k)}{S^*(k)} \quad (5.5)$$

We determine k_{max} by locating the frequency at which the FT of the instrument function $S^*(k)$ falls below a minimum fraction of its maximum value. Fig. 5.1(a) shows both the raw and the deconvolved spectra.

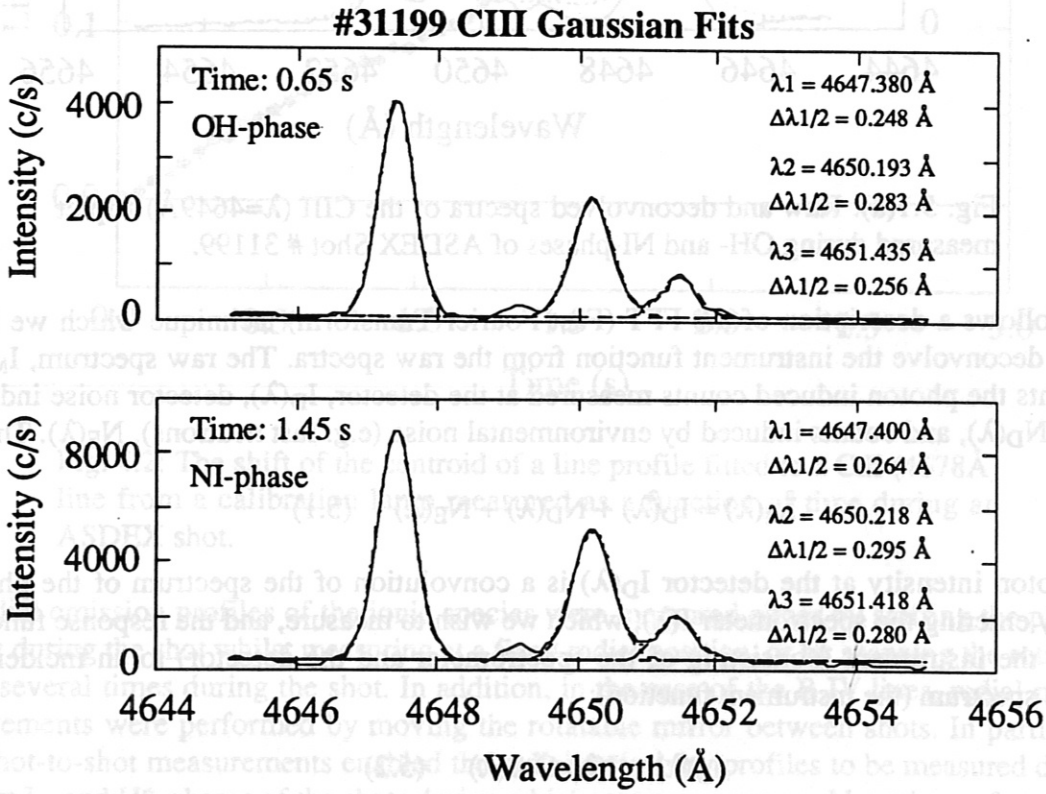

Fig. 5.1(b): Triple Gaussian fits to deconvolved CIII (λ=4649Å) triplet spectra measured during the OH- and NI-phases of ASDEX Shot # 31199.

After performing the deconvolution the spectra are fitted with an appropriate sum of several Gaussians and constant background intensity. The fitting procedure utilizes a non-linear, weighted least squares fitting procedure which determines the coefficients of the fitted function and their uncertainties [5.1], see Fig. 5.1(b). To avoid the complication of having to propagate the measurement uncertainties through the FFT procedure it is assumed that the uncertainties of the deconvolved spectral intensities can be calculated from the square root of the number of counts per channel in the deconvolved spectra, i.e. Poisson statistics are assumed for the deconvolved rather than the raw spectra.

In order to determine the reliability of the interpretation of the measurements and of the data evaluation, each of the triplet lines are initially fitted separately. The triplet spectra are fitted with the sum of three Gaussians of independent intensities, widths and central wavelengths and a constant background intensity. An example of the line intensities and intensity ratios determined from the fit coefficients are shown in Fig. 5.1(c). The bold line shows the total intensity of the triplet lines (I+). At the onset of neutral beam injection at 1.0 s the line intensities increase strongly whilst the ratio of the intensity of each component to the total intensity of the triplet remain remarkably constant. The measured line ratios are equal, within the measurement uncertainties, to the ratios of the statistical weights of the upper j'-levels to the sum of the statistical weights of these levels ($(2j'+1)/n'^2$) which are indicated by the dashed lines. These line ratios are to be expected when the upper levels are populated by electron impact excitation.

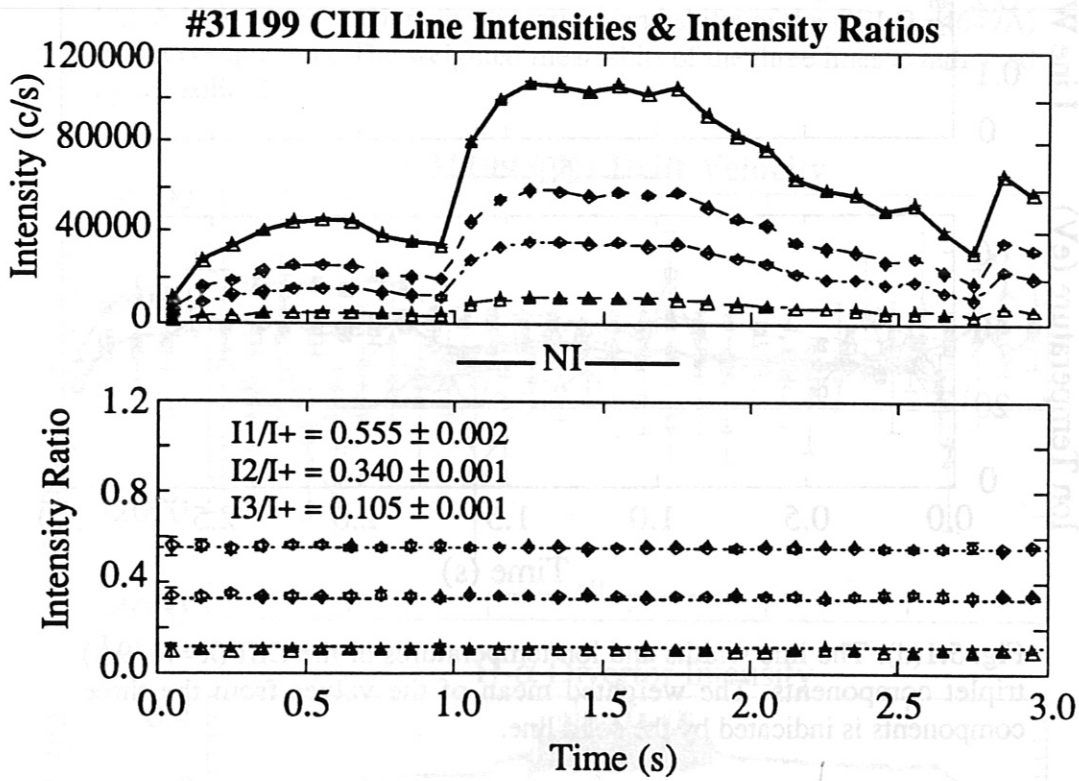

Fig. 5.1(c): The measured intensities of the CIII (λ=4649Å) triplet lines and their sum, I+ (represented by the solid line). Below are shown the ratios of the triplet line intensities to the total triplet intensity. The ratios of the statistical weights of the upper j'-levels are indicated by the dashed lines.

The line widths and ion temperatures obtained for each triplet component remain reasonably equal throughout the entire shot as is shown in Fig. 5.1(d). The bold lines show the weighted means, over the triplet components, of the line widths and the ion temperature. Note that no increase of the ion temperature during the NI-phase, relative to that during the Ohmic-phase, is observed. This is understood as being a consequence of the competition between the collisional heating and the ionisation of the CIII ions (as discussed in Chap. 2) which does not allow the CIII ions to reach temperatures much in excess of 40 eV. Furthermore, the CIII emission shell moves radially outwards during the NI-phase, perhaps into a region of reduced background ion temperature.

As shown in Fig. 5.1(e), the wavelength separations of the Gaussians fitted to the triplet lines remain constant and equal, within the measurement uncertainties, to tabulated values [5.2]. The shifts of the centroid wavelengths of the fitted Gaussians (relative to their mean values over the time period from 0.0 to 1.0 s), also shown in Fig. 5.1(e), show a small shift to longer wavelengths of about 0.01Å to 0.02Å during the NI-phase. The bold line shows the weighted mean of the shifts of the three components.

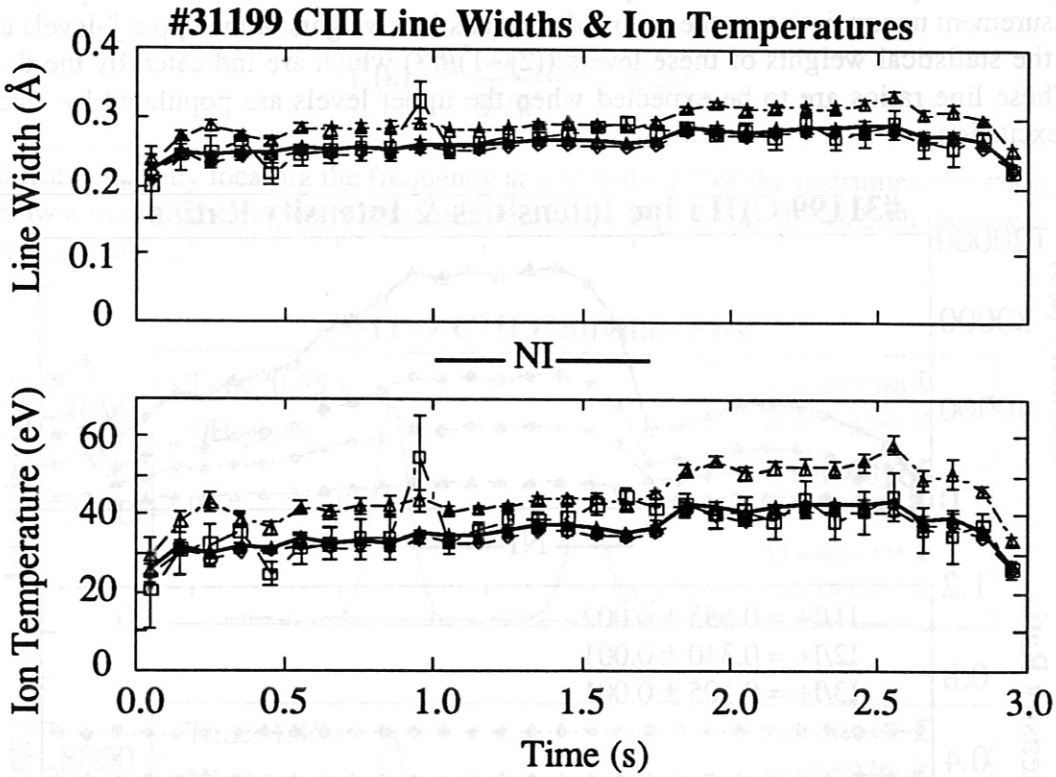

Fig. 5.1(d): The line widths and ion temperatures of the CIII (λ=4649Å) triplet components. The weighted mean of the values from the three components is indicated by the solid line.

Finally, Fig. 5.1(f) shows the drift velocity of the CIII ions as determined from the shifts of the centroid wavelengths of the fitted Gaussians (relative to their mean values over the time period from 0.0 to 1.0 s) and the H-α intensity measured in the divertor, which is used to identify the H-phase. After the onset of the neutral beam injection at 1.0 s the H-α intensity rises, indicating the L-phase. At about 1.15 s the transition into the H-phase occurs, indicated by a sudden drop of the H-α intensity. During the H-phase very frequent ELMs occur. We therefore call this a 'grassy' H-phase rather than a quiescent (ELM-free) H*-phase.

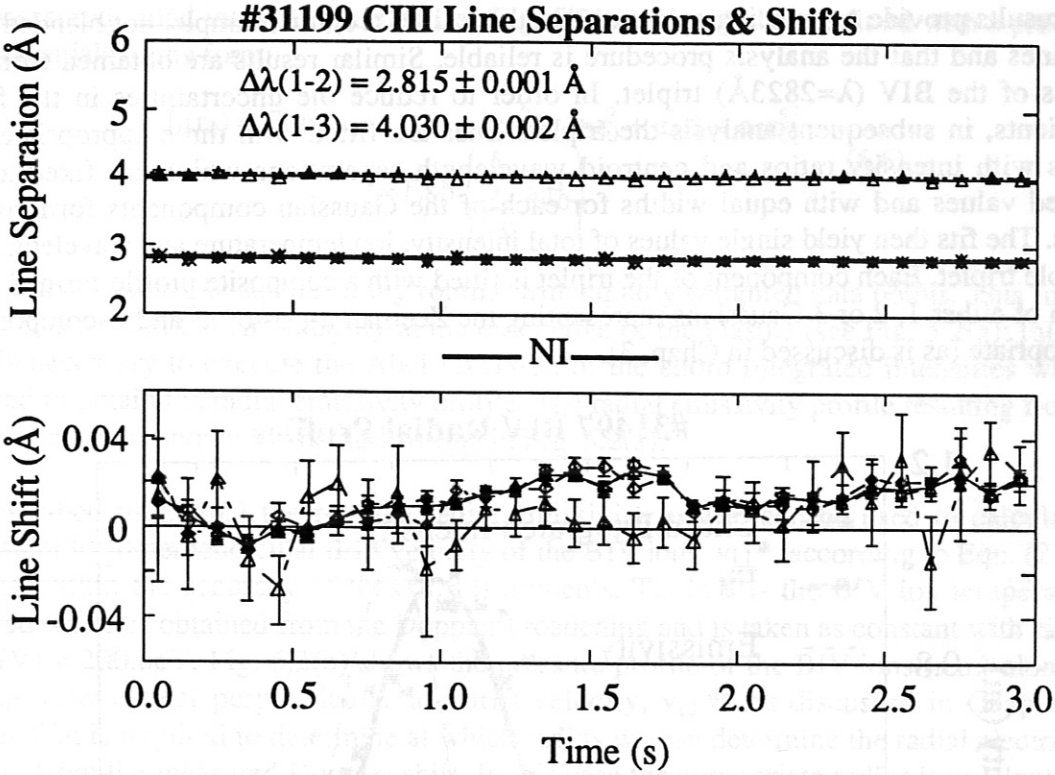

Fig. 5.1(e): Line wavelength separations and shifts of the CIII (λ=4649Å) triplet components. The weighted mean shift of the three lines is indicated by the solid line.

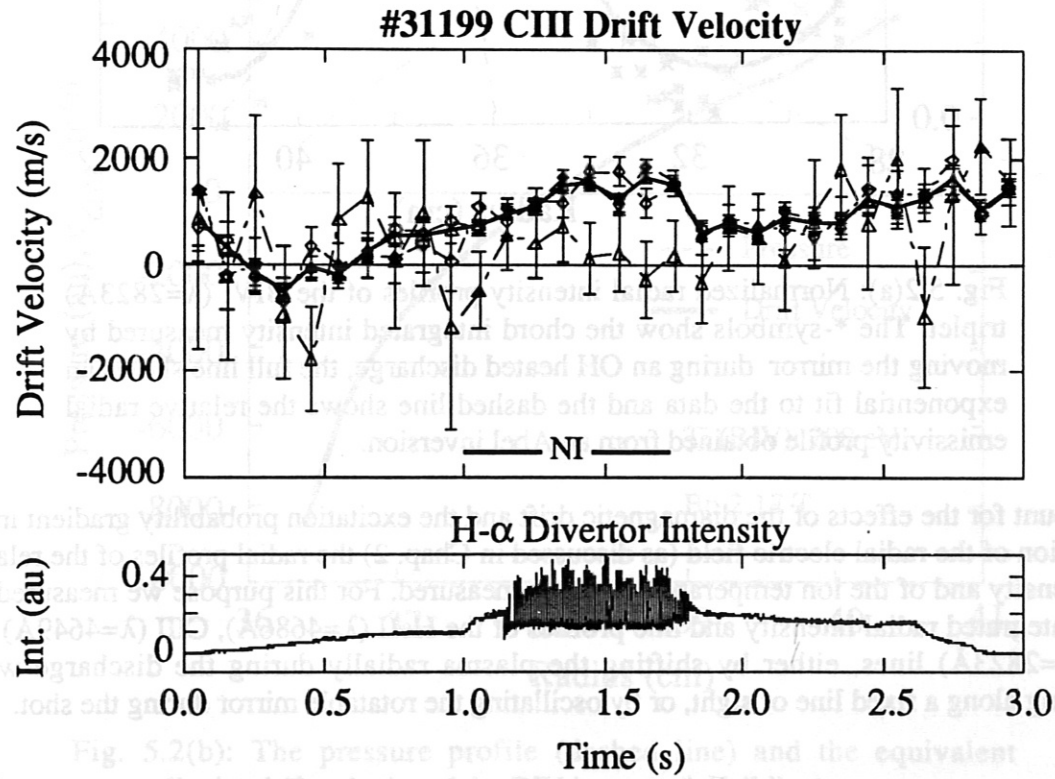

Fig. 5.1(f): Drift velocities of the CIII ions derived from the wavelength shifts of the CIII (λ=4649Å) triplet lines. The weighted mean of the drift velocity derived from the wavelength shift of the three lines is indicated by the solid line.

These results provide convincing evidence that these lines are, for example, not blended with other lines and that the analysis procedure is reliable. Similar results are obtained from the analysis of the BIV (λ=2823Å) triplet. In order to reduce the uncertainties in the fitted coefficients, in subsequent analysis the triplets lines are fitted with three appropriate line profiles with intensity ratios and centroid wavelength separations which are fixed at the tabulated values and with equal widths for each of the Gaussian components forming the profiles. The fits then yield single values of total intensity, ion temperature and wavelength for the whole triplet. Each component of the triplet is fitted with a composite profile formed from the sum of either 1, 2 or 3 Gaussians representing the Zeeman π-, σ- or π- and σ-components as appropriate (as is discussed in Chap. 3).

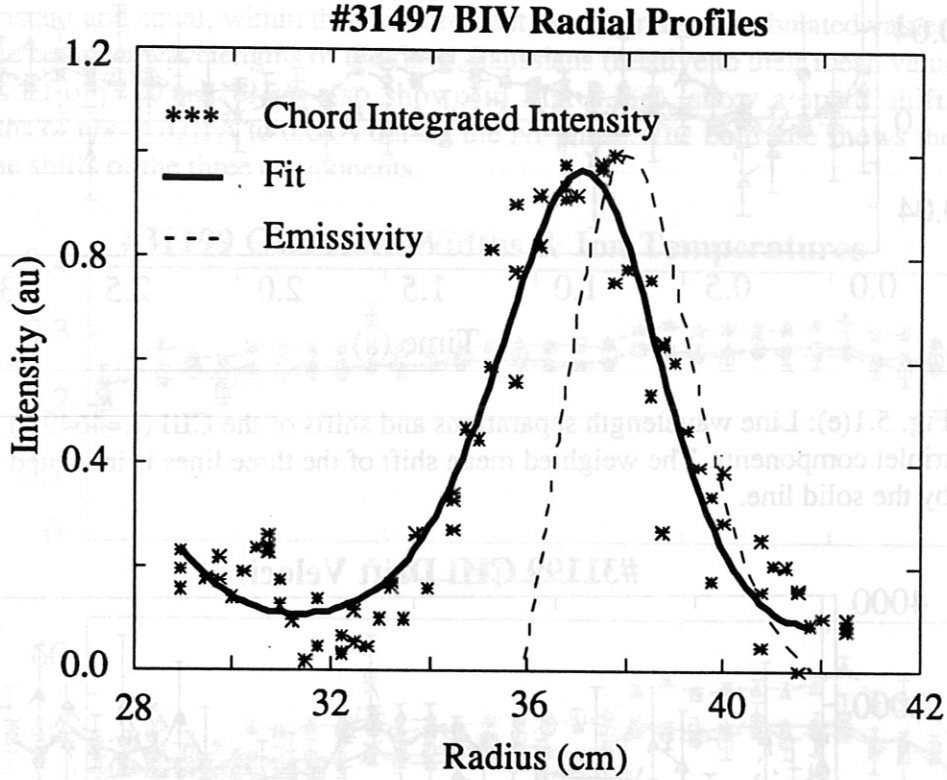

Fig. 5.2(a): Normalized radial intensity profiles of the BIV (λ=2823Å) triplet. The *-symbols show the chord integrated intensity measured by moving the mirror during an OH heated discharge, the full line shows an exponential fit to the data and the dashed line shows the relative radial emissivity profile obtained from an Abel inversion.

To account for the effects of the diamagnetic drift and the excitation probability gradient in the calculation of the radial electric field (as discussed in Chap. 2) the radial profiles of the relative line intensity and of the ion temperature must be measured. For this purpose we measured the chord integrated radial intensity and line profiles of the HeII (λ=4686Å), CIII (λ=4649Å) and BIV (λ=2823Å) lines, either by shifting the plasma radially during the discharge while measuring along a fixed line of sight, or by oscillating the rotatable mirror during the shot.

The measured radial intensity profiles (see Fig. 5.2(a), *-symbols) are fitted with a product of 6 exponentials of the form:

$$I_r(r_0) = \mathrm{Exp}\left\{a_0 + a_1 r_0 + a_2 r_0^2 + a_3 r_0^3 + a_4 r_0^4 + a_5 r_0^5\right\} = \mathrm{Exp}\left\{\sum_{i=0}^{5} a_i r_0^i\right\} \quad (5.6)$$

using a non-linear least square fitting routine with equally weighted data points. This function is then normalized to zero intensity at the outer edge of the plasma (see Fig. 5.2(a): full line). This is necessary to execute the Abel inversion of the chord integrated intensities which is required to obtain the radial emissivity profile. The radial emissivity profile resulting from this Abel inversion is shown by the dashed line in Fig. 5.2(a).

As described in Chap.3 the relative radial emissivity profile can be used to calculate the equivalent local perpendicular drift velocity of the BIV ions, $v_{i\perp}$*, according to Equ. (2.10), at least to within the accuracy of these measurements. To do this the BIV ion temperature is required which is obtained from the Doppler broadening and is taken as constant with radius at T_i (BIV) = 200.0eV. Fig. 5.2(b) shows the pressure profile of the BIV ions (a.u.) along with the equivalent local perpendicular ion drift velocity, $v_{i\perp}$*. As discussed in Chap. 2, this information is required to determine at which radius we can determine the radial electric field directly from the measured Doppler shift. In this case the appropriate radius is at about r = 37 cm, just inside the radius of the maximum of the emissivity.

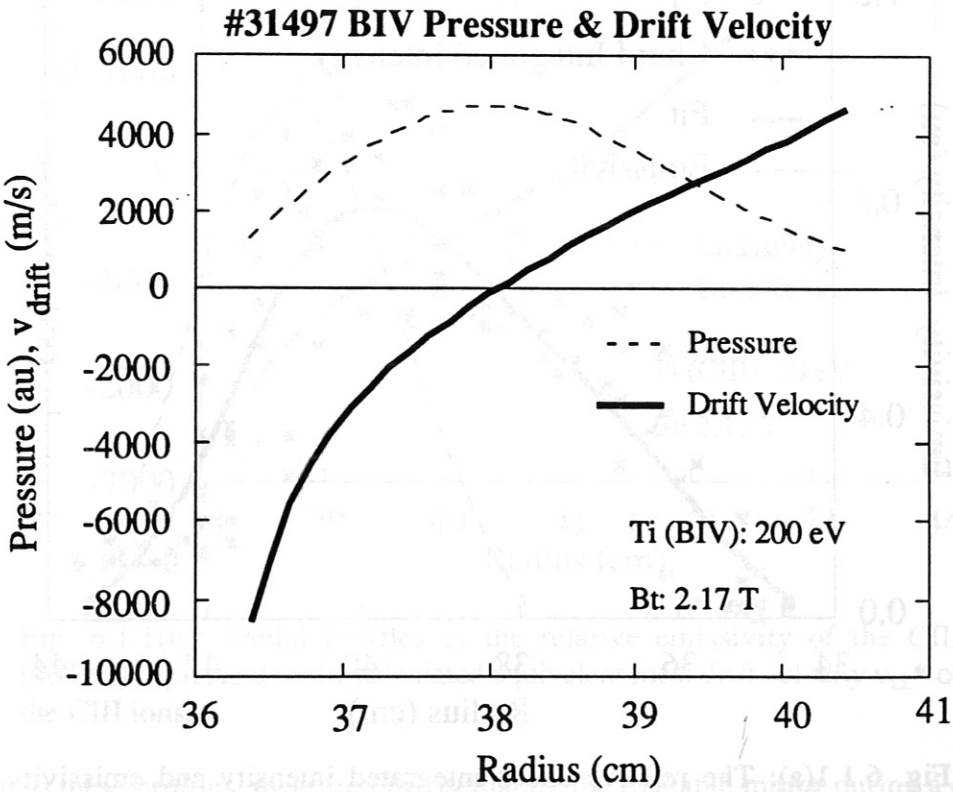

Fig. 5.2(b): The pressure profile (dashed line) and the equivalent perpendicular drift velocity of the BIV ions, $v_{i\perp}$* (full line).

6. Results:

This chapter presents the results of our measurements on the BIV, CIII and HeII ions. Most of the results presented are from measurements made using the BIV (2823Å) triplet lines as these measurements have yielded the most useful information for the evaluation of the radial electric field within the thermal barrier of the H-mode plasma, just inside the separatrix. The temporal and parametric dependencies (NBI-heating power, Co- and Ctr-directions of NBI, I_p and B_t) of the BIV ion drift velocities are presented and these results used to evaluate these same dependencies for the radial electric field. The results are briefly discussed in terms of neo-classical theories of poloidal momentum damping and poloidal rotation.

6.1. Radial Profiles:

Knowledge of the radial emissivity profiles of the observed lines is required to determine the appropriate line of sight along which to observe in order to determine the radial electric field from a direct measurement of the observed Doppler shift. Measurements of the emissivity profiles of the C III (4649Å), B IV (2823Å) and He II (4686Å) multiplets were performed both by shifting the plasma and viewing along a fixed line of sight and by oscillating the rotatable mirror during the Ohmic-phase of the plasma. The measured radial emissivity profiles of the CIII (4649Å), B IV (2823Å) and He II (4686Å) multiplets presented below were measured using the latter technique.

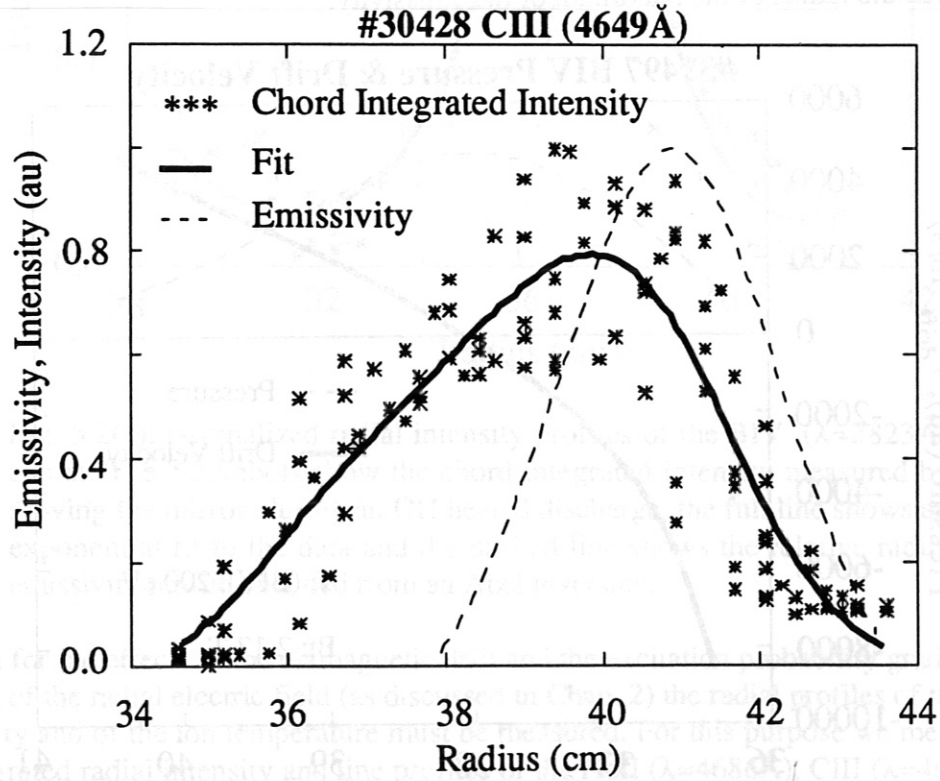

Fig. 6.1.1(a): The relative chord integrated intensity and emissivity profiles of the CIII (4649Å) triplet measured during the Ohmic-phase of the plasma.

From these measurements the maximum of the C III (4649Å) line emissivity is found to be located at the separatrix (r_{sep} = 40 cm) to an accuracy of about ± 1 cm. The radial extent of the emission shell is about 4 cm FWHM (full width at half maximum), as shown in Fig. 6.1.1(a). The B IV (2823Å) emission shell is located further inside the plasma at a radius of 38±1 cm and has a radial extent of about 3 cm FWHM, as shown in Fig. 5.2(a). He II (4686Å) emission shell is located at the same radial position as the B IV (2823Å) emission, see Fig. 6.1.2(a). In case of B IV (2823Å) and He II (4686Å) the apparent perpendicular drift velocities $v_{i\perp}$* calculated from the emissivity profiles vary quite strongly within ± 2 cm of the maximum of the pressure profiles. Values of $v_{i\perp}$* are calculated as $8 \cdot 10^3$ ms^{-1} at a position 2 cm inside and $4 \cdot 10^3$ ms^{-1} at a position 2 cm outside the radius of the maximum emissivity, see Figs. 5.2(b) and 6.1.2(b). Due to the effect of the integration along the line of sight, as shown in Figs. 2.2, when measuring along chords of impact radii just inside that of the peak of the emissivity profile, the measured perpendicular drift velocity $v_{i\perp m}$* does not represent the high local values of $v_{i\perp}$*. This is because of cancellation of oppositely Doppler shifted components of the emission from the inner and outer sides of the shell. Therefore, when measuring at impact radii just less than that of the maximum emissivity, this contribution to the observed Doppler shift remains small and E_r may be infered directly from the measured shift.

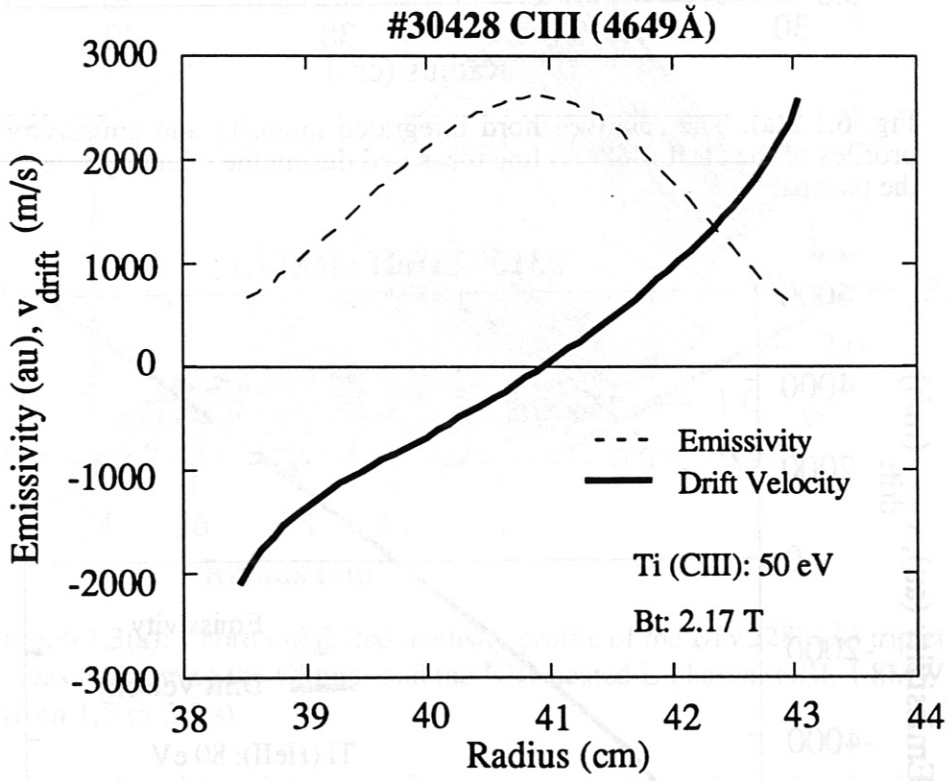

Fig. 6.1.1(b): Radial profiles of the relative emissivity of the CIII (4649Å) triplet and of the calculated equivalent local drift velocity $v_{i\perp}$* of the CIII ions.

In addition to these profiles, measured by oscillating the rotatable mirror during a discharge, radial profiles were also obtained by shifting the plasma radially by ± 5 cm around its normal position whilst viewing along a fixed line of sight. The resulting radial profiles are in very good agreement with those measured by oscillating the mirror. By using this technique these profiles could be measured over a greater range of radii than by oscillating the mirror.

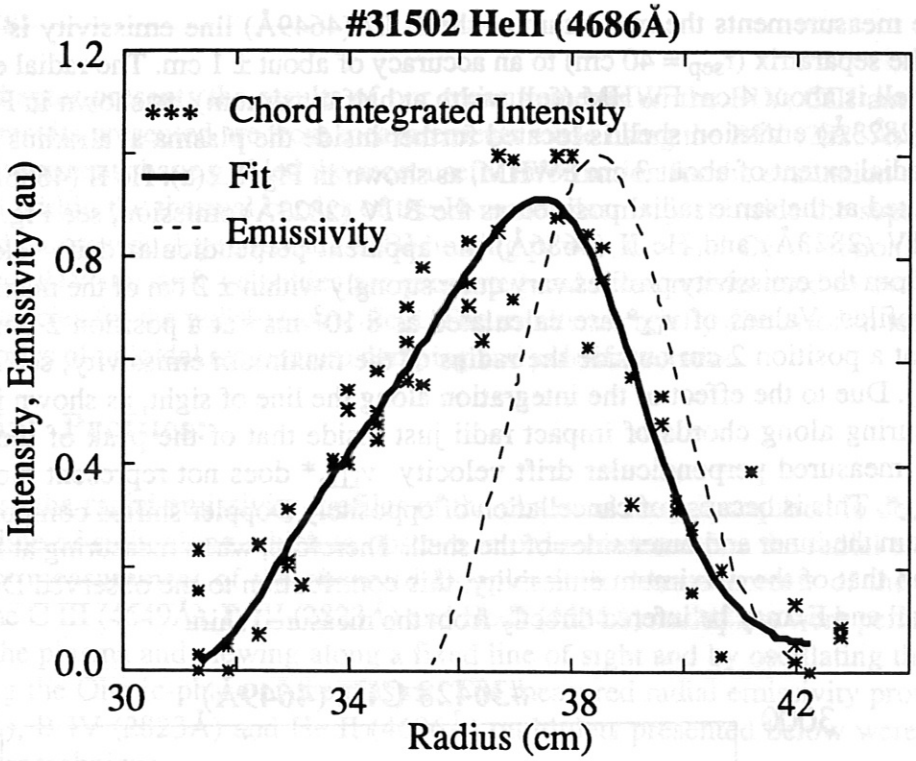

Fig. 6.1.2(a): The relative chord integrated intensity and emissivity profiles of the HeII (4686Å) line measured during the Ohmic-phase of the plasma.

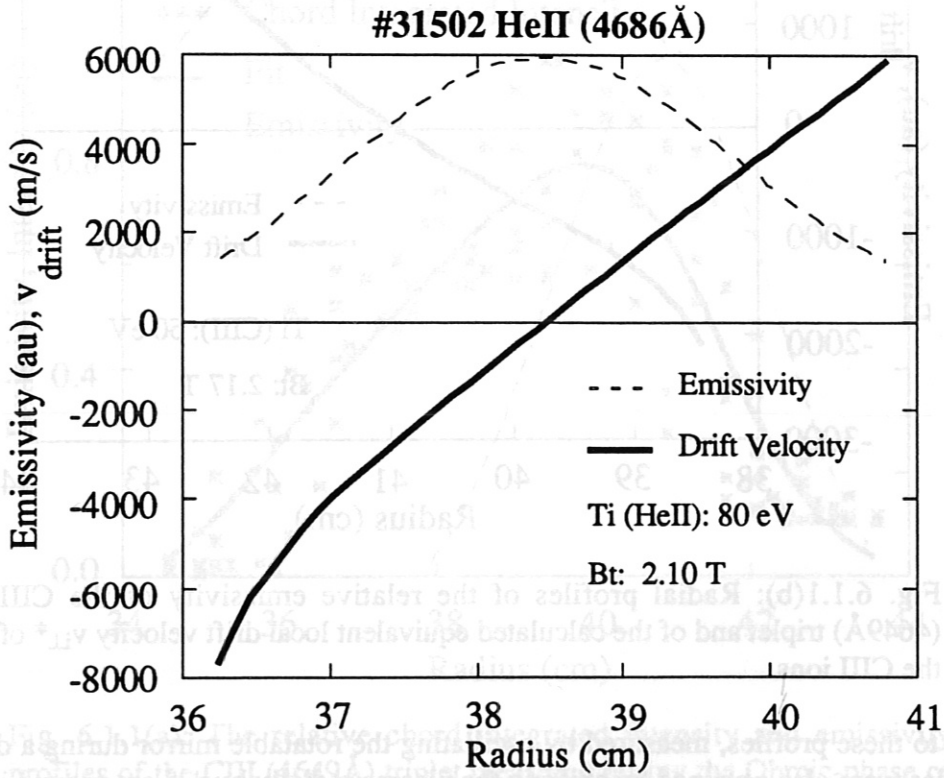

Fig. 6.1.2(b): Radial profiles of the relative emissivity of the HeII (4686Å) line and of the calculated equivalent local drift velocity $v_{i\perp}$* of the HeII ions.

For the Ohmic-phase, these profiles can be used to determine the observation direction such that the radial electric field can be determined directly from the measured Doppler shift. Unfortunately, we cannot use the techniques described above to measure the emissivity profiles during H*-phase as these phases are too short to allow the multiple sweeps of the mirror required to perform measurements during the occurence of temporal intensity variations. Therefore, in order to estimate the correct observation direction for performing these measurements in the NBI heated phases we have performed shot-to-shot measurements of the radial emissivity profile of BIV (2823Å). From these measurements an estimate of the outward shift of the emission shells can be made. Chord integrated intensity profiles were obtained by measuring along chords of different fixed impact radii during successive similar shots. Fig. 6.1.3(a) shows the time dependence of the BIV (2823Å) intensity profile measured in this way for NBI heated plasmas (P_{NI} = 1.8 MW) with only Ohmic and L-phases. Unfortunately, during the NBI phase it is not possible to perform an Abel inversion of these profiles as the measurements were not extended out to a sufficiently large radius.

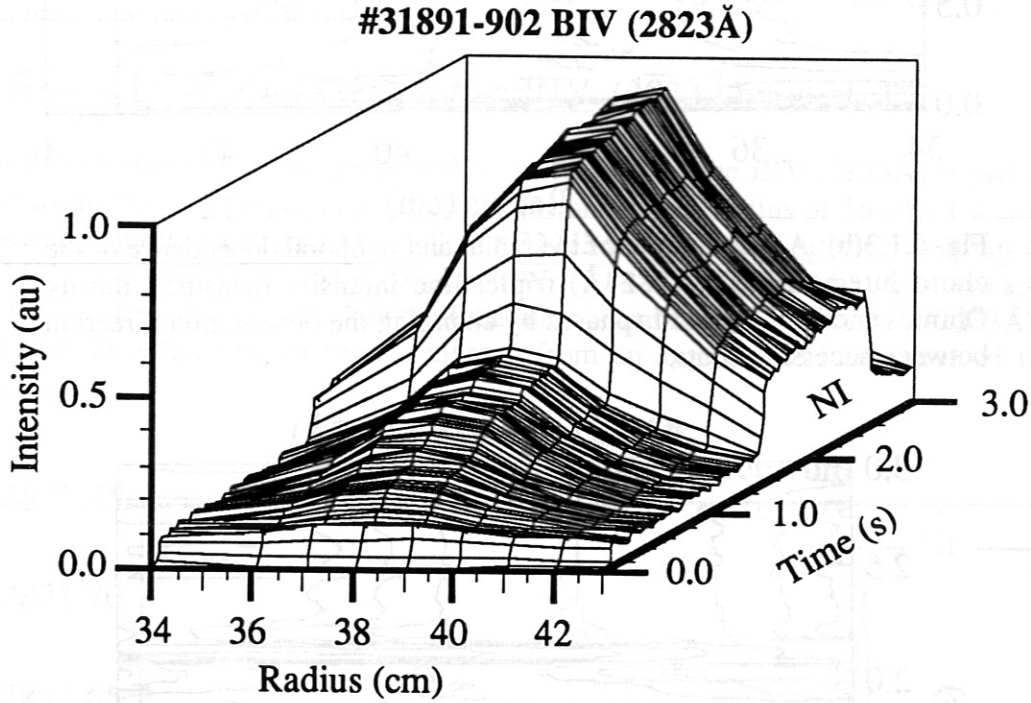

Fig. 6.1.3(a): Chord integrated intensity profile of the BIV (2823Å) triplet measured during the Ohmic- and the NBI-heated L-phases (NBI, 1.8MW from 1.5 to 2.5 s).

To visualise the radial shifs of these profiles a contour plot of these data is shown in Fig. 6.1.3(b). This shows that the emission shell moves radially outwards by about 1 cm and broadens assymetrically towards the outer side during the L-phase compared with the Ohmic-phase. During the H-phase, however, the profiles shift outwards even more. From shot-to-shot measurements of the BIV (2823Å) triplet on plasmas with Ohmic-, L- and H*-phases we see that the emission shell moves outwards by 2 cm during the H-phase compared to it's position during the Ohmic phase, as is shown in Fig. 6.1.3(c). These profiles were measured in plasmas with $D^0 \rightarrow D^+$ Co-injection which often ended by disrupting, therefore, this contour plot is meaningful only at times until the end of the injection phase at 1.7 s.

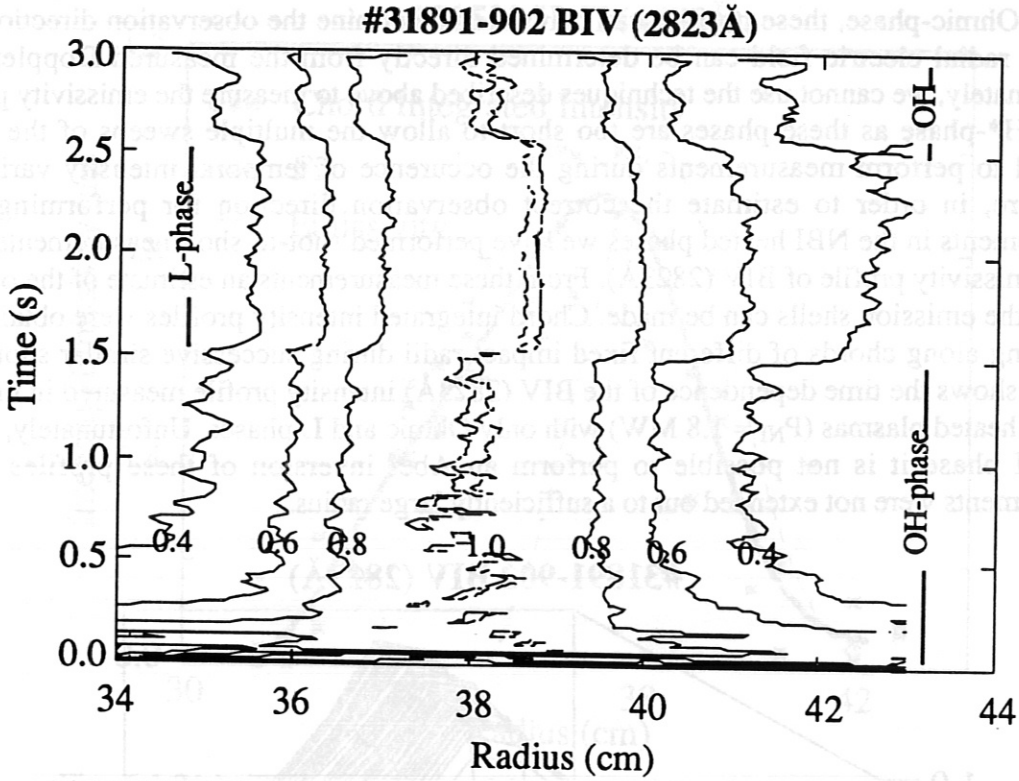

Fig. 6.1.3(b): A contour plot of the radial and temporal dependence of the chord integrated BIV (2823Å) triplet line intensity measured during Ohmic- and NBI-heated L-phases by changing the observation direction between sucessive shots.

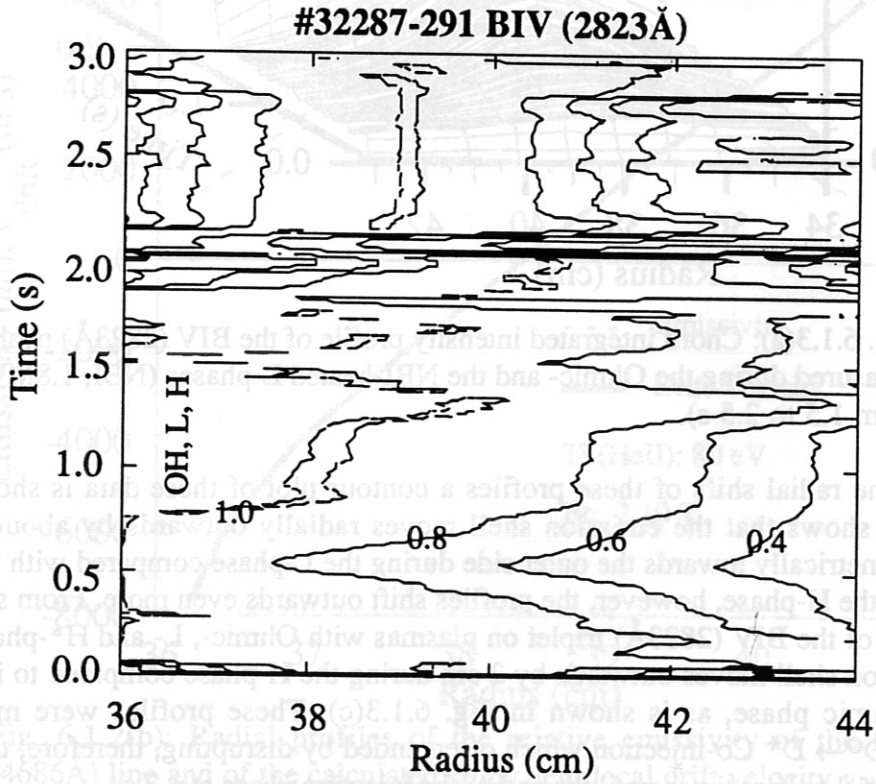

Fig. 6.1.3(c): A contour plot of the radial and temporal dependence of the chord integrated BIV (2823Å) triplet line intensity measured during Ohmic-, L- and H*-phases by changing the observation direction between sucessive shots (NBI, 2.5 MW from 1.2 to 1.7 s).

6.2 Results from Measurements on the BIV Ions:

Of the impurity lines investigated the BIV (2823Å) triplet lines have proved the most useful for determining the radial electric field within the thermal barrier of the H-mode, just within the separatrix. The reasons for this have been discussed earlier. In this section we present the results of measurements of the BIV ion drift velocities beginning in Sect. 6.2.1 with a full set of results from the analysis of data measured viewing perpendicular to $\vec{B}$ during a typical NBI heated shot which exhibits the H*-mode. The line centriod wavelength shift, deconvolved and fitted spectra, triplet intensities, line widths and BIV ion temperatures and perpendicular drift velocities are presented. In Sect. 6.2.2 time histories of components of the BIV ion drift velocity measured in poloidal, perpendicular (to $\vec{B}$) and toroidal directions are presented. In each case, measurements made viewing along two opposing lines of sight during successive similar shots are shown. From these measurements an estimate of the absolute drift velocity which is largely independent of instrumental drifts can be made. From such sets of measurements we are able to construct the BIV ion drift velocity vector at the plasma periphery during a particular phase of the plasma.

6.2.1 Example of Analysis of the BIV (2823Å) Spectra:

In this section results are presented from analysis of the BIV (2823Å) triplet spectra recorded whilst viewing perpendicular to $\vec{B}$, at a chord impact radius of 36 cm (4-6 cm inside the separatrix), during a typical ASDEX Shot # 32273 with NBI heating which exhibits Ohmic-, L- and H*-phases (Co-NBI, $D^0 \rightarrow D^+$, 2.3 MW,1.2 → 1.7 s B_t = 1.74 T, I_p = 280 kA). Fig. 6.2.1 (a) shows the centroid wavelength of the most prominant line of the BIV (2823Å) triplet at 2821.68Å as a function of time evaluated from an appropriate integration of the raw spectrum.

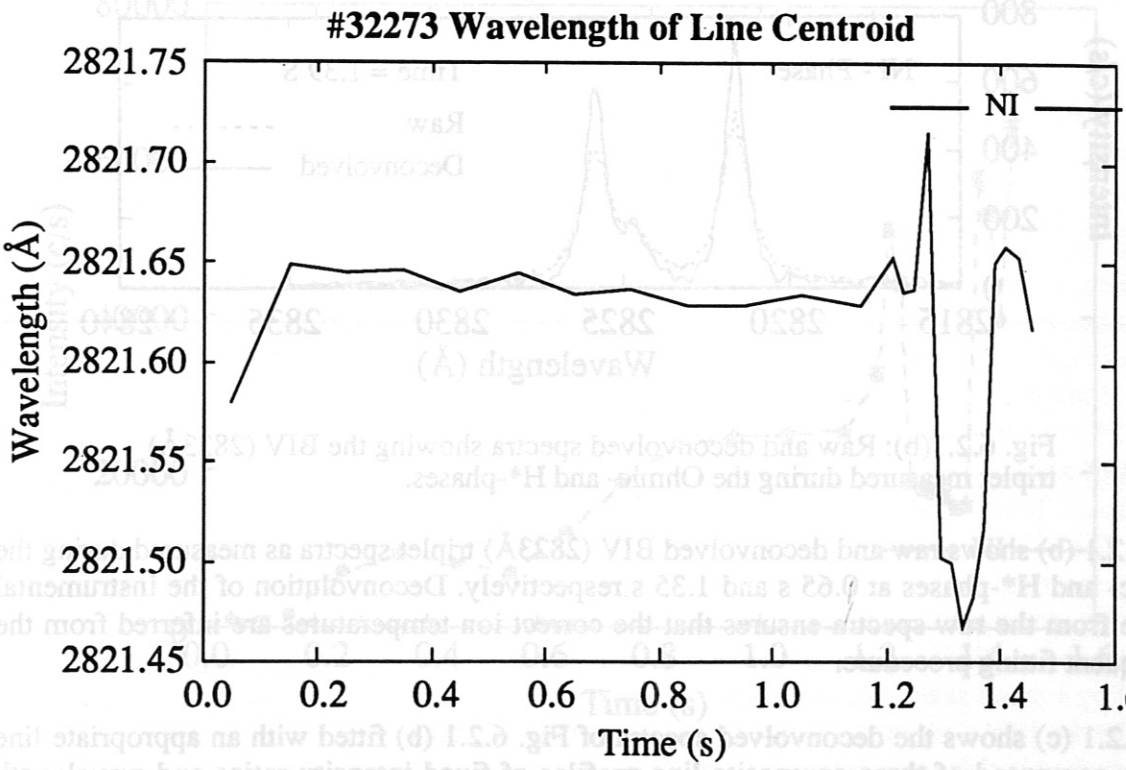

Fig. 6.2.1(a): The wavelength of the centroid of the most prominent BIV(2823Å) triplet line at 2821.68 Å.

In this case a significant 'blue' shift of the line is observed which increases slowly during the H*-phase. The maximum magnitude of the shift of the centroid wavelength relative to the Ohmic-phase value is about 0.2Å corresponding to values of the perpendicular drift velocity of approximately 20 kms^{-1}. The fact that the centroid wavelength of the raw spectrum exhibits such noticable shifts during the H*-phase is an important confirmation of the reliability of the more complex deconvolution and line fitting procedure used to evaluate most of our data. This is particularly important as, when viewing along a single line of sight through regions where the drift velocity component along the line of sight changes, representation of the line profile Gaussians may not be strictly valid. That the shift of the centroid wavelength of the line and the centroid wavelength of the fitted profile are almost equal is an important check that the line fitting method can provide us with valid line shift measurements. (In Chap.2, Equ. 2.14 has been used to evaluate the perpendicular drift velocity, $v_{i\perp m}$*, inferred from the shift of the line *centroid wavelength* which would be observed viewing perpendicular to $\vec{B}$ for various values of E_r , $v_{\parallel}$ etc, as shown in Figs. 2.2 (b - e).)

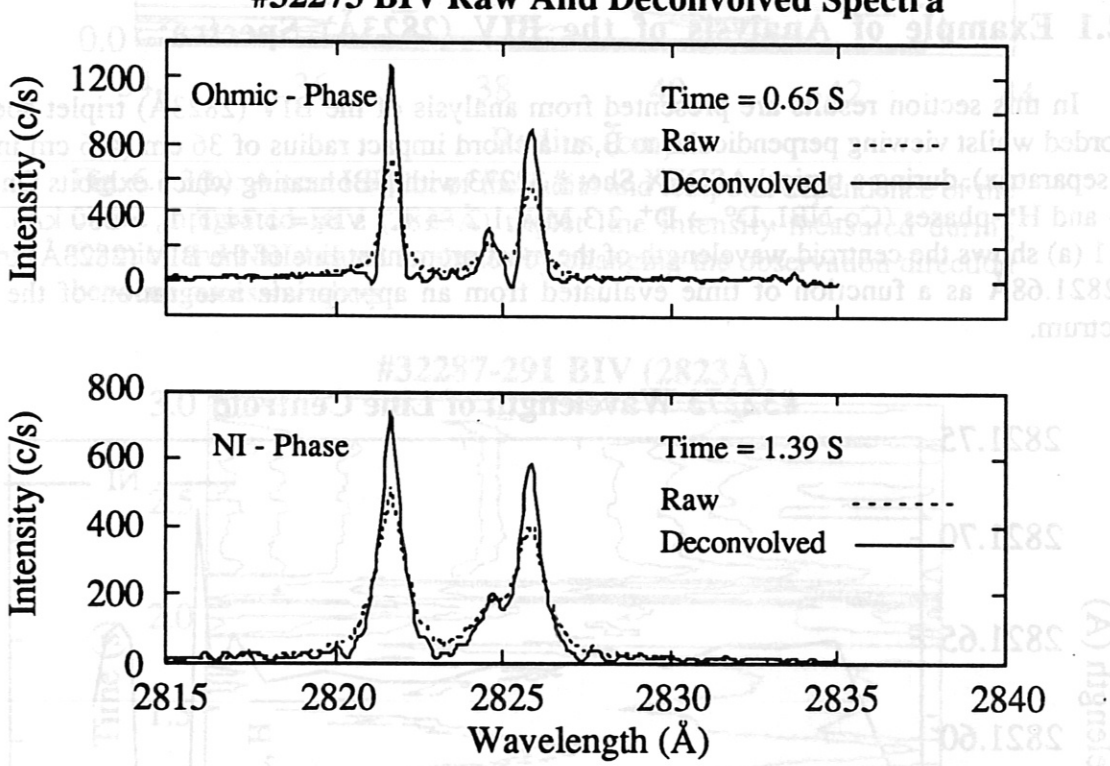

Fig. 6.2.1(b): Raw and deconvolved spectra showing the BIV (2823Å) triplet measured during the Ohmic- and H*-phases.

Fig. 6.2.1 (b) shows raw and deconvolved BIV (2823Å) triplet spectra as measured during the Ohmic- and H*-phases at 0.65 s and 1.35 s respectively. Deconvolution of the instrumental profile from the raw spectra ensures that the correct ion temperatures are inferred from the subsequent fitting procedure.

Fig. 6.2.1 (c) shows the deconvolved spectra of Fig. 6.2.1 (b) fitted with an appropriate line profile composed of three composite line profiles of fixed intensity ratios and wavelength separations and of equal widths.

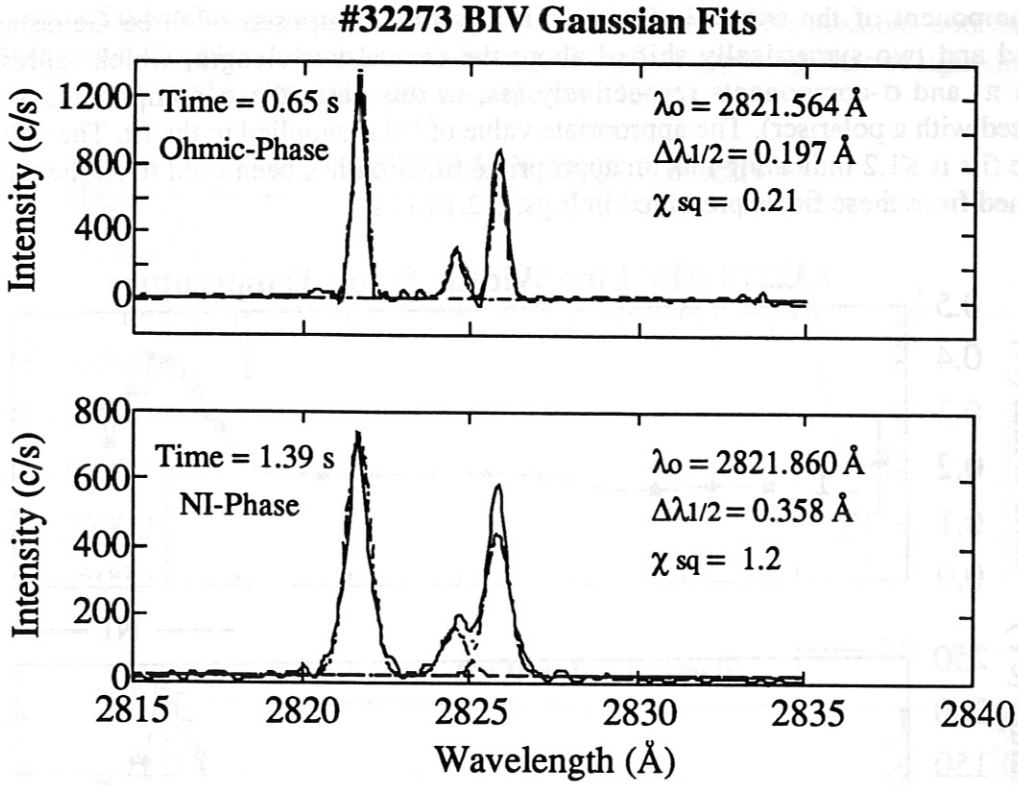

Fig. 6.2.1(c): The deconvolved BIV (2823Å) triplet lines (as measured during the Ohmic- and H*-phases) fitted with an appropriate line profile.

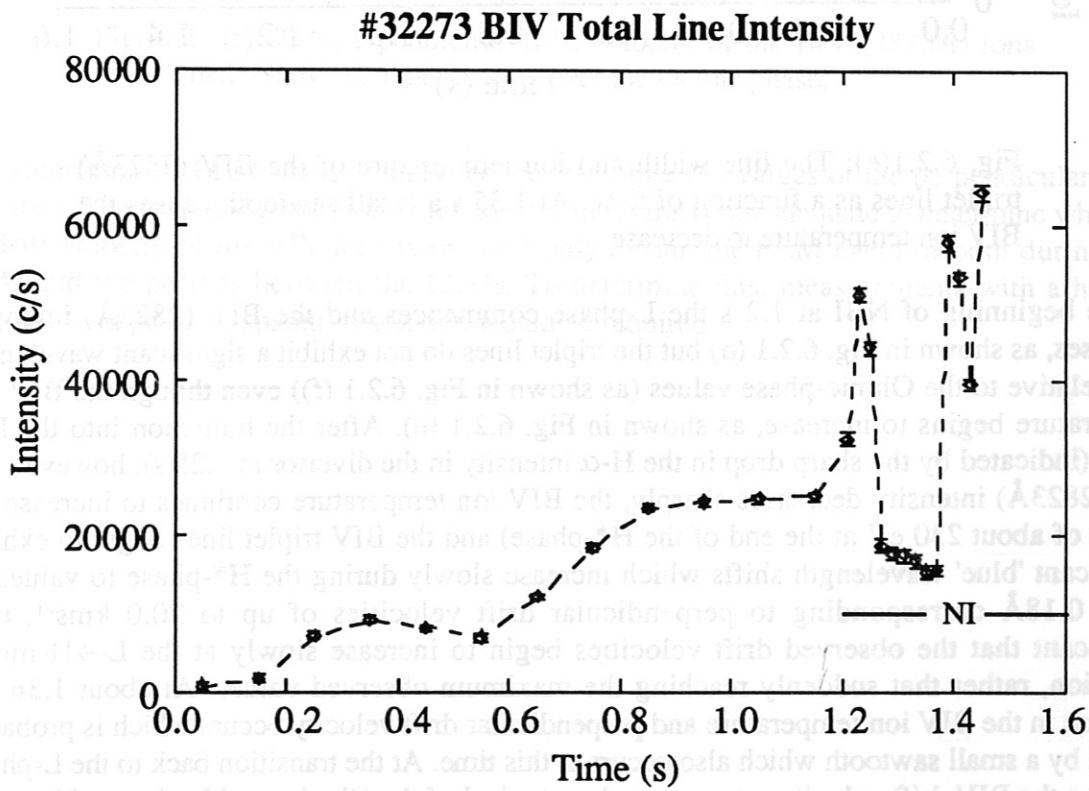

Fig. 6.2.1(d): The total line intensity of the BIV (λ=2823 Å) line. L-phase: 1.2-1.25 s and from 1.38 s onward. H* -phase: 1.25-1.38 s.

Each component of the triplet is fitted with a profile composed of three Gaussians, one unshifted and two symetrically shifted about the central wavelength, which represent the Zeeman π- and σ-components respectively (as, in this case, the σ-components were not suppressed with a polariser). The appropriate value of |B| is supplied to the fit. The value of χ^2 for these fits is ≤ 1.2 indicating that an appropriate function has been used to fit the data. Data determined from these fits is presented in Figs. 6.2.1 (d - f).

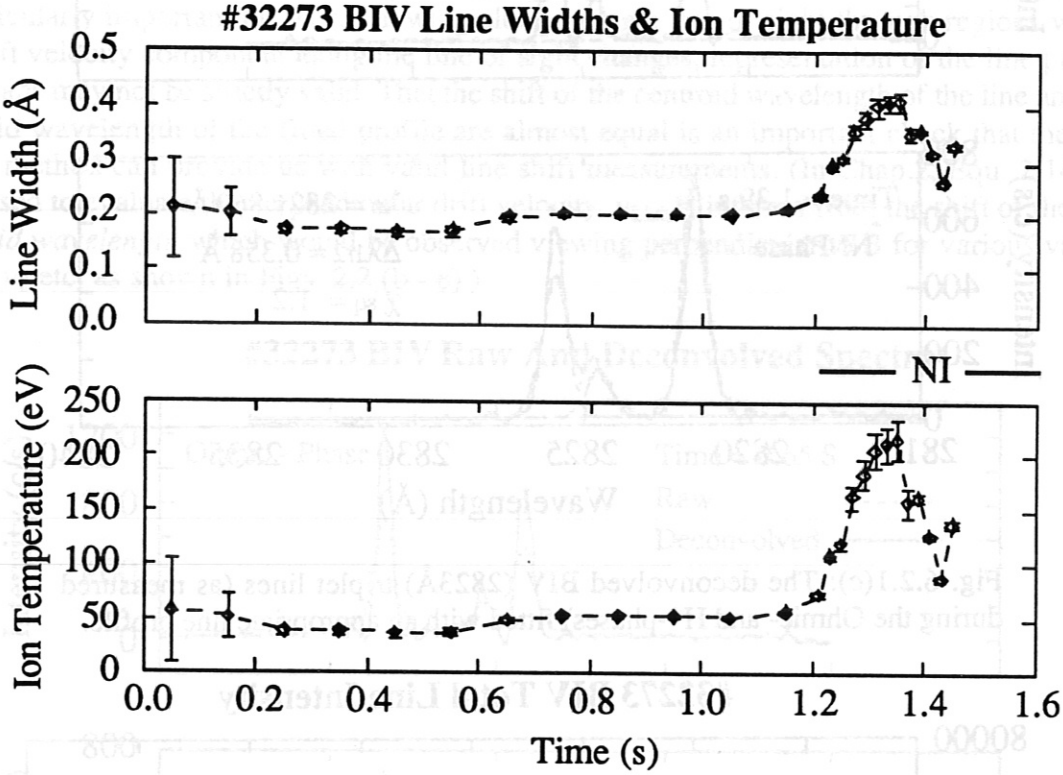

Fig. 6.2.1(e): The line width and ion temperature of the BIV (2823Å) triplet lines as a function of time. At 1.35 s a small sawtooth causes the BIV ion temperature to decrease.

At the beginning of NBI at 1.2 s the L-phase commences and the BIV (2823Å) intensity increases, as shown in Fig. 6.2.1 (d) but the triplet lines do not exhibit a significant wavelength shift relative to the Ohmic-phase values (as shown in Fig. 6.2.1 (f)) even though the BIV ion temperature begins to increase, as shown in Fig. 6.2.1 (e). After the transition into the H*-phase (indicated by the sharp drop in the H-α intensity in the divertor at 1.25 s), however, the BIV (2823Å) intensity decreases sharply, the BIV ion temperature continues to increase (to values of about 230 eV at the end of the H*-phase) and the BIV triplet lines begin to exhibit significant 'blue' wavelength shifts which increase slowly during the H*-phase to values of about 0.18Å corresponding to perpendicular drift velocities of up to 20.0 kms^{-1}. It is significant that the observed drift velocities begin to increase slowly at the L$\rightarrow$H-mode transition, rather that suddenly reaching the maximum observed values. At about 1.36 s a decrease in the BIV ion temperature and perpendicular drift velocity occurs which is probably caused by a small sawtooth which also occurs at this time. At the transition back to the L-phase at 1.38 s the BIV drift velocity returns to values typical of the Ohmic- and L-phases. Note that these drift velocities are determined relative to a mean value over the Ohmic-phase. With a system which views along one line of sight it is difficult to determine the absolute wavelength accurately enough to determine absolute drift velocities of less than about 2.0 kms^{-1} as are typical of the perpendicular drift velocities present during the Ohmic-phase. For the

construction of the velocity vector diagrams presented below, where possible, a measurement of the differential Doppler shift observed viewing along two opposing lines of sight during two successive shots is used to determine the absolute velocities.

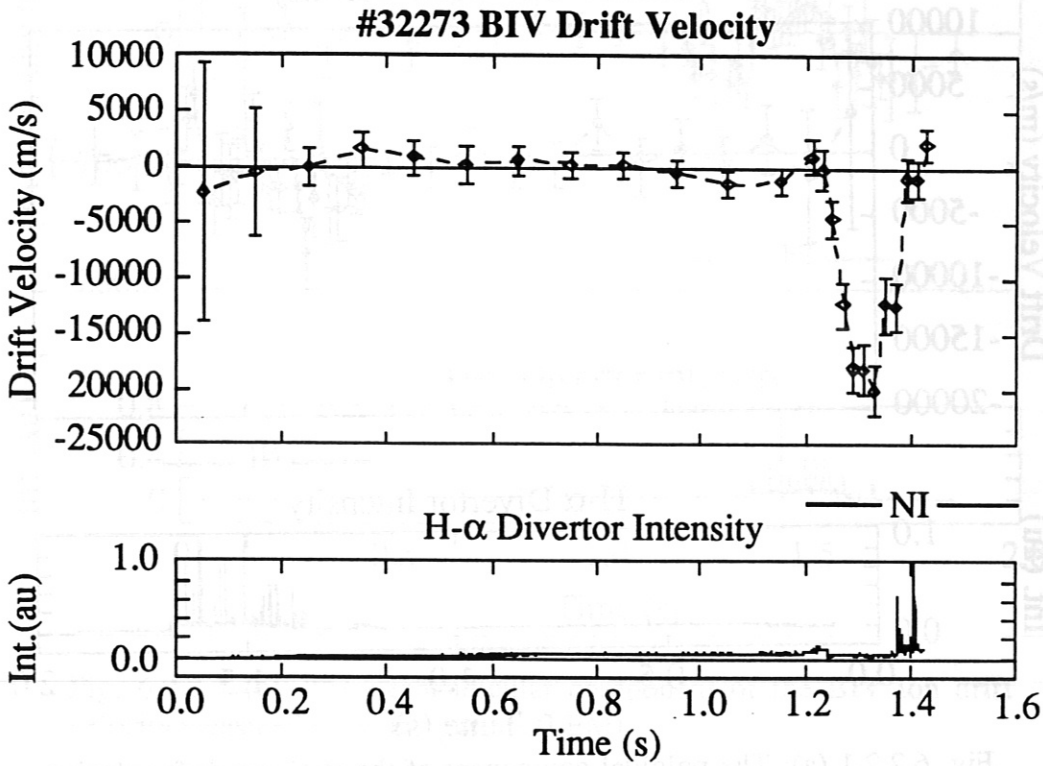

Fig. 6.2.1(f): The perpendicular drift velocity of the BIV (2823Å) ions determined relative to a mean value over the Ohmic phase.

The occurrence of ELMs substantially reduces the observed values of the perpendicular drift velocities. The temporal resolution of our system of 20 ms is not adequate to determine whether the drift velocity of the BIV ions is reduced only during the ELM event or both during the ELMs and the periods between the ELMs. To determine this, measurements with a higher temporal (and possible spatial) resolution would be required.

6.2.2 Measurements of Poloidal, Toroidal and Perpendicular Drift Velocities:

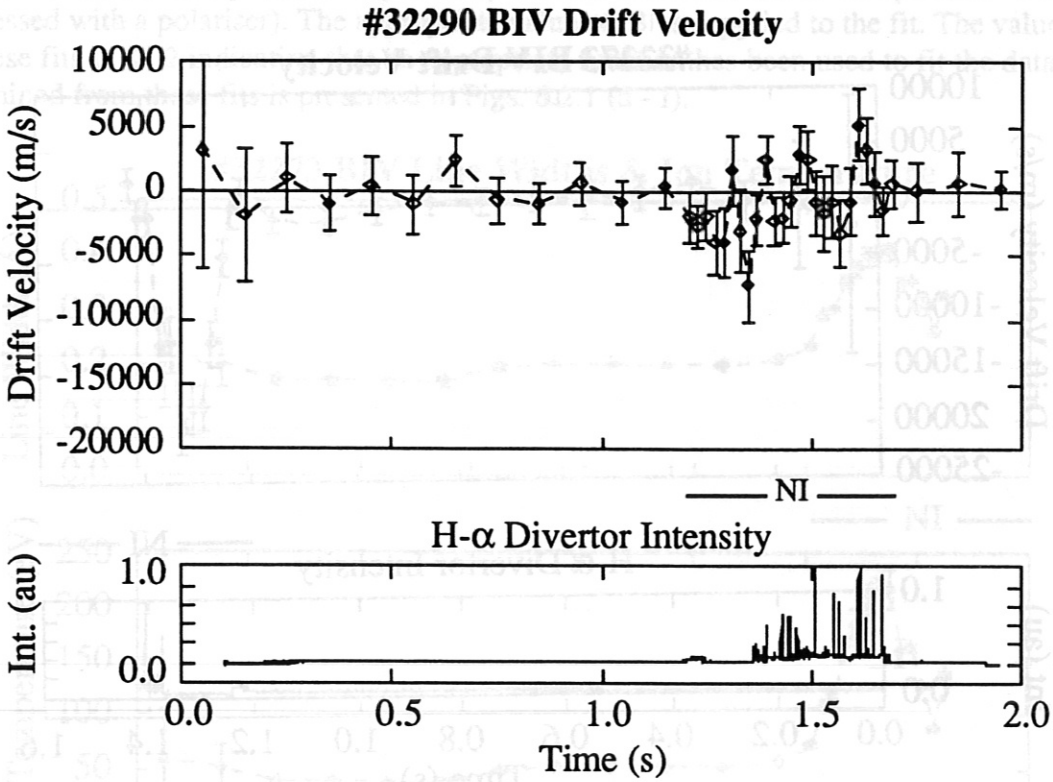

Fig. 6.2.2.1 (a): The poloidal component of the BIV ion drift velocity measured viewing upwards (LEM).

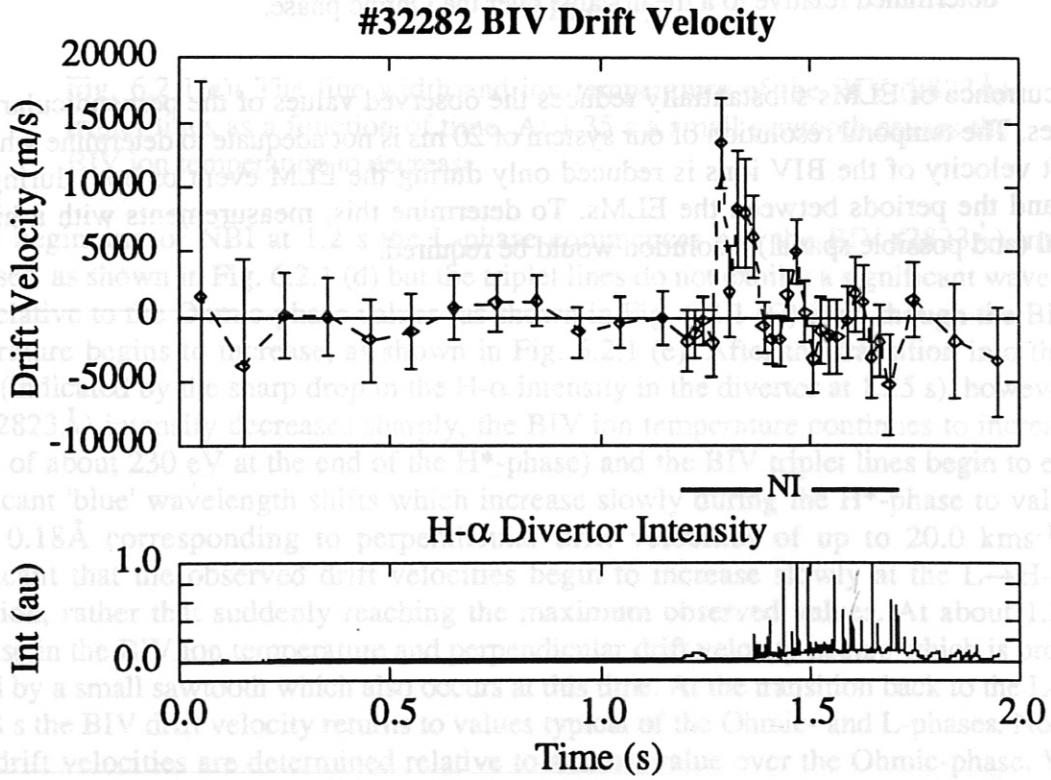

Fig. 6.2.2.1 (b): The poloidal component of the BIV ion drift velocity measured viewing downwards (UEM).

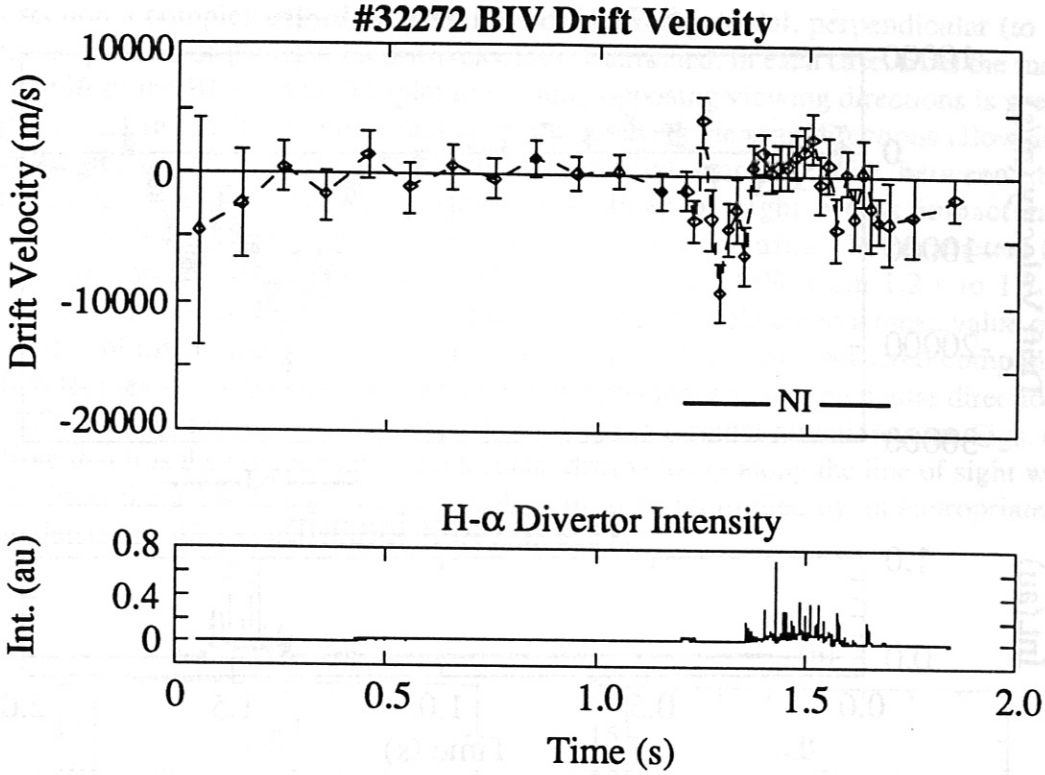

Fig. 6.2.2.1 (c): The perpendicular component of the BIV ion drift velocity measured viewing upwards (LEM).

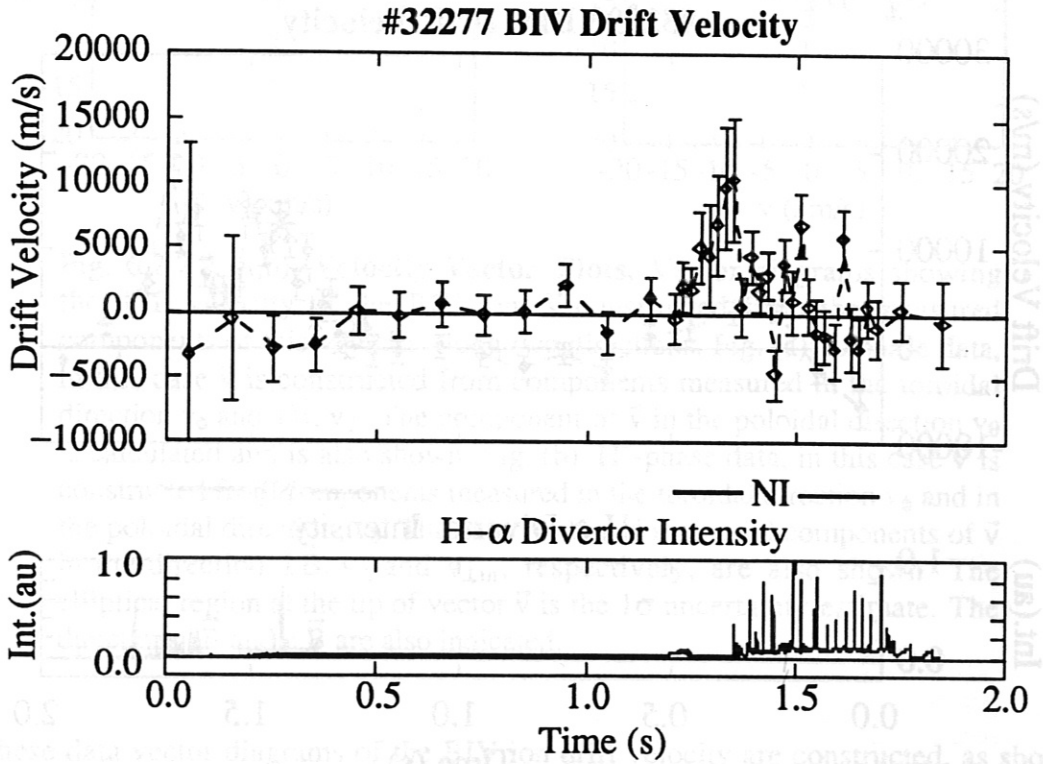

Fig. 6.2.2.1 (d): The perpendicular component of the BIV ion drift velocity measured viewing downwards (UEM).

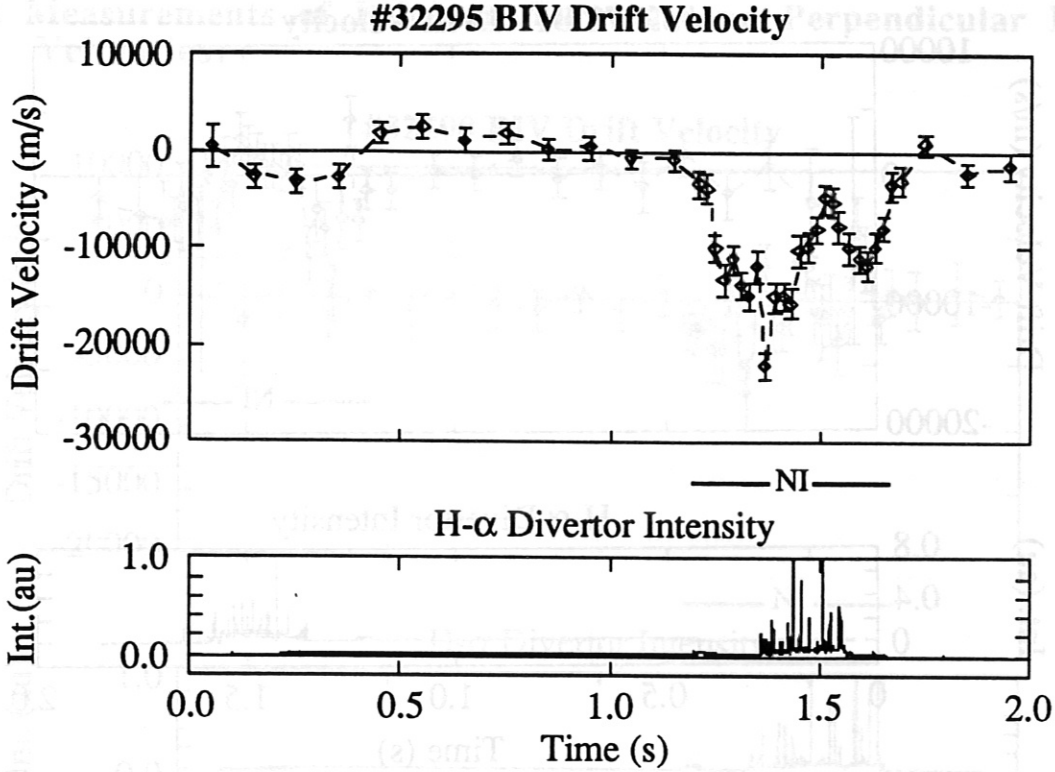

Fig. 6.2.2.1 (e): The toroidal component of the BIV ion drift velocity measured viewing parallel to I_p.

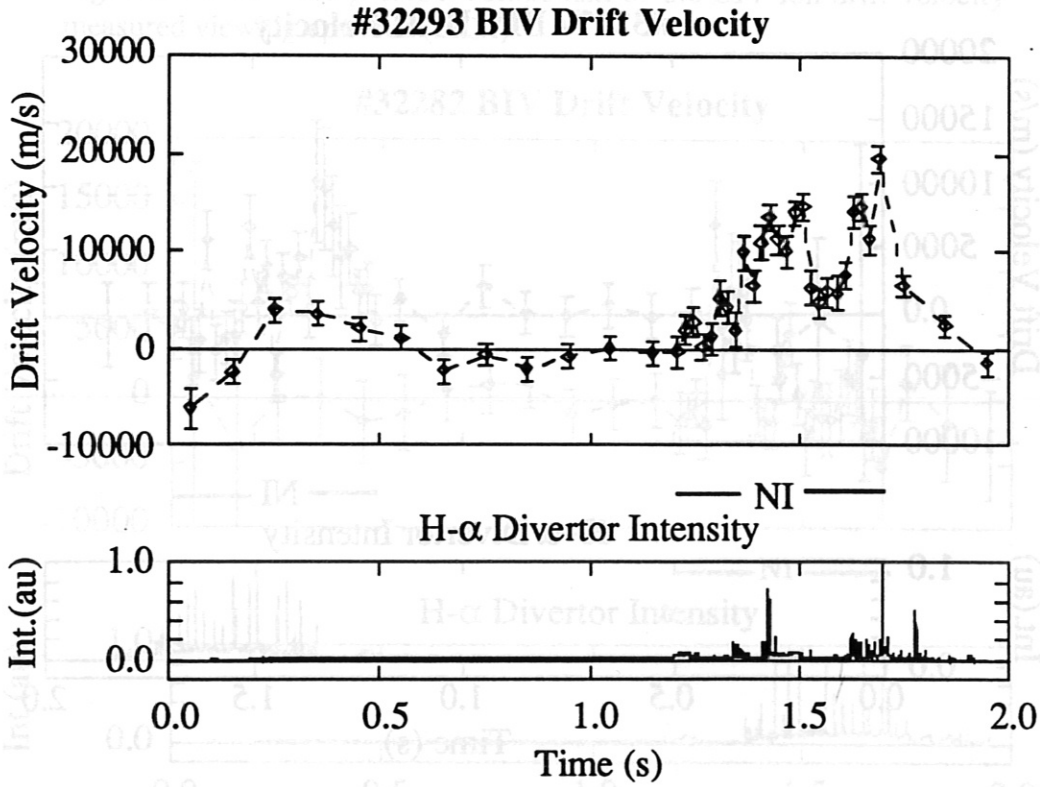

Fig. 6.2.2.1 (f): The toroidal component of the BIV ion drift velocity measured viewing anti-parallel to I_p.

In this section a complete set of the time histories of the poloidal, perpendicular (to $\vec{B}$) and toroidal components of the BIV ion drift velocities determined, in each case, from the measured Doppler shift of the BIV (2823Å) triplet lines along opposing viewing directions is presented, see Figs. 6.2.2.1 (a - f). These observations along opposing viewing directions allow absolute drift velocities to be estimated from the differential Doppler shift between the two measurements. The poloidal and perpendicular lines of sight are at impact radii of approximately 38 cm (i.e. about 4 cm to 6 cm inside the separatrix). The parameters for this series of shots are: I_p = 280 kA, B_t = 1.74 T, Co-NBI, 2.3 MW from 1.2 s to 1.7 s. The values of the drift velocities shown in these time histories are relative to a mean value over the Ohmic-phase of the plasma. In the H*-phases the magnitudes of the measured components of the drift velocities are between 0 and 10 kms^{-1} in the poloidal and perpendicular directions (see Figs. 6.2.2.1 (a - d)) and between 10 and 20 kms^{-1} in the toroidal directions (see Figs. 6.2.2.1 (e,f)). Note that it is the component of the toroidal drift velocity along the line of sight which is shown in Figs. 6.2.2.1 (e,f) and that these values must be multiplied by an appropriate factor (~1.2) to determine the toroidal drift velocity component.

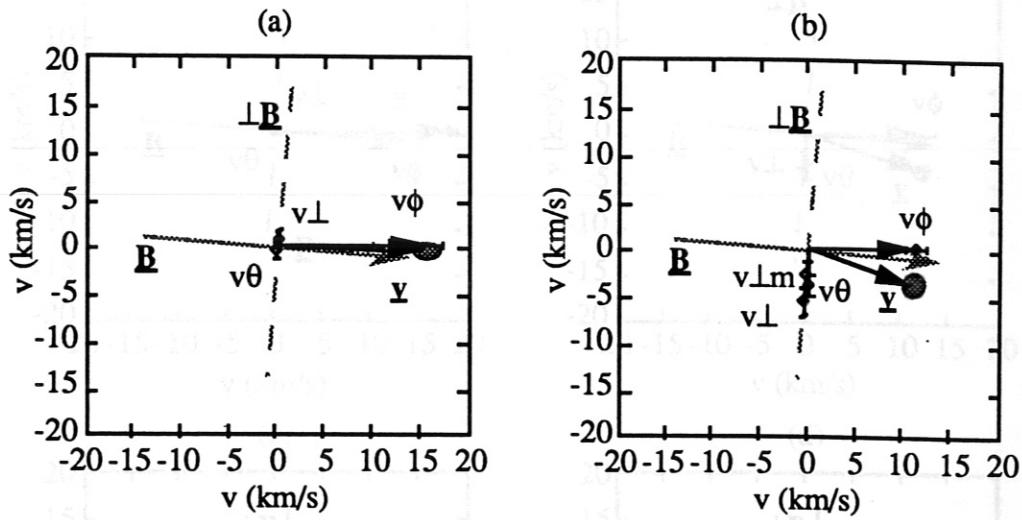

Fig. 6.2.2.2 (a,b): **Velocity-Vector Plots.** Vector diagrams showing the drift velocity of the BIV ions $\vec{v}$ constructed from the measured components of this velocity along two directions. Fig. (a): L-phase data, in this case $\vec{v}$ is constructed from components measured in the toroidal direction v_ϕ and $\perp\vec{B}$, $v_\perp$. The component of $\vec{v}$ in the poloidal direction v_θ is calculated and is also shown. Fig. (b): H*-phase data, in this case $\vec{v}$ is constructed from components measured in the toroidal direction v_ϕ and in the poloidal direction, v_θ. The calculated and measured components of $\vec{v}$ in the direction $\perp\vec{B}$, $v_\perp$ and $v_{\perp m}$, respectively, are also shown. The elliptical region at the tip of vector $\vec{v}$ is the 1σ uncertainty estimate. The directions $\parallel\vec{B}$ and $\perp\vec{B}$ are also indicated.

From these data vector diagrams of the BIV ion drift velocity are constructed, as shown in Figs. 6.2.2.2 (a,b). The velocities used to construct these vectors are absolute values calculated from the differential Doppler shift measured along opposing directions during successive similar shots. In the H*-phase the magnitude of the poloidal component of the drift velocity is comparable to that of the toroidal component and $v_\perp$ is in the $-\vec{B}\times\nabla p$ direction (electron diamagnetic drift direction). Also shown in these diagrams are the directions perpendicular and

parallel to $\vec{B}$. In the H*-mode $\vec{v}$ lies at a significant angle to $\vec{B}$. This value of $v_\perp$ implies that there is a negative radial electric field (inwardly directed) at the plasma periphery, just inside the separatrix. In the L-phase $v_\perp$ is small and in the $\vec{B}x\nabla p$ direction, this case $\vec{v}$ is almost exactly in the toroidal direction. This implies that the magnitude of the radial electric field is much reduced in the L-phase compared to it's magnitude the H*-phase. Note that, when the values of v_θ and $v_\perp$ are small (≤ 2 kms^{-1}), the contributions to the measured velocities from the diamagnetic drift and the gradient of the excitation probability become significant and thus, in this case, it is not possible to determine whether the sign of E_r is reversed in the L-phase compared to that in the Ohmic-phase.

6.2.3 Parameter Dependencies of the Drift Velocities:

In this section the dependencies of the BIV ion drift velocity on the NBI-heating power, the confinement regime (L-, H- and H*-mode), the direction of the NBI with respect to the plasma current (Co- and Counter-NBI) and the magnitude of B_t and I_p (at constant q_a) are presented.

6.2.3.1 NBI-Power Dependence: L-, H- and H*-phases:

In order to study the dependence of the BIV ion drift velocity on the NBI-heating power measurements have been made on a series of shots with 1.0 MW (3 sources), 1.6 MW (5 sources) and 2.3 MW (7 sources) of NBI. For these shots I_p = 280 kA and B_t = 1.74 T corresponding to q_a = 3. Vector diagrams showing the measured BIV ion drift velocity are shown in Figs. 6.2.3.1 (a - d).

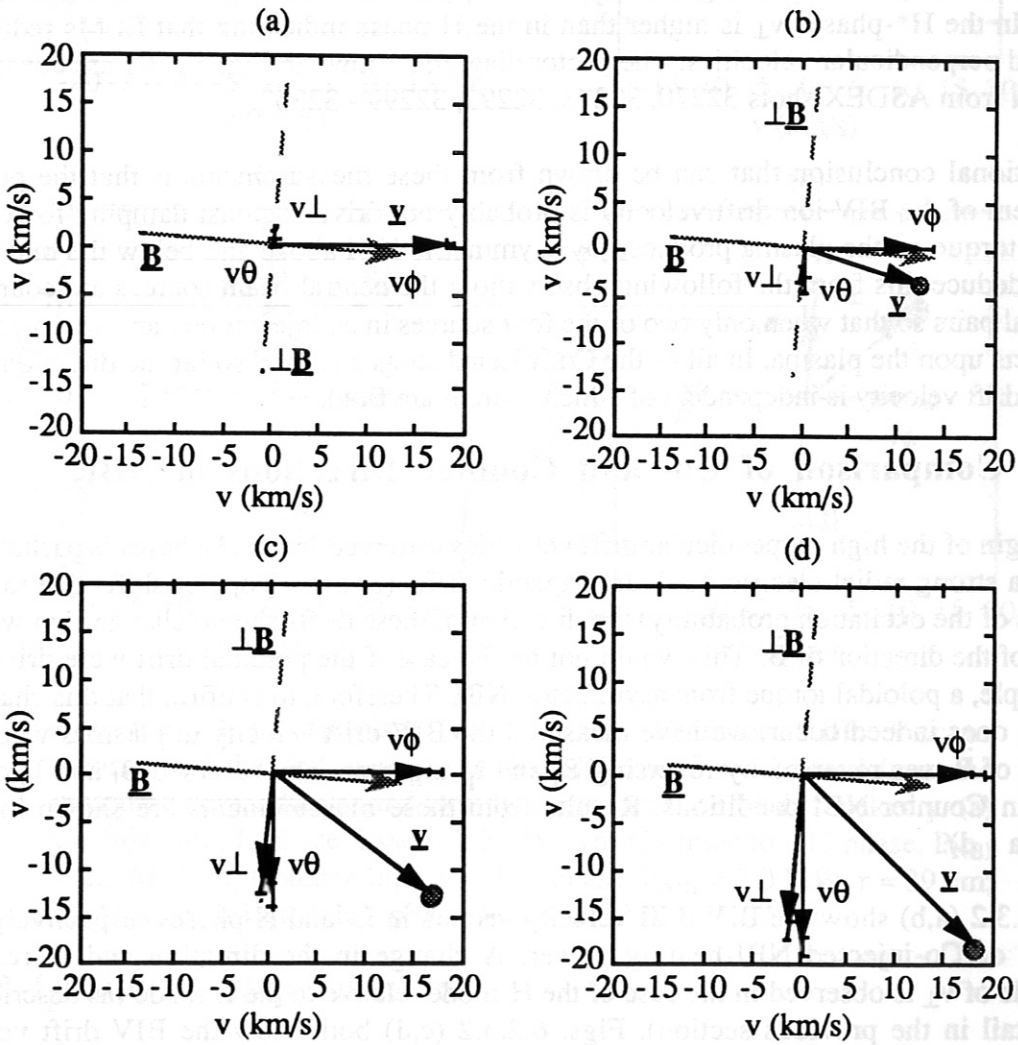

Fig. 6.2.3.1 NBI Power Dependence: Vector diagrams showing the drift velocity vector $\vec{v}$ constructed from the toroidal component v_ϕ and perpendicular component $v_\perp$ of the measured drift velocity of the BIV ions. These data are from a NBI power scan with: (a) 1.0 MW (L-phase); (b) 1.6 MW (H-phase); (c) 1.6 MW (H*- phase); and (d) 2.3 MW (H*-phase) of Co-Injected NBI heating. For these shots I_p = 280 kA and B_t = 1.74 T. The directions ∥ and ⊥ to $\vec{B}$ are also indicated.

With 1.0 MW of NBI no transition into the H-mode occurs and the plasmas remain in the L-mode where the perpendicular drift velocity $v_\perp$ is measured to be in the $\vec{B}x\nabla p$ direction (ion diamagnetic drift direction) and is much smaller than the toroidal component of the drift velocity v_ϕ, as shown in Fig. 6.2.3.1 (a). With 1.6 MW of NBI the plasmas undergo transitions into both ELMy H-mode and ELM-free H*-mode phases. In the ELMy H-phase $v_\perp$ is still small compared with v_ϕ but in the opposite direction to that measured in the L-phase, as shown in Fig. 6.2.3.1 (b). In contrast, in the H*-phase the perpendicular component of the drift velocity $v_\perp$ is much higher than in the L- and 'grassy' H-phases, being comparable in magnitude to the toroidal component v_ϕ, as is shown in Fig. 6.2.3.1 (c). With 2.3 MW of NBI v_θ and v_ϕ are almost equal at around 18 kms^{-1}. These measurements show that in the L-mode the perpendicular drift velocity of the BIV ions is in the $\vec{B}x\nabla p$ direction (ion diamagnetic drift direction) and is small (≤ 2 kms^{-1}). In the H- and H*-modes the direction of $v_\perp$ changes to the $-\vec{B}x\nabla p$ direction (electron diamagnetic drift direction) and is much larger in magnitude (5 to 15 kms^{-1}). In the H*-phases $v_\perp$ is higher than in the H-phase indicating that ELMs reduce the measured perpendicular velocities. The vector diagrams shown in Fig. 6.2.3.1 are constructed with data from ASDEX shots 32270, 32273, 32292, 32299 - 32302.

An additional conclusion that can be drawn from these measurements is that the poloidal component of the BIV ion drift velocity is probably not driven against damping forces by a poloidal torque on the plasma produced by asymmetric NBI above and below the mid-plane. We can deduce this from the following observation: the neutral beam sources are coupled in horizontal pairs so that when only two of the four sources in an injector box are fired a poloidal torque acts upon the plasma. In all of the Co-injected shots analysed so far the direction of the poloidal drift velocity is independent of which sources are fired.

6.2.3.2 Comparison of Co- and Counter Directions of NBI:

If the origin of the high perpendicular drift velocities observed in the H-phases is particle ExB drifts in a strong radial electric field, diamagnetic drifts (or even Doppler shifts due to radial gradients of the excitation probability) the direction of these drifts should change sign with the reversal of the direction of $\vec{B}$. This would not be the case if the poloidal drift were driven by, for example, a poloidal torque from asymmetric NBI. Therefore, to confirm that this change in direction does indeed occur, we have measured the BIV drift velocity in plasmas where the direction of $\vec{B}$ was reversed by reversing B_t and I_p together. The reversed B_t and I_p case is studied in Counter-NBI conditions. Results from these measurements are shown in Figs. 6.2.3.2 (a - d).

Figs. 6.2.3.2 (a,b) show the BIV drift velocity vectors in L- and H-phases respectively with 2.3 MW of Co-injected NBI-heating power. A change in the direction and increase in magnitude of $v_\perp$ is observed in the case of the H-mode relative to the L-mode (as described in more detail in the previous section). Figs. 6.2.3.2 (c,d) both show the BIV drift velocity vectors in H*-phases with 2.0 MW of Counter-injected NBI-heating power measured along chords with impact radii of 39 cm and 37 cm respectively. It is clear that on reversing the direction of $\vec{B}$ the direction of $v_\perp$ also reverses as is expected for the case where the perpendicular drift velocities are due to the ExB or diamagnetic-like drifts mentioned above (alternatively one can say that the direction of $v_\perp$ retains a constant relation to the ion or electron diamagnetic drift directions). These results show that the poloidal component of the BIV ion drift velocity is not driven by a poloidal torque from the NBI acting on the plasma. If this were the case the poloidal drift velocity would not change sign on reversal of the direction of $\vec{B}$. The

velocity vectors shown in Figs. 6.2.3.2 (a,b) (Co-NBI case) were constructed from data measured on ASDEX Shots 32272, 32277, 32293, 32295 and in Figs. 6.2.3.2 (c,d) (Ctr-NBI case) from ASDEX Shots 31918 - 31923.

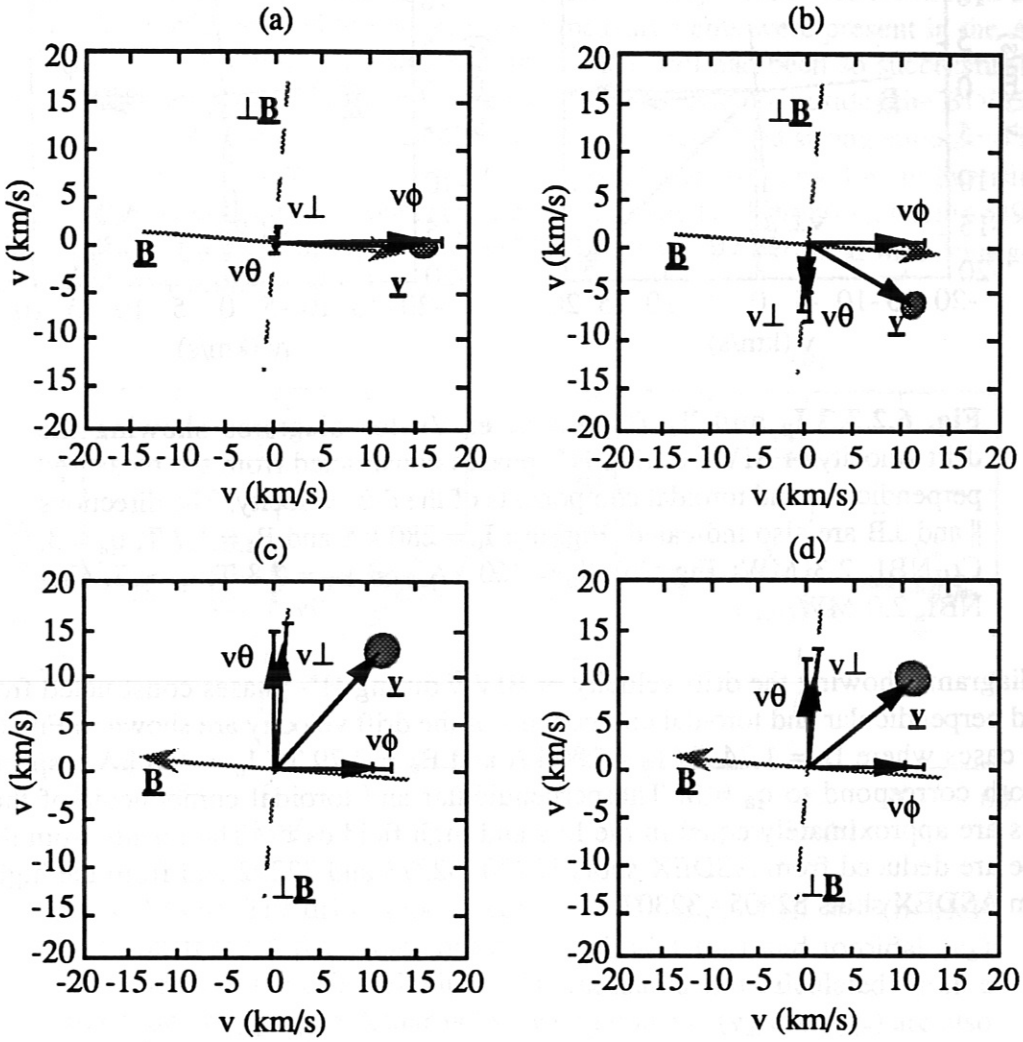

Fig. 6.2.3.2 Comparison of Co- and Counter NBI: Vector diagrams of the drift velocity of the BIV ions $\vec{v}$ constructed from the measured perpendicular and toroidal components of the drift velocity. (a) Co-Injection, L-phase, P_{NBI} = 2.3 MW; (b) Co-Injection, H-phase, P_{NBI} = 2.3 MW; (c) Counter-Injection, H*- phase, P_{NBI} = 2.0 MW, r = 39 cm; (d) Counter-Injected, H*- phase, P_{NBI} = 2.0 MW, r = 37 cm.

6.2.3.3 I_p and B_t Dependence:

In order to study the dependence of the BIV ion drift velocity on B_t under conditions of constant q_a (and also so that the line of sight remains aligned $\perp\vec{B}$ when measuring $v_\perp$) the plasma current I_p was changed together with the toroidal magnetic field B_t.

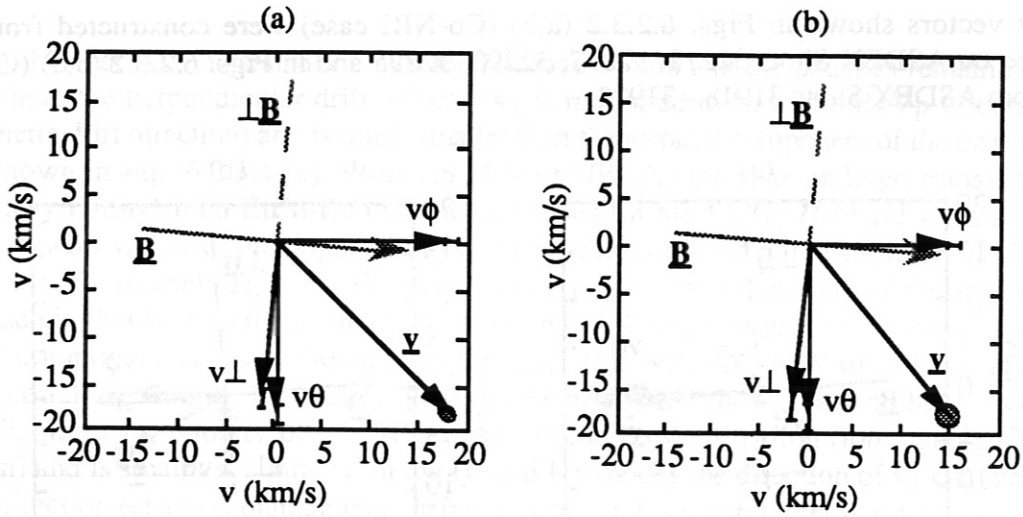

Fig. 6.2.3.3 I_p and B_ϕ Dependence: Vector diagrams showing the drift velocity of BIV $\vec{v}$ during H*- phases constructed from the measured perpendicular and toroidal components of the drift velocity. The directions $\parallel$ and $\perp\vec{B}$ are also indicated. Fig. (a): I_p = 280 kA and B_t = 1.7 T, q_a = 3, Co-NBI, 2.3 MW; Fig. (b): I_p = 460 kA and B_t = 2.8 T, q_a = 3, Ctr-NBI, 2.0 MW.

Vector diagrams showing the drift velocity of BIV $\vec{v}$ during H*- phases constructed from the measured perpendicular and toroidal components of the drift velocity are shown in Fig. 6.2.3.3 (a,b) for cases where B_t = 1.74 T / I_ϕ = 280 kA and B_ϕ = 2.79 T / I_p = 460 kA respectively, which both correspond to q_a = 3. The perpendicular and toroidal components of the drift velocities are approximately equal in the low and high field cases. The results from the low field case are deduced from ASDEX shots 32270, 32273 and 32292 and from the high field case from ASDEX shots 32305 - 32307.

6.3 Results from Different Ion Species:

The principle of our measurement of the radial electric field requires that different ionic species have to be used to measure E_r at different radii. However, only a restricted number of intrinsic impurity ions that could be used to perform these measurements were present in the ASDEX plasma. This was because the boronisation of the vessel wall had been so successful that the influxes of oxygen and carbon had been drastically reduced and so, besides the BIV (2823Å) triplet lines, only the very strong CIII (4549Å) triplet lines remained strong enough to be used for our measurements. The CV (2274Å) and OV (2784Å) lines were too low in intensity to be utilised. We therefore concentrated our measurements on the HeII (4686Å), CIII (4649Å) and BIV (2823Å) lines. The measurements on the He II ions were performed in discharges with mixed D^+ and He^{++} working gas.

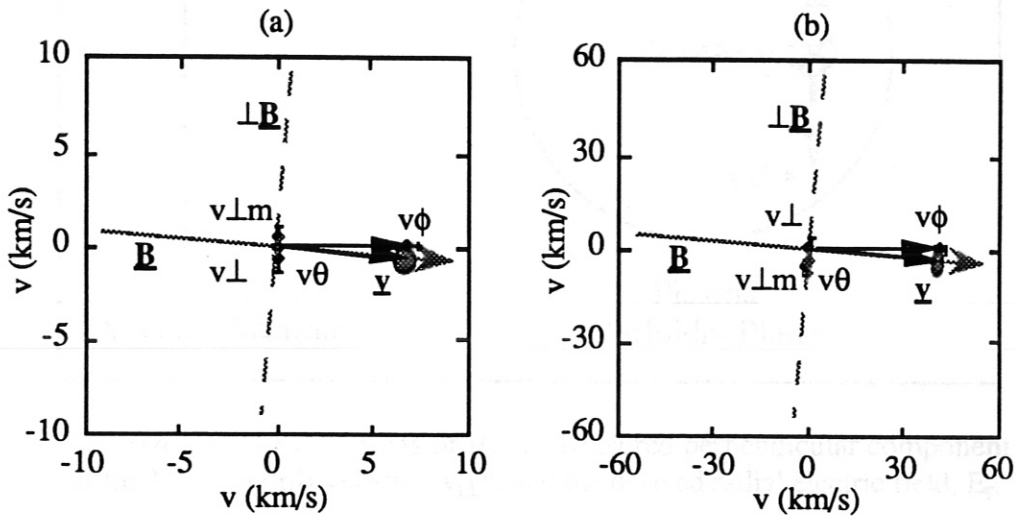

Fig. 6.3 (a,b): The drift velocity vectors $\vec{v}$ of (a) the CIII and (b) HeII ions constructed from the measured poloidal (v_θ) and toroidal (v_ϕ) components of the drift velocities. The measured and calculated (from a projection of $\vec{v}$) perpendicular velocity components ($v_\perp$ and $v_{\perp m}$) are also shown, as are the directions $\perp$ and $\parallel$ to $\vec{B}$. (Note the different scales in each case.) These data are from H-phase plasmas with Co-NBI, 2.5 MW, $H^o \rightarrow (D^+ + He^{++})$ measuring at a chord impact radius of 39 cm.

The results from the analysis of all of the CIII (4649Å) spectra evaluated show that the perpendicular drift velocities of the C III ions are small (≤ 2.0 kms^{-1}) under all conditions (L-, H- and H*-modes). It is shown in Sect. 6.1 that the CIII ions are located at or just outside the separatrix radius. This result, therefore, indicates that the strong negative radial electric field ($|E_r| \leq -25$ kVm^{-1}), which we infer is present a few cm inside the separatrix during the H*-mode (from the measured perpendicular drift velocity of the BIV ions), is not present at or just outside the separatrix under any conditions ($|E_r| \leq 4$ kVm^{-1}).

An example of the drift velocity vector of the CIII ions constructed from measurements made during the H*-phase is shown in Fig. 6.3 (a). In this case the CIII ions drift almost exactly along $\vec{B}$. Our measurements on the HeII (4686Å) line show a significant perpendicular drift velocities of about 8 kms^{-1} (in the electron diamagnetic drift direction) during the H*-phase (and also during the ELMy H-phase). The measured value of the toroidal component of the HeII ion drift velocity is considerably higher than the values measured for the BIV and the CIII ions. An example of the drift velocity vector of the HeII ions constructed from measurements

made during the H*-phase is shown in Fig. 6.3 (b). In this case the HeII ions also drift almost exactly along $\vec{B}$. The data used to construct Fig. 6.3 were measured during ASDEX Shots 31713, 722, 729 and 733.

As discussed in Chap. 3, the interpretation of the profile of the HeII (4686Å) line in terms of drift velocities is not straight forward. Particularly, the effect of changes in the relative contributions of electron impact and charge exchange excitation of this line between the Ohmic, L- and H-phases is not yet understood. Because of these problems we have concentrated our attention on the results of our measurements on the B IV ions.

6.4 Evaluation of the Radial Electric Field:

The aim of this work was to measure the radial electric field at the edge of ASDEX plasmas under a variety of conditions, particularly with reference to possible changes in E_r between L- and H-mode conditions. The principle of this measurement is explained in Chap. 2.

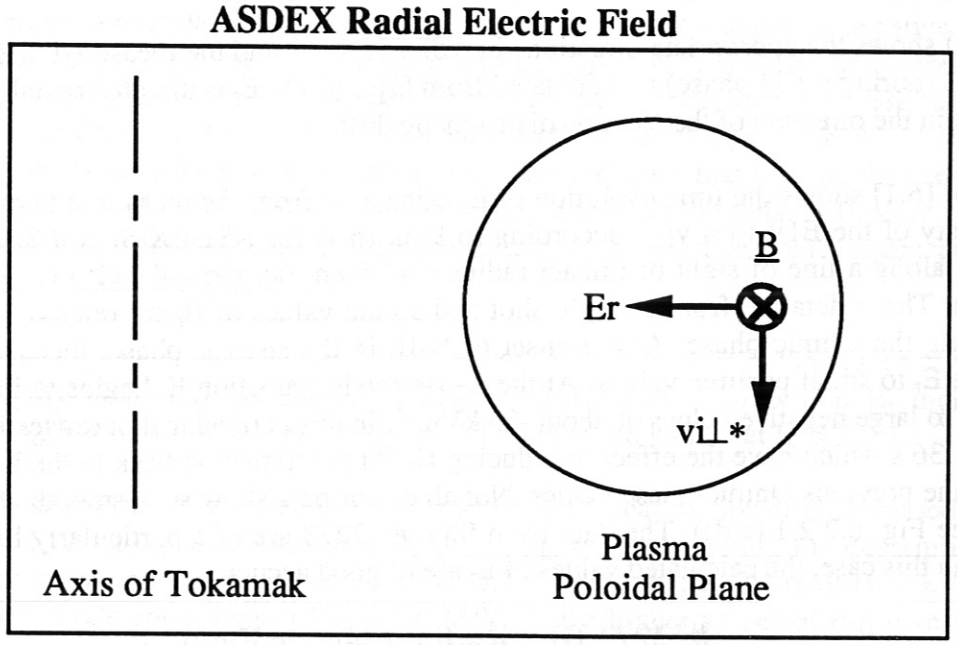

Fig. 6.4 (a): The directions of $\vec{B}$, the measured perpendicular component of the BIV ion drift velocity, $v_{i\perp}$*, and the derived radial electric field, E_r.

From a local measurement of the Doppler shift of the centroid wavelength of a spectral line a measured velocity $v_{i\perp}$* may be inferred. In general this is related to the local value of E_r by Equ. (2.7) and, in the limiting cases of $\omega_i\tau_k << 1$ and $\omega_i\tau_k >> 1$, E_r is given by Eqns. (2.8) and (2.10), respectively. Generally, therefore, in order to determine E_r from $v_{i\perp}$* we have to account for possible contributions to the shift from the ion diamagnetic drift and the radial gradient of the excitation probability ζ'_k. When performing such a measurement using passive emission spectroscopy the measured line emission is an integral of the emission from along the line of sight. Numerical calculations of this line-of-sight integration (presented in Chap. 2) show that for such edge emission shells there is a line of sight with a particular impact radius along which the shifts due to p'_i and ζ'_k are negligible. Additionally, by tilting the line of sight out of the poloidal plane into a direction $\perp \vec{B}$, any contribution to the shift from a component of the ion drift velocity parallel to $\vec{B}$ can be minimised. When measuring along such a line of sight E_r can be inferred directly from the measured shift from the expression:

$$E_r = v^*_{i\perp} B \qquad (6.1)$$

Note that E_r can be inferred directly from $v_{i\perp}$* without having to measure an orthogonal component. In Chap. 2 the radial emissivity profile of the BIV(2823Å) line, as measured in the H*-mode, is used to perform the line-of-sight integrations discussed above for model cases. The results of these calculations are presented in Fig. 2.2. The local values of the perpendicular ion fluid velocity $v_{i\perp}$ and the velocity determined from the measured line shift $v_{i\perp}$* are shown as a function of radius. It can be concluded from these results that, from a measurement of $v_{i\perp}$* E_r can be calculated directly from Equ. (6.1) when measuring along chords with impact radii

between 35 cm and 40 cm to an accuracy of ± 1.0 kVm^{-1}, even in the presence of drifts parallel to $\vec{B}$ of 100 kms^{-1}. The appropriate, approximate value of B to be used in Equ. (6.1) is that at the major radial position of the viewing chord R_c, which is given by:

$$B(R_c) = B(R_o)\frac{R_o}{R_c} \qquad (6.2)$$

Fig. 6.4 (a) shows the appropriate directions in ASDEX for $\vec{B}$ and the measured drift velocity $v_{i\perp}$* and E_r (during the H-phase) as calculated from Equ. (6.1). E_r is directed radially inwards and $v_{i\perp}$* is in the direction of the electron diamagnetic drift.

Fig. 6.4 (b) [6.1] shows the time evolution of E_r calculated from the measured perpendicular drift velocity of the BIV ions $v_{i\perp}$* according to Equ. (6.1) for ASDEX Shot # 32273 when measuring along a line of sight of impact radius r = 36 cm (at about 4.5±1.5 cm inside the separatrix). These data are from a single shot and so the values of E_r are relative to a mean value during the Ohmic phase. At the onset of NBI, in the short L-phase, there is a slight increase in E_r to small positive values. At the L→H-mode transition E_r begins to increase in magnitude to large negative values of about -25 kVm^{-1}. In this particular shot sawteeth occur at 1.3 s and 1.36 s which have the effect of reducing E_r. At the transition back to the L-phase E_r returns to the previous Ohmic-phase values. Not all of our data show such smooth changes of E_r (e.g. see Fig. 6.2.2.1 (c,d)). The data from Shot # 32273 are of a particularly high count rate, thus, in this case, the calculated values of E_r are of good accuracy.

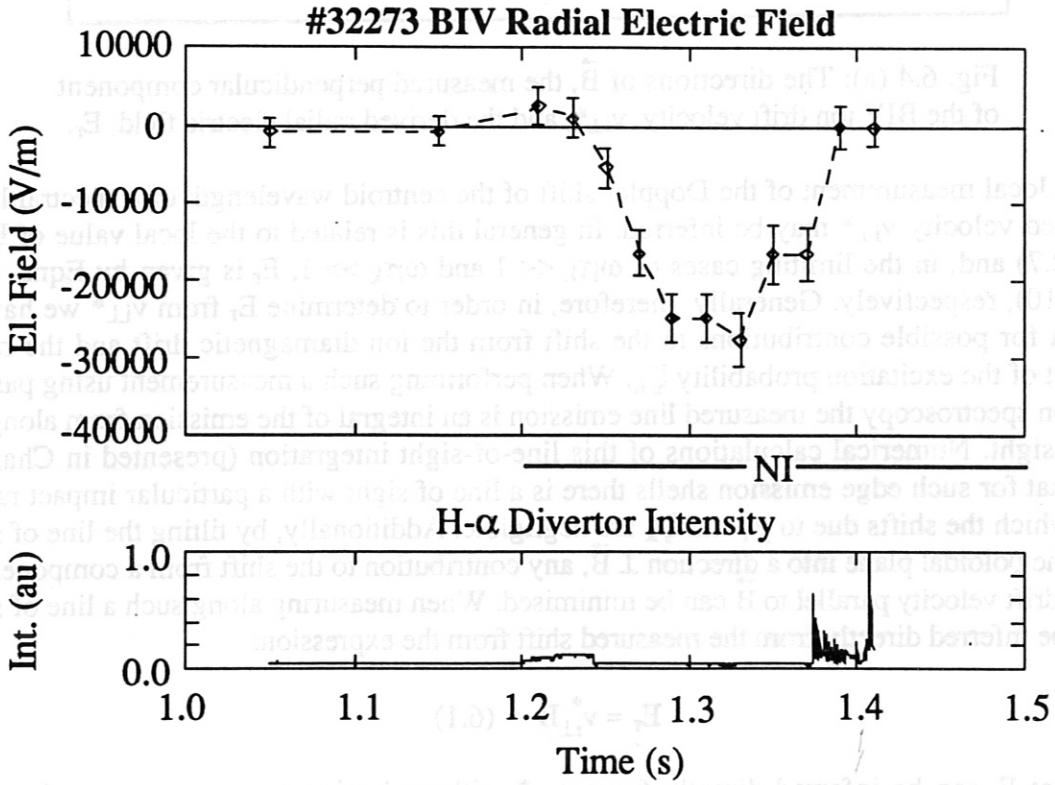

Fig. 6.4 (b) The radial electric field, E_r, calculated from the measured perpendicular drift velocity of the B IV ions, $v_{i\perp}$*.

Additional information, obtained from our measurements on the BIV ions, on the parametric dependence of $v_{i\perp}$* on the toroidal field B_t, plasma current I_p and NBI heating power P_{NI} (presented in section 6.2.3) can be extended to make statements on the dependence of E_r on these parameters.

Reversal of the sign of B_t and I_p (at constant magnitude and $q_a = 3$) reverses the direction of the observed perpendicular drift velocity and, hence, we can infer that E_r is negative (inwardly directed) in both co- and counter- NBI conditions. This can be seen in the vector diagrams presented in Figs. 6.2.3.2 (b,c). Note that, although in the counter-injection case the injection power is lower ($P_{NI} = 2.0$ MW) than in the co-injection case ($P_{NI} = 2.3$ MW), the measured value of $v_\perp$ is about twice that in the latter case. This indicates that E_r is likely to be larger in counter-injection conditions than in co-injection conditions for the same NBI heating power. It is well known that there is a marked improvement in the particle confinement in counter- compared to co-injection conditions.

On increasing B_t and I_p together so that q_a remains constant ($q_a = 3$) the values of $v_\perp$ and v_ϕ remain largely unaltered (as shown in Fig. 6.2.3.3). This implies that E_r increases on increasing B_t, from $E_r = -22$ kVm^{-1} at $B_t = 1.7$ T to $E_r = -36$ kVm^{-1} at $B_t = 2.8$ T.

Fig. 6.2.3.1 shows the drift velocity vectors as the NBI heating power is increased from 1.0 MW to 2.3 MW at constant values of B_t and I_p ($q_a = 3$). Following the description of the dependence of $v_\perp$ on P_{NI} given in Sect. 6.2.3.1 we find that E_r is small (< 2 kVm^{-1}) and positive in L-mode conditions at $P_{NI} = 1.0$ MW. At the higher values of P_{NI} investigated E_r changes sign to negative values which increase in magnitude with P_{NI}. At $P_{NI} = 1.6$ MW in the H-phase (with ELMs) E_r increases in magnitude to -4 kVm^{-1} and at the same heating power but in the H*-phase (ELM-free) E_r increases in magnitude to -16 kVm^{-1}. Increasing P_{NI} further to 2.3 MW increases E_r in magnitude to -23 kVm^{-1} in the H*-phase. Note that in the H-phases with ELMs the values of $v_\perp$ (and E_r) are average values over periods with many ELM-events.

6.5 Discussion of Results:

It is not our aim in this report to discuss the likely validity of the various recently proposed theories of how changes in a radial electric field and / or a poloidal rotation of the plasma may be related to the confinement improvement which occurs at the L→H-mode transition. It is, rather, to describe the principle of our measurement of these quantities and to present the results of our measurements with their associated uncertainties. With our main purpose being fulfilled in earlier sections, here we discuss the results in terms of simpler hypotheses based upon established theoretical results.

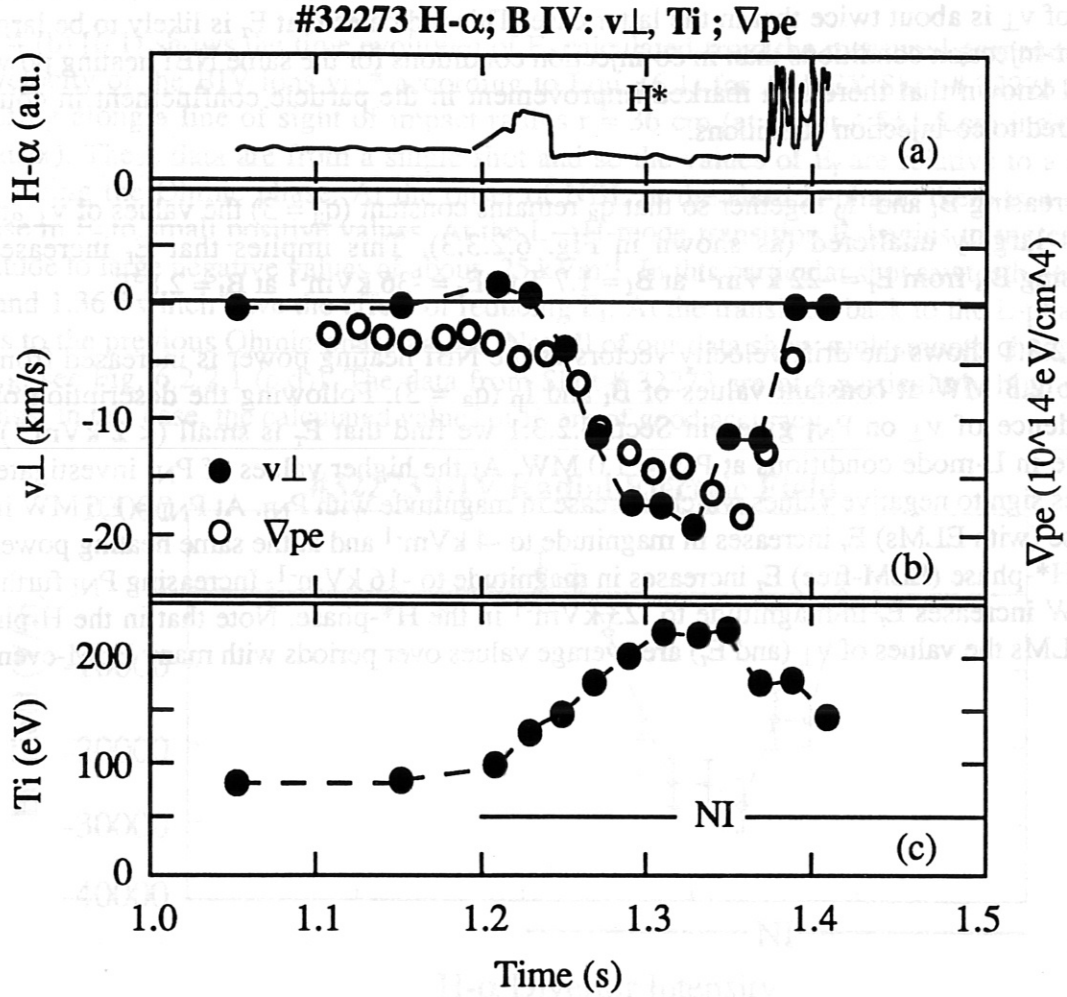

Fig. 6.5, The time evolution of the measured perpendicular drift velocity of the BIV ions, $v_\perp$; the ion temperature of the BIV ions determined from Doppler broadening T_i ; the edge pressure gradient of the electrons ∇p_e determined from Thomson scattering data; and the divertor Hα intensity.

Fig. 6.5 shows the time evolution of the measured perpendicular drift velocity of the BIV ions $v_\perp$; the ion temperature of the BIV ions determined from Doppler broadening T_i ; the edge pressure gradient of the electrons ∇p_e determined from Thomson scattering data; and the divertor Hα intensity for ASDEX Shot # 32273. It can be seen that the measured perpendicular drift velocity of the BIV ions $v_\perp$ (and hence E_r) increases slowly during the H*-phase with a very similar temporal behaviour to both ∇p_e and T_i (BIV). The occurrence of sawteeth at 1.3 s and 1.36 s reduce both T_i (BIV) and $v_\perp$. That these quantities evolve in a similar manner is evidence that $v_\perp$ (and E_r) may be related to the pressure or temperature gradients at the edge.

The steady-state radial force balance for each particle species is given by Equ. (2.3). Each species is confined separately by the combined Lorenz force due to the radial electric field and the $v_\perp B$ force arising from any component of the fluid velocity perpendicular to $\vec{B}$. Each particle species may be considered in a frame of reference moving $\perp$ to $\vec{B}$ at the local E_r/B drift velocity. In such a reference frame there exists no net radial electric field and the species is confined by the jxB force due it's diamagnetic current. In the absence of viscous forces or inter-species frictional forces opposing these perpendicular flows, the pressure profiles of all the particle species will be independent of one another. The perpendicular drift velocity profile of each species is able to adjust to the appropriate value to provide confinement and the radial profile of E_r is arbitrary. Considering a pure deuterium plasma, if poloidal flow of the deuterons v_θ is heavily damped, in the extreme case where $v_\theta = 0$ the radial electric field is given by:

$$E_r = \frac{1}{n_D e}\frac{\partial p_D}{\partial r} - v_\phi B_\theta \quad (6.3)$$

where the D-subscript refers to the deuterons. It follows that, for the case where v_θ is zero and the $v_\phi B_\theta$ term is negligible, E_r is uniquely determined by the deuteron pressure gradient, i.e. when the deuterons are unable to flow perpendicularly to $\vec{B}$ the deuterons must be confined by an appropriate radial electric field.

There is strong theoretical reason to believe that any poloidal component of the bulk ion fluid velocity would be heavily damped. Poloidal rotation of the ion fluid would result in deformation of a fluid volume element due to the changing magnitude of the toroidal field with the major radial position of the volume element. This deformation produces a force on the fluid, due to parallel ion viscosity, which opposes the poloidal rotation. This process is referred to as 'magnetic pumping' [6.4, 6.5]. As seen above, the ambiguity of whether the deuterons are confined by electrostatic or $v_\perp B$ forces is removed if such viscous damping processes reduce the poloidal component of the ion fluid velocity to negligible values. The radial electric field is then given by $E_r = p_i'/n_i e$ (neglecting the small contribution from any toroidal motion, $-v_\phi B_\theta$). Estimating this value of E_r for ASDEX Shot # 32273 by assuming p_i' and n_i are equal to the values of p_e' and n_e measured using the YAG Thomson scattering diagnostic gives a value of E_r of not more than 30% of that inferred from the Doppler shift of the BIV ions. We may conclude from this that the measured value of E_r is at least sufficient to confine the deuterons (in the case that the poloidal component of their motion is zero).

Where one particle species is prevented from rotating poloidally E_r is uniquely defined by the pressure gradient of that species. Should an additional ion species be present which experiences negligible damping so that its perpendicular drift velocity can adopt any value, then it's pressure profile need not be related to that of the non-rotating species. If, however, the perpendicular drift velocity of the second species is also reduced to negligible values by viscous forces or inter-species frictional forces then the pressure profile of this species will be related to that of the first (as is the case for the neo-classical impurity accumulation phenomenon). Considering the deuterons and a second ion species of charge Ze the pressure profiles are related according to:

$$\frac{1}{n_z}\frac{\partial p_z}{\partial r} = \frac{Z}{n_D}\frac{\partial p_D}{\partial r} \quad (6.4)$$

which leads to 'accumulation' profiles related by:

$$n_z \alpha n_D^Z T_D^{Z-1} \quad (6.5)$$

We have, therefore, the following possible cases: a) independent perpendicular ion fluid velocities allowing independent ion pressure profiles; b) equal perpendicular ion fluid velocities where the ion pressure profiles must be related by Equ. (6.5); and / or c) the poloidal drift velocity component of one or more species being negligibly small, due to viscous damping, which leads to a unique radial profile of E_r given by the pressure profile(s) of the damped species.

The parallel ion viscosity coefficient of the electrons is smaller than that of the ions by a factor $(m_e/m_i)^{1/2}$ [6.6] so that any poloidal component of the electron drift velocity would be much less heavily damped than would be the case for the ions. The electrons are thus able to assume an independent pressure profile from that of the ions. The pressure profiles of the low ionisation states of the low-Z impurity species (on which we perform our measurements), which have the form of narrow shells at the edge of the plasma, are obviously not related to the pressure profile of the deuterons by a relation of the form of Equ. (6.4). Thus, these ions must be free to adopt a largely independent perpendicular fluid velocity, otherwise their pressure profiles would not be stationary. If the ionisation time of these ions τ_{ion} is shorter than the viscous damping time, which is of the order of the ion-ion collision time τ_{ii}, the ions may experience little effective viscous damping before being further ionised and thus be free to adopt independent pressure and perpendicular drift velocity profiles. Simultaneous, radially resolved measurements of all of the relevant quantities in Equ. (6.3) for a number of ion species should yield a unique value of E_r unless additional physics has been overlooked. Our present experimental arrangement is unable to perform such measurements.

The measured value of E_r is found to increase on increasing B_t and I_p (at constant P_{NI} and q_a) as is described in Sect. 6.4. If the deuterons are prevented from rotating poloidally and E_r adjusts to confine the ions, this result implies that ∇p_i should have also increased on increasing B_t.

Neoclassical theories predict a poloidal component of the ion fluid velocity in a pure plasma $v_{\theta,neo}$ which arises from a balance between thermal forces on the ions due to the ion temperature gradient and the viscous damping of the poloidal flow [6.2, 6.3]. The value of this neoclassical poloidal fluid velocity is given by:

$$v_{\theta,neo} = \frac{k}{eB} \frac{\partial T_i}{\partial r} \quad (6.6)$$

where k is a constant, the value of which is dependent upon the collisionality of the ions. The collisionality of the ions ν_{ii}^* is given by:

$$\nu_{ii}^* = \frac{\nu_{ii} R_o q}{v_{th,i} \varepsilon^{3/2}} \quad (6.7)$$

where ν_{ii} is the ion-ion collision frequency, $v_{th,i}$ is the ion thermal velocity and ε is the inverse aspect ratio, r/R_o. Where $\nu_{ii}^* << 1$ the ions are in the collisionless 'banana' regime and k = 1.17; where $1 << \nu_{ii}^* << \varepsilon^{-3/2}$ the ions are in the 'plateau' regime and k = -0.5; and where $\nu_{ii}^* >> \varepsilon^{-3/2}$ the ions are in the collisional 'Pfirsch-Schlüter' regime and k = -1.7 [6.3] or -2.2

[6.2]. Estimates of ν_{ii}^* (calculated from values of the edge density, temperature and Z_{eff} measured in ASDEX) give $\nu_{ii}^* > 10$ in the H*-mode, therefore the ions are in the collisional regime. Evaluating $v_{\theta,neo}$ by assuming $k = -1.7$, $T_i = T_e$ and using values of T_e measured about 5 cm inside the separatrix by the YAG Thomson scattering system gives $v_{\theta,neo} = 3.8$ kms^{-1} in the H*-phase of Shot # 32273. This value is about 20% of that measured for the BIV ions during the same shot (see Fig. 6.2.1(f)).

As we are unable to resolve the actual gradients of n_i and T_i at the edge we cannot conclude whether our measurements of $v_\perp$ (and E_r) are in agreement with the hypothesis of either a) the deuterons not rotating poloidally and being confined solely by the radial electric field, or b) the BIV ions rotating poloidally with the deuterons at a velocity equal to that predicted by neoclassical theory for the bulk plasma ions. (The value of the neoclassical poloidal ion fluid velocity calculated above is none the less much lower than that which we measure for the BIV ions.)

7. Conclusions:

The drift velocity vectors of the BIV, CIII, and HeII ions have been determined at the periphery of ASDEX Ohmic and L- and H-mode NBI heated plasmas from spectroscopic measurements of the Doppler shift of spectral line emission. These velocity vectors have been constructed from measured values of the poloidal drift velocity v_θ (or the drift velocity perpendicular to $\vec{B}$, $v_\perp$) and the toroidal drift velocity v_ϕ of the ions. Where possible, these velocities are determined from the differential Doppler shift of spectral line emission measured along opposing viewing chords on successive plasma shots.

The measurements on the BIV ions were most successful as the BIV(2823Å) line was of adequate intensity and with an intensity maximum just inside the separatrix radius (r = 40 cm). The intensities of the CIII (4647Å) and the HeII (4686Å) lines were also sufficient to perform measurements. In the case of HeII(4686Å), however, interpretation of the shift of the line centroid wavelength in terms of the drift velocity is complicated by the unresolved fine structure components, especially when measuring along a single chord. Under all plasma conditions investigated, the measured poloidal and perpendicular drift velocities of the CIII ions are small (< 2000 ms^{-1}) and show no marked changes at the L→H-mode transition. The CIII(4647Å) emissivity has a maximum just outside the separatrix (at r = 41 cm in the Ohmic phase).

Numerical calculations (based upon the measured emissivity profiles) show that, in the case of emission shells localised near the plasma edge, there is a viewing chord in a direction perpendicular to $\vec{B}$, with a particular impact radius, along which the contribution to the line shift from the diamagnetic drift of the ions is negligibly small and any contribution from a component of the drift velocity parallel to $\vec{B}$ is also minimised. Thus, along this line of sight, the measured perpendicular drift velocity $v_\perp$ is due solely to any E_rxB drift velocity of the ions. Therefore, at this radius E_r can be determined directly from the measured value of $v_\perp$.

It is shown that, when attempting to determine E_r, it can be necessary to account for a component of the Doppler shift of a spectral line which can arise solely from a radial gradient of the excitation probability. When observing (along a direction $\perp\vec{B}$ and $\vec{r}$) lines emitted from excited states with lifetimes τ_k of the order of or longer than the reciprocal gyro-frequency ω_i^{-1} (i.e. $\tau_k\omega_i \sim 1$ or $\tau_k\omega_i > 1$), the presence of a radial gradient in the excitation probability of the excited state ζ'_k will produce a shift of the centroid wavelength of the line. In such a case the velocity inferred from the line shift will include an additional component v_{pseudo}, due solely to this effect, in addition to any diamagnetic velocity component v_{diam}. At radii where there are steep gradients in n_e and / or T_e (in the case of electron impact excitation) or of n_o (in the case of charge-exchange excitation) this contribution must be accounted for when interpreting line shifts in terms of the perpendicular ion fluid velocity $v_\perp$ or E_r. In the limiting case of $\tau_k\omega_i >> 1$ the diamagnetic and pseudo drift velocities may be combined into a single term proportional to $(\varepsilon' T_i)/(\varepsilon T_i)$ (where ε is the emissivity and T_i the ion temperature). Again, in the case of radially localised emission shells, there is a line of sight along which the contribution to the line shift from this compound term can be negligible and E_r can be determined directly from the line shift.

In Ohmic and L-mode conditions the measured values of v_θ and $v_\perp$ are small (< 2000 ms^{-1}) and in the ion diamagnetic drift direction ($B\times\nabla p$) for all of the ion species observed. In the ELM-free H-phases (H*-phases) the measured values of v_θ and $v_\perp$ of the BIV ions increase to values of the order of 10 kms^{-1} in the electron diamagnetic drift direction ($-B\times\nabla p$).

These high values of $v_\perp$ (or v_θ) are measured at chord impact radii at which the contributions to the measured velocities from v_{pseudo} and / or v_{diam} are negligible. The observation of these high

values of $v_\perp$ implies the existence of a strong, inwardly directed radial electric field E_r of magnitude ≤ 25 kVm^{-1} in the H*-phases of the plasmas. This conclusion is supported by two further observations. Firstly, the sign of $v_\perp$ reverses when the direction of the magnetic field is reversed. This observation supports the conclusion that the measured perpendicular fluid velocity is due to the E_rxB drift of the BIV ions. Secondly, the sign of $v_\perp$ is observed to be independent of the sign of any poloidal torque due to unbalanced momentum input from the NBI which would result from the separate firing of top or bottom NBI sources which are grouped in horizontal pairs.

The following observations indicate that the origin of this radial electric field may be related to the edge pressure or temperature gradients. In the H*-phase $v_\perp$ is seen to rise gradually on the time-scale of the evolution of the pressure gradient of the electrons p_e' and the temperature of the BIV ions. The maximum observed values of $v_\perp$ (which are reached towards the end of the H*-phase) increase with NBI heating power P_{NI} (at constant q and B_t) and exhibit no strong dependence upon I_p or B_ϕ (at constant P_{NI}), as is also the case for the edge temperature and pressure gradients. At the occurrence of ELM's, which temporarily reduce these edge gradients, a strong decrease in $v_\perp$ is observed.

From our measurements it is not possible to obtain information on the gradient of E_r inside the separatrix. For this purpose either another suitable impurity species with a maximum emissivity at a different radius to that of the BIV ions would be required and/or simultaneous measurements of the line emissivity profile along many lines of sight with different impact radii. These radial measurements would have to be of sufficient resolution to perform the wavelength resolved Abel inversions which would be required to determine E_r as a function of radius. From our measurements of $v_\perp$ of the CIII ions, however, we can conclude that there must be steep gradients of $v_\perp$ (and E_r) close to the separatrix since these ions are located mostly outside the separatrix and, as mentioned above, values of $v_\perp$ observed for these ions are always small.

Neoclassical theory [6.2, 3] predicts a poloidal velocity for the bulk plasma ions $v_{\theta,\,neo}$ which arises from a balance between thermal forces on the ions and viscous damping of poloidal ion flow. Its value is given by $v_{\theta,\,neo} = - k\nabla T_i$ where k is a constant, the value of which depends upon the collisionality regime. An estimate of the collisionality of the deuterons of $\nu_i^* > 10$ (calculated from measured values of the edge temperature, density and Z_{eff} in ASDEX H-mode plasmas) indicate that the deuterons are in the collisional Pfirsch-Schlüter regime where $k = 1.7$ [6.3]. Assuming $\nabla T_i = \nabla T_e$ and using values of ∇T_e calculated from Thomson scattering data gives values of $v_{\theta,\,neo}$ which are ~20% of those measured for the BIV ions.

The measured values of E_r are greater than the values required to confine the deuterons under the assumption that they do not rotate poloidally (i.e. $E_r = \nabla p_i/n_i e - v_\phi B_\theta$). Estimating the deuteron pressure gradients (by assuming $\nabla p_i = \nabla p_e$ (Thomson scattering)) we find that the measured value of E_r is about three times that required to confine the deuterons.

Because of our uncertain knowledge of the profiles of T_i and n_i in the edge region we cannot rule out that our experimental findings are, in fact, in agreement, on the one hand, with the bulk plasma ions not rotating poloidally and being confined by the radial electric field and, on the other hand, with the neo-classical prediction of v_θ (although the neo-classical value of v_θ calculated from Thomson scattering data is very low).

Appendix 1: The Influence of Gradients in the Excitation Rate on Doppler Shifts in the Presence of a Magnetic Field:

In this appendix an expression is derived which relates the fluid velocity of an ion species, $v_{i\perp}$, to the velocity inferred from the Doppler shift of photons emitted by excited ions of state k, $v_{i\perp}$*, in the presence of a magnetic field, gradients in the ground state ion density n_g and temperature T_g and the probability of excitation of ions from the ground state g to the state k, ζ_k.

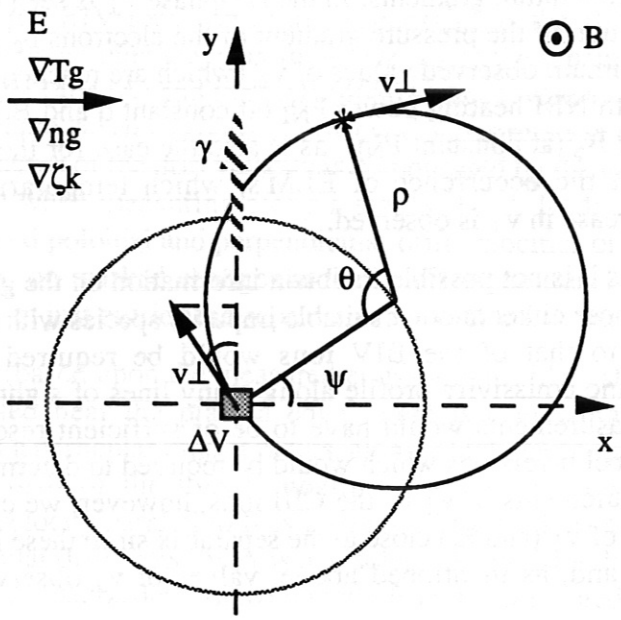

Fig. A1.1 Definition of the quantities considered in the analysis.

Fig. A1.1 defines the quantities considered in the analysis and their spatial relationships. The magnetic field $\vec{B}$ is aligned parallel to the z-axis, gradients in ng, Tg and ζk which are functions only of the x-coordinate are considered and, viewing in the negative y-direction, photons are observed which are emitted in the positive y-direction from an element of volume ΔV situated at the origin. In the presence of an electric field E aligned parallel to the x-axis, the guiding centres of the Larmor orbits will drift in the negative y-direction with a velocity $v_{ExB} = E/B$. To include this drift in the analysis we can consider the coordinate system, volume element and measurement system to be moving in the negative y-direction at the velocity v_{ExB}. The wavelength shift $\Delta\lambda_{ik}$ of the centroid of the line intensity emitted from transitions with a wavelength λ_{jk} from excited ions state k which decay to a state j within the volume element ΔV measured in the *laboratory* frame is given by:

$$\left[\frac{\Delta\lambda_{jk}}{\lambda_{jk}}\right]_{lab} = -\frac{1}{c}\left[\frac{\langle A_{jk}\, n_k\, v_y\rangle_{\Delta V}}{\langle A_{jk}\, n_k\rangle_{\Delta V}}\right]_{mov} + \left[\frac{E}{cB}\right]_{lab} \qquad (A1.1)$$

where A_{ik} is the transition probability for the excited ions of state k to decay to a state j, v_y is the component of the ion velocity along the direction of observation and the quantities labelled 'mov' and 'lab' are evaluated in the moving and laboratory coordinate systems respectively.

The velocity of the ions inferred from this shift (in a direction perpendicular to $\vec{B}$), $v_{i\perp}$*, in the *laboratory* frame is given by:

$$v^*_{g\perp} = c\left[\frac{\Delta\lambda_{jk}}{\lambda_{jk}}\right]_{lab} \qquad (A1.2)$$

Referring to Fig. A1.1, photons emitted from excited ions which decay within the volume element ΔV and which follow Larmor orbits with guiding centres located at all angles ψ on circles centred at the origin with radii equal to the Larmor radius ρ, such that the ions pass through ΔV. All possible Larmor radii ($\rho = 0 \rightarrow \infty$), corresponding to ions of different perpendicular velocity, have to be considered. The first term on the rhs of Equ. A1.1 may be written as:

$$\left[\frac{\Delta\lambda_{jk}}{\lambda_{jk}}\right]_{mov} = -\frac{1}{c}\frac{\int_0^{\infty} v_\perp \int_0^{2\pi} n_k(v_\perp, \psi, \theta = 0)\cos\psi \, d\psi \, dv_\perp}{\int_0^{\infty}\int_0^{2\pi} n_k(v_\perp, \psi, \theta = 0)\, d\psi \, dv_\perp} \qquad (A1.3)$$

where $v_\perp$ is the speed of the excited ions perpendicular to $\vec{B}$ and the angle θ defines the angular distance of the excited ions from the volume element along the Larmor orbit, the relevant excited state ion density being at $\theta = 0$.

Whereas the density of the ground state ions n_g is a function only of the x-coordinate of the guiding centre ($n_g = n_g(\rho, \psi)$), the excited state ion density n_k is, in addition, a function of the angle θ ($n_k = n_k(\rho, \psi, \theta)$), due to the spatial dependence of the excitation probability ζ_k. Due to the finite lifetime of the excited ions their density at $\theta = 0$ is generally influenced by the excitation probability along the entire orbit.

The ionisation balance equation for the excited ions is:

$$\frac{\partial n_k(v_\perp, x)}{\partial t} = \bar{n}_g(x)\, f_g(v_\perp, x)\, \zeta_k(x) - \sum_{E_j < E_k} A_{jk}\, n_k(v_\perp, x) \qquad (A1.4)$$

where $\bar{n}_g$ is the total ground state ion density, $f_g(v_\perp, x)$ is the probability of an ion at a position x having a perpendicular speed $v_\perp$. The excitation probability ζ_k is a function of x and hence the position of the ion along the orbit defined by θ. In the case of electron impact ionisation ζ_k is given by:

$$\zeta_k(x) = n_e(x)\, \chi_{ex}(T_e(x)) \qquad (A1.5)$$

where n_e is the electron density and χ_{ex} is the rate coefficient for electron impact excitation. In the case of charge exchange with neutral atoms, ζ_k is given by:

$$\zeta_k(x) = n_o(x)\,\chi_{cx}(x) \quad \text{(A1.6)}$$

where n_o is the neutral atom density and χ_{cx} is the charge exchange rate coefficient. (Care must be taken when considering charge exchange with low energy neutrals in which case χ_{cx} may not be independent of the ion temperature, as it is to a good approximation in the case of charge exchange with high energy beam neutrals.)

Allowing for gradients in the total ground-state density $\bar{n}_g$, the ground-state ion velocity distribution f_g and the excitation probability ζ_k and expanding in a Taylor's series to first order in x gives:

$$\bar{n}_g(v_\perp, x)\, f_g(v_\perp, T_g) = \bar{n}_{go}\, f_{go}(v_\perp, T_{go}) + \left[\frac{\partial}{\partial x}\left(\bar{n}_g\, f_g(v_\perp, T_g)\right)\right]_o x_1 \quad \text{(A1.7)}$$

$$\zeta_k(x) = \zeta_{ko} + \left[\frac{\partial \zeta_k}{\partial x}\right]_o x_2 \quad \text{(A1.8)}$$

where the o-subscripts indicate that the quantities are evaluated at x = 0 and the subscripts 1 and 2 on x indicate which of the expressions given below is appropriate for x. In terms of (ρ, ψ, θ) we have:

$$x_1 = \rho \cos\psi \quad \text{(A1.9)}$$

$$x_2 = \rho\left(\cos\psi - \cos\left(\psi - \vartheta\right)\right) \quad \text{(A1.10)}$$

The differential equation (A1.4) can be written in terms θ of as:

$$\omega_g \frac{\partial n_k(\theta)}{\partial \theta} + \frac{n_k(\theta)}{\tau_k} = \bar{n}_g\, f_g\, \zeta_k(\theta) \quad \text{(A1.11)}$$

where τ_k is the mean lifetime of the excited ions and we have used the relations:

$$\theta = \omega_g\, t, \quad \frac{1}{\tau_k} = \sum_{E_j < E_k} A_{jk} \quad \text{(A1.12, 13)}$$

where the A_{jk} are the transition probabilities for level k to decay to other levels j of lower energy and ω_g is the ion gyro-frequency.

Substituting relations (A1.7), (A1.8), (A1.9) and (A1.10) into Equ. (A1.11) and retaining only terms of first order or lower in x yields the differential equation:

$$\omega_g \frac{\partial n_k}{\partial \theta} + \frac{n_k}{\tau_k} = \bar{n}_{go} f_{go} \zeta_{ko} + \left(\bar{n}'_{go} f_{go} + \bar{n}_{go} f'_{go}\right) \zeta_{ko}\, \rho \cos\psi +$$
$$\bar{n}_{go} f_{go} \zeta'_{ko} \rho \left[\cos\psi - \cos\psi\cos\theta - \sin\psi\sin\theta\right] \quad \text{(A1.14)}$$

which has a solution of the form:

$$n_k(\theta) = a\cos\theta + b\sin\theta + c \qquad \text{(A1.15)}$$

Solving for a, b and c gives:

$$a = \frac{\tau_k}{1+(\omega_g\tau_k)^2}\left(\omega_g\tau_k \sin\psi - \cos\psi\right)\bar{n}_{go}\, f_{go}\, \zeta'_k\, \rho \qquad \text{(A1.16)}$$

$$b = -\frac{\tau_k}{1+(\omega_g\tau_k)^2}\left(\omega_g\tau_k \cos\psi + \sin\psi\right)\bar{n}_{go}\, f_{go}\, \zeta'_k\, \rho \qquad \text{(A1.17)}$$

$$c = \tau\left(\bar{n}_{go}\, p_o\, f_o + \left(\bar{n}_{go}\, p_o\, f_o\right)'\rho\cos\psi\right) \qquad \text{(A1.18)}$$

To evaluate Equ. (A1.3) only $n_k(0) = a + c$ is needed. The integration over ψ can thus be performed immediately yielding:

$$\left[\frac{\Delta\lambda_{jk}}{\lambda_{jk}}\right]_{mov} = -\frac{1}{2c}\int_0^{\infty}\left[\frac{\bar{n}_{go}'}{\bar{n}_{go}} + \frac{f_o'}{f_o} + \frac{\zeta_k'}{\zeta_k} - \frac{1}{1+(\omega_g\tau_k)^2}\frac{\zeta_k'}{\zeta_k}\right] f_o\, \rho\, v_\perp\, dv_\perp \qquad \text{(A1.19)}$$

The perpendicular *speed* distribution of the ions $f_g(v_\perp)$ can be represented by a Maxwellian perpendicular *velocity* distribution given by:

$$f(v_\perp)\, dv_\perp = \left(\frac{m_g}{2\pi e T_g}\right)\exp\left\{-\left(\frac{m_g}{2eT_g}\right)v_\perp^2\right\} dv_\perp \qquad \text{(A1.20)}$$

multiplied by the appropriate 2D phase space volume, $2\pi v_\perp$. This form of $f_g(v_\perp)$ is appropriately normalised:

$$\int_0^{\infty} 2\pi v_\perp f_g(v_\perp)\, dv_\perp = 1 \qquad \text{(A1.21)}$$

Substituting the following relation for ρ:

$$\rho = \frac{v_\perp m_g}{Z_k e B} \qquad \text{(A1.22)}$$

and performing the integration of Equ. (A1.19) over $v_\perp$ yields the result:

$$\left[\frac{\Delta\lambda_{jk}}{\lambda_{jk}}\right]_{mov} = -\frac{T_g}{cZ_gB}\frac{\partial}{\partial x}\left[\ln\left(\bar{n}_g\, T_g\, \zeta_k^{\Gamma}\right)\right] \qquad \text{(A1.23)}$$

where Γ is given by:

$$\Gamma = \frac{(\omega_g \tau_k)^2}{1 + (\omega_g \tau_k)^2} \qquad \text{(A1.24)}$$

Equations (A1.2) and (A1.23) may be combined to give the velocity, $v_{i\perp}^*$, which is inferred from the Doppler shift measured in the *laboratory* frame as:

$$v_{i\perp}^* = -\frac{1}{eZ_i n_i B}\frac{\partial p_i}{\partial r} - \frac{T_i \Gamma}{eZ_i B}\left[\frac{\frac{\partial}{\partial r}(\zeta_k)}{\zeta_k}\right] + \frac{E_r}{B} = v_{diam} + v_{pseudo} + v_{rot} \qquad \text{(A1.25)}$$

where, to be consistent with Ch.2, the subscript g is replaced by i, the x-coordinate is replaced by the radial r-coordinate and the pressure of the ion species $p_i = n_i T_i$. Comparing this equation with Equ. 2.4, this analysis shows that there can be an additional Doppler shift in the presence of a gradient of the excitation rate (represented by v_{pseudo}) which is not revealed by the conventional fluid model. A Doppler shift of the line centroid results from the gradient of the excitation rate when $(\omega_i \tau_k)^2 \sim 1$ or $(\omega_i \tau_k)^2 >> 1$, even in the absence of a pressure gradient. In the limit $(\omega_i \tau_k)^2 \rightarrow 0$ this equation reduces to Equ. 2.4 which is derived from the fluid model and the gradient of the excitation rate produces no additional Doppler shift.

Appendix 2: Gradient Scale Length and Equivalent Electric Field:

In this appendix we estimate the terms arising from the pressure and excitation rate gradients which contribute to the velocity inferred from the shift of a spectral line. This is done in terms of an equivalent electric field E_Λ^* and a gradient scale length Λ.

In Appendix 1 it is shown that, in the presence of gradients of n_i, T_i and ζ_k perpendicular to $\vec{B}$ the velocity inferred from the line shift of a spectral line $v_{i\perp}^*$ is given by:

$$v_{i\perp}^* = -\frac{1}{eZ_i n_i B}\frac{\partial p_i}{\partial r} - \frac{T_i \Gamma}{eZ_i B}\left[\frac{\frac{\partial}{\partial r}(\zeta_k)}{\zeta_k}\right] + \frac{E_r}{B} = v_{diam} + v_{pseudo} + v_{rot} \qquad (A1.25)$$

where ζ_k is the excitation probability and Γ is given by:

$$\Gamma = \frac{(\omega_i \tau_k)^2}{1 + (\omega_i \tau_k)^2} \qquad (A\ 1.24)$$

Equ. (A 1.25) may be rearranged to combine the terms arising from the gradients of the pressure v_{diam} and the excitation rate, v_{pseudo}:

$$v_{i\perp}^* = -\frac{T_i}{eZ_i B}\left[\frac{\frac{\partial}{\partial r}\left(n_i T_i \zeta_k^\Gamma\right)}{\left(n_i T_i \zeta_k^\Gamma\right)}\right] + \frac{E_r}{B} = v_{diam+pseudo} + v_{rot} \qquad (A\ 2.1)$$

This combined term may be expressed in terms of an equivalent radial electric field in terms of the gradient scale length Λ:

$$E_\Lambda^* = \frac{T_i}{e Z_i}\frac{1}{\Lambda} \qquad (A\ 2.2)$$

$$\frac{1}{\Lambda} = -\frac{\frac{\partial}{\partial r}\left(n_i\, T_i\, \zeta_k^\Gamma\right)}{\left(n_i\, T_i\, \zeta_k^\Gamma\right)} = -\frac{\partial}{\partial r}\ln\left(n_i\, T_i\, \zeta_k^\Gamma\right) = -\frac{\partial}{\partial r}\left(\ln\left(n_i\, T_i\right) + \Gamma \ln \zeta_k\right) \qquad (A\ 2.3)$$

Once again separating the contributions from the pressure and excitation rate gradients we have:

$$\frac{1}{\Lambda} = -\frac{\partial}{\partial r}\left(\ln\left(n_i\, T_i\right) + \Gamma \ln \zeta_k\right) = \frac{1}{\Lambda_{diam}} + \frac{\Gamma}{\Lambda_{pseudo}} \qquad (A\ 2.4)$$

This yields the inferred velocity, $v_{i\perp}^*$, from Equ. (A 2.1) in terms of the contributions to the actual electric field, E_r, due to the equivalent electric fields from the pressure, E_{diam}^*, and excitation rate gradients, E_{pseudo}^* (the superscript * is used to distinguish the equivalent electric fields from the actual radial electric field):

$$v_{i\perp}^* = \frac{1}{B}\left(E_\Lambda^* + E_r\right) = \frac{1}{B}\left(E_{diam}^* + E_{pseudo}^* + E_r\right) \qquad (A\ 2.5)$$

In order to calculate the equivalent electric field E_Λ^* all of the contributions to the decay length Λ have to be measured or estimated. Using Van Regemorter's approximation [3.1] for the electron impact excitation:

$$\zeta_k = n_e \chi_{ex}(\Delta E_{gm}, T_e) = n_e \frac{C}{\sqrt{T_e}} \exp\left(-\frac{\Delta E_{gm}}{T_e}\right) \quad \text{(A 2.6)}$$

where C is a constant, we find for the excitation gradient term:

$$\frac{1}{\Lambda_{pseudo}} = -\frac{\partial}{\partial r}\left(\Gamma\left(\ln n_e + \ln \chi_{ex}\right)\right) = \Gamma\left(\frac{1}{\Lambda_{n_e}} + \left(\frac{\Delta E_{gm}}{T_e} - \frac{1}{2}\right)\frac{1}{\Lambda_{T_e}}\right) \quad \text{(A 2.7)}$$

Note that Λ_{pseudo} is a function of the quantity Γ and the gradient scale lengths of n_e and T_e. Furthermore, depending on the energy level under investigation, the multiplier of $1/\Lambda_{Te}$ may change sign.

The diamagnetic term of Equ. (A 2.4) may be split into the gradient scale lengths of of n_i and T_i:

$$\frac{1}{\Lambda_{diam}} = -\frac{\partial}{\partial r}(\ln n_i T_i) = \frac{1}{\Lambda_{n_i}} + \frac{1}{\Lambda_{T_i}} \quad \text{(A 2.8)}$$

With Eqs. (A 2.7) and (A 2.8) the decay length Λ of Equ. (A 2.3) can be written as:

$$\frac{1}{\Lambda} = \frac{1}{\Lambda_{diam}} + \frac{1}{\Lambda_{pseudo}} = \frac{1}{\Lambda_{n_i}} + \frac{1}{\Lambda_{T_i}} + \Gamma\left(\frac{1}{\Lambda_{n_e}} + \left(\frac{\Delta E_{gm}}{T_e} - \frac{1}{2}\right)\frac{1}{\Lambda_{T_e}}\right) \quad \text{(A 2.9)}$$

To calculate $1/\Lambda$ the density and temperature gradient scale lengths of the electrons and the ions need to be determined. However, with the possible exception of the $1/\Lambda_{Te}$ term, all the other terms are additive. Thus, despite an incomplete knowledge of all the terms, a lower limit of $1/\Lambda$ can be determined. In the following tables measured and estimated values of the gradient scale lengths appropriate to Equ. (A 2.9) together with the resulting values of $1/\Lambda$ and E_Λ^* are listed.

Table A 2.1: Summary of Relevant Atomic Data

Ion	Transition	ΔE_{gm} (eV)	Te (eV)	$\Delta E_{gm}/T_e$	$\Delta E/T_e - 1/2$	Γ
He II	$^2D - {}^2F$	2.7	80	0.033	-0.467	0.01
B IV	$^3S - {}^3P$	4.4	200	0.022	-0.478	0.58
C III	$^3S - {}^3P$	2.7	50	0.054	-0.446	0.14

where it is assumed that $T_e = T_i$ and T_i is determined from the measured Doppler broadening of the ion species considered. For the species BIV and CIII the given ΔE_{gm} (eV) is the energy difference of the excited state m from the meta-stable 'ground' state since the meta-stable triplet states are about equally populated as the singlet ground state. The appropriate evaluation of Γ is described Appendix 3.

Table A 2.2: Scale Lengths and Equivalent Electric Fields:

Ion	$1/\Lambda_{ni}$ (cm^{-1})	$1/\Lambda_{Ti}$ (cm^{-1})	$1/\Lambda_{diam}$ (cm^{-1})	$1/\Lambda_{ne}$ (cm^{-1})	F/Λ_{Te} (cm^{-1})	Γ/Λ_{pseud} (cm^{-1})	$1/\Lambda$ (cm^{-1})	E_Λ^* (kV/m)
He II	> 0.714	0.714	1.429	0.833	>-0.667	0.002	1.431	11.44
B IV					>-0.683	0.087	1.516	10.11
C III					>-0.637	0.027	1.456	3.64

Λ_{ni} is estimated from our own radial measurement, Fig. 3.5, in an Ohmic plasma; it is assumed that $\Lambda_{Ti} = \Lambda_{ni}$; Λ_{ne} is taken from a Li-beam measurement during the H-phase [A2.1]; Λ_{Te} is taken from an edge ruby laser measurement in the L-phase [A2.2]. The quantity F is defined as $F = \Delta E/T_e - 1/2$.

Taking into account that the gradient scale length Λ_x, for each quantity x, near the separatrix usually decreases from OH -> H or L -> H phase, thus increasing $1/\Lambda_x$, the estimated values of $1/\Lambda$ and E_Λ^* are likely to be lower limits of the real situation.

We conclude that $1/\Lambda_{diam}$ gives the main contribution and Γ/Λ_{pseudo} is small, particularly for He II. However, the estimated equivalent radial electric field E_Λ^* is of the order of the measured E_r. To determine E_r unambiguously it is necessary to measure at a radial position near the maximum of εT_i (for $\Gamma = 1$) where the contributions to the Doppler shift from the ion pressure and excitation rate gradients vanish as discussed in Chap. 2.

Finally, rearranging Equ. (A 2.5), we have:

$$E_r = v_{i\perp}^* B - E_\Lambda^* \quad \text{(A 2.10)}$$

with $E_\Lambda^* > 0$ and $v_{i\perp}^* < 0$ (as measured in the H-phase). Thus, taking the E_Λ^* correction into account, the magnitude of the real radial electric field, $E_r < 0$ (directed inward), as inferred from the measurement, increases.

On the other hand, considering charge exchange excitation instead of electron impact excitation, the neutral density gradient has the opposite sign of that of the electron density gradient. Therefore, the correction due to the excitation rate and life time would cause the magnitude of the inferred radial electric field to decrease. Since the gradient scale length of the neutral density due to a beam is usually small, this correction may be of importance in the case of measurements utilising line emission excited by high energy neutral beams.

Appendix 3: Estimates of Excited State Lifetimes:

In order to estimate the quantity Γ (defined by Equ. A1.24 in Appendix 1) for the particular atomic transitions investigated, the lifetimes of the excited states τ_k must be estimated from a consideration of the detailed atomic physics.

The electronic configuration and spectral term of the particular transitions used here (CIII (4648Å), BIV (2823Å) and HeII (4686Å)) and for similar studies (CV (2274Å) and CVI (5291Å)) are listed in Table A3.1.

Two cases have to be considered. For the $^3S1$ - $^3P0_{0,1,2}$ transitions of He-like BIV and CV and Be-like CIII the excited state levels of principle quantum number n' but differing orbital quantum number l' are well separated in energy by the l' dependence of the Coulomb interaction with the other electrons in the ion. In this case, at electron densities typical of ASDEX conditions, collisions by the ions of the background plasma will induce practically no transitions between states of differing l'. In this case electrons excited into a state n'l' remain in that state until they decay and the l'-states are said to be 'unmixed'. The lifetime of the excited state is then given by:

$$\frac{1}{\tau_k} = \sum_{E<E'} A_{nl}^{n'l'} \qquad (A3.1)$$

where $A_{nl}^{n'l'}$ is the transition probability for the decay of a state n'l' to a state nl and the summation is over all transitions to states of lower energy.

For the H-like ions of HeII and CVI the unmixed description is not appropriate as states of equal n' and different l' are almost degenerate. In this case the transition probabilities between states of different l', $A_l^{l'}$, due to collisions with the background plasma ions can be greater than the transition probability of the excited state; i.e.:

$$\frac{1}{\tau_k} << A_l^{l'} \qquad (A3.2)$$

In this case an electron which is excited into a level n'l' can experience several transitions into other l states before decaying. In such a situation the states of different j' will have relative populations which are proportional to their statistical weights 2j'+1. The l' levels are then said to be 'statistically mixed'. The occurrence of l-mixing can profoundly influence the lifetimes of the excited states. The nearly degenerate l'-states are populated with equal probability by electron impact excitation. In the absence of l-mixing the population of an l'-level will reach a value such that it's decay rate equals the excitation rate into that particular l'-level. The emissivity from each l'-level will then be proportional to the statistical weight of the level, 2l'+1. Transitions from some l'-levels can have much lower decay rates than others.

In the fully mixed condition, however, the l'-levels cannot be considered independently. An excited electron will have a decay probability $A_{nn'}$ from a level n' to a level n, which is given by a mean value of $A_{nl}^{n'l'}$ over all of the possible l'-states weighted by the statistical weights (2l'+1) of these l'-levels:

$$A_{nn'} = \sum_{l'} \frac{(2l'+1)\, A_{nl}^{n'l'}}{n'^2} \quad \text{(A3.3)}$$

The mean lifetime of the excited state k, of principle quantum number n', is then given by:

$$\frac{1}{\tau_k} = \sum_{n<n'} A_{nn'} \quad \text{(A3.4)}$$

It remains to decide whether the background ion density is sufficiently high for the fully mixed condition to be appropriate. Sampson [A3.1] gives a lower limit to the electron density (assuming $n_i = n_e$) for H-like ions of principle quantum number n and nuclear charge Z to be statistically l-mixed given by:

$$n_{e,\,crit} = 1.18 \times 10^{18} \frac{Z^{7.5}}{n'^{8.5}} \text{ cm}^{-3} \quad \text{(A3.5)}$$

In Table A3.1 values of $n_{e,crit}$ are evaluated for each transition together with a statement of whether the assumption of complete l-mixing is appropriate (assuming $n_e > 2 \cdot 10^{13}$ cm^{-3} for ASDEX conditions). The branching ratios of the transitions, B_{jk}, (the fraction of ions of excited state k which decay to the state j appropriate to the transition) are also listed. The decay probabilities $1/\tau_k$ are evaluated using whichever of the expressions (A3.2) or (A3.5) is appropriate to each transition. Finally, values of $\omega_i\tau_k$ and Γ are calculated assuming B=2.0T as is typically the case in ASDEX.

Table A.3.1: Summary of Relevant Spectroscopic Data.

Ion	λ [Å]	Config-uration	Spectral Term	$n_{e,crit}$ 10^{13}cm^{-3}	Mix	B_{jk}	$1/\tau_k$ 10^8s^{-1}	$\omega_i\tau_k$	Γ
CIII	4648.8	2s3s-2s3p	^{3}S1 - ^{3}P0	-	-	1	0.78	0.41	0.14
BIV	2823.4	1s2s-1s2p	^{3}S1 - ^{3}P0	-	-	1	0.46	1.17	0.58
HeII	4686	n=4-3	All pos. lj-l'j'	0.16	Yes	0.3	4.78	0.10	0.01
CV	2273.9	1s2s-1s2p	^{3}S1 - ^{3}P0	-	-	1	0.57	1.13	0.56
CVI	5291	n=8-7	All pos. lj-l'j'	1.7	Yes	<1	>1.07	<0.75	<0.48

References:

[1.1] Wagner, F., Becker, G., Behringer, K., Campbell, D., Eberhagen, A. et al., *"Regime of Improved Confinement and High Beta in Neutral Beam Heated Divertor Discharges of the ASDEX Tokamak"*, Phys. Rev. Lett., Vol 49, No 19 (1982), 1408-1412.

[1.2] Itoh, S.I., Itoh, K., *"Model of the L- to H-mode Transition in Tokamaks"*, Phys. Rev. Lett. Vol 63 (1988), 2276.

[1.3] Bigliari, H., Diamond, P.H., Terry, P.W., *" The Influence of Sheared Poloidal Rotation on Edge Turbulence"*, Phys. Fluids B, Vol 2, No 1 (1990), 1.

[1.4] Hinton, F.L.,*"Thermal Confinement Bifurcation and L- to H-mode Transition in Tokamaks"*, GA Report, GA-A20151, July 1990.

[1.5] Shaing, K.C., Crume, E.C.Jr.,*"Bifurcation Theory of Poloidal Rotation in Tokamaks: a Model for the L -> H Transition"*, Phys. Rev. Lett., Vol 63 (1989), 2369.

[1.6] Groebner, R.J., Burrell, K.H., Seraydarian, R.P., *" Role of Edge Electric Field and Poloidal Rotation in the L-H Transition"*, Phys. Rev. Lett., Vol 64, No 25 (1990), 3015-3018.

[1.7] Ida, K., Hidekuma, S.,*" Edge Electric Field Profiles of H-mode Plasmas in the JFT-2M Tokamak"*, Phys. Rev. Lett., Vol 65 (1990), 1364.

[1.8] Taylor, R.J., et. al.,*" H-mode Behaviour Induced by Biassed-Field Currents in a Tokamak"*, Phys. Rev. Lett., Vol 63 (1989) 2365.

[1.9] Weynants, R.R. et al.,*"H-mode Behaviour Induced by Radially Outwards Field Imposed in TEXTOR"*, 13th IAEA Conference on Plasma Physics and Controlled Nuclear Fusion Research, Washington (1990), IAEA-CN-53/A-6-6.

[2.1] Spitzer, L., Jr., *"Physics of Fully Ionized Gases"*, Interscience, John-Wiley & Sons, Inc. (1962) ISBN 0 470 817232.

[2.2] Lotz, W., *" Electron-Impact Ionization Cross-Sections and Ionization Rate Coefficients for Atoms and Ions"*, Ap. J. Suppl., Vol 14, (1967), 207-238.

[3.1] Van Regemorter, H., Astrophys. J., 136 (1962) 906.

[4.1] Fussmann, G., Hofmann, J.V., Janeschitz, G., Szigeti, J., *"An Optical Scanning System for Spectroscopic Impurity Flux Measurements Inside the ASDEX Tokamak."*, (1989) IPP Report, IPP III/152.

[5.1] Bevington, P.R., "Data Reduction and Error Analysis in the Physical Sciences.", Mc. Graw-Hill (1969) ISBN-69-16942.

[5.2] Wiese, W.L., Smith, M.W., Glennon, B.M., "Atomic Transition Probabilities, Hydrogen through Nickle", U.S. Department of Commerce, National Bureau of Standards, NSRDS-NBS-4 (1966).

[6.1] Wagner, F., Ryter, F., Field, A.R., Fussmann, G., Hofmann, J.V., Manso, M.E., Vollmer, O., et al., "Recent Results of H-Mode Studies on ASDEX", I.A.E.A., Washington, Oct. 1st - 6th (1990).

[6.2] Hazeltine, R.D., *"Rotation of a Toroidally Confined Collisional Plasma"*, Phys. Fluids, 17, 5 (1974) 961.

[6.3] Hinton, F.L., *"Thermal Confinement Bifurcation and the L- to H-Mode Transition in Tokamaks"*, G.A. Report, GA-A20151 (1990), Submitted to Phys. Fluids B.

[6.4] Hassam, A.B., Kulsrud, R.M.,*"Time Evolution of Mass Flows in a Collisional Tokamak"*, Phys. Fluids, 21, 12 (1978) 2271.

[6.5] Stix, T.H., *"Decay of Poloidal Rotation in a Tokamak Plasma"*, Phys. Fluids, 16, 8 (1973) 1260.

[6.6] Braginskii, S.I., *" Transport Processes in a Plasma"*, Rev. Plasma Phys., Vol 1, (1965), 205-311.

[A2.1] Mc. Cormick, K., et al., J. Nucl. Mater., Vol. 145-147 (1987) 215

[A2.2] Murman, H., Huang, M., "*Thomson Scattering Diagnostic in the Boundary Layer of ASDEX*", Plasma Phys. and Contr. Fus., Vol. 27, No. 2 (1985) 103-114

[A3.1] Sampson, D.H., J. Phys. B, 10 (1979) 749